INFLUENCE OF MORPHOLOGY AND SURFACE MODIFICATIONS ON THE PHOTOCATALYTIC ACTIVITY OF TITANIA-BASED NANO TUBE ARRAYS

Thesis submitted to
University of Calicut, Malappuram
in partial fulfillment of the requirements for
the award of the degree of

DOCTOR OF PHILOSOPHY IN CHEMISTRY
under the Faculty of Science

By

MANOJ N.

Under the supervision of

Dr. V. KUMAR,
Senior Scientist

CENTRE FOR MATERIALS FOR ELECTRONICS TECHNOLOGY [C-MET]
(Scientific Society, Ministry of Electronics and Information Technology (MeitY)
Govt. of India, M.G. Kavu, Athani P.O, Thrissur 680581, Kerala India
www.cmett.gov.in
August 2018

INFLUENCE OF MORPHOLOGY AND SURFACE MODIFICATIONS ON THE PHOTOCATALYTIC ACTIVITY OF TITANIA-BASED NANO TUBE ARRAYS

Ph.D. Thesis

Submitted by

Manoj N.
S/O N. Vishnu Unni
Nageri Illam
P.O.Pulpatta
Manjeri, Malappuram
Kerala-676123
e-mail: manonageri@gmail.com

Research Supervisor
Dr.V.Kumar
Senior Scientist
Centre for Materials for Electronics Technology
Trissur-680581
Kerala, India
e-mail: vkumar@cmet.gov.in

August 2018

UNIVERSITY OF CALICUT
CERTIFICATE ON PLAGIARISM CHECK

1.	Name of the research scholar	MANOJ. N		
2.	Title of thesis/dissertation	INFLUENCE OF MORPHOLOGY AND SURFACE MODIFICATIONS ON THE PHOTOCATALYTIC ACTIVITY OF TITANIA-BASED NANO TUBE ARRAYS		
3.	Name of the supervisor	Dr. V. KUMAR		
4.	Department/Institution	C-MET THRISSUR		
5.		Introduction/ Review of literature	Materials and Methods	Result/Discussion/ Summary/Conclusion
	Similar content (%) identified	1 %	4 %	0 %
	Acceptable maximum limit (%)	25	25	10
6.	Software used	Urkund		
7.	Date of verification	8/8/2018		

*Report on plagiarism check, specifying included/excluded items with % of similarity to be attached.

Checked by (with name, designation & Signature) _[signature]_ Dr. Vinod. V.M.
Assistant Librarian
University of Calicut

Name & Signature of the Researcher _[signature]_ Manoj. N

Name & Signature of the Supervisor _[signature]_ Dr. V. Kumar
Scientist
Centre for Materials for Electronics
Technology (C-MET), DIT, Govt. of India
Mulangunnathukavu, Athani,
Thrissur-680 581

The Doctoral Committee* has verified the report on plagiarism check with the contents of the thesis, as summarized above and appropriate measures have been taken to ensure originality of the Research accomplished herein.

[signature]

Name & Signature of the HoD/HoI (Chairperson of the Doctoral Committee)

डॉ. एन. रगु
Dr. N. RAGHU
निदेशक/**Director**
सी-मेट (एम इ आइ टी वै, भारत सरकार)
C-MET (MeitY, Govt. of India)
अत्तानि पोस्ट/Athani P.O., एम.जी. कावु /M.G. Kavu
त्रिश्शूर - ६८० ५८१ / Thrissur - 680 581
केरला/ Kerala

सेन्टर फॉर मेटिरियल्स फॉर इलेक्ट्रॉनिक्स टेक्नोलॉजी (सी-मेट)

(वैज्ञानिक संस्था, इलेक्ट्रॉनिक्स और सूचना प्रौद्योगिकी मंत्रालय, भारत सरकार)

षोरनूर रोड, मुलंगुन्नतुकावु पोस्ट, अत्तानि, त्रिशूर - 680 581, केरला, भारत

CENTRE FOR MATERIALS FOR ELECTRONICS TECHNOLOGY

(Scientific Society, Ministry of Electronics and Information Technology, Government of India)

Shoranur Road, P.O. Mulangunnathukavu, Athani, Thrissur - 680 581, Kerala, India

Tel : EPABX : 91-487-2201156-59 (4 LINES). Fax : 91-487-2201347

E-mail : cmett@cmet.gov.in   URL : www.cmet.gov.in

CERTIFICATE

This is to certify that the thesis entitled **"INFLUENCE OF MORPHOLOGY AND SURFACE MODIFICATIONS ON THE PHOTOCATALYTIC ACTIVITY OF TITANIA-BASED NANO TUBE ARRAYS"** submitted to University of Calicut in partial fulfillment of the requirements for the award of the degree of **Doctor of Philosophy in Chemistry** under the Faculty of Science, University of Calicut, is a record of the authentic work carried out by **Manoj. N.**, at Centre for Materials for Electronics Technology, Thrissur, under my guidance. The work presented in this thesis has not been submitted for any other degree or diploma of this or any other University and has been found to have no plagiarism using the software approved by the UGC/University.

Thrissur

२९ August 2018

Dr. V. Kumar

Supervising Guide

CERTIFICATE

This is to certify that the corrections/modifications are suggested by the adjudicators have been incorporated in the thesis entitled **"INFLUENCE OF MORPHOLOGY AND SURFACE MODIFICATIONS ON THE PHOTOCATALYTIC ACTIVITY OF TITANIA-BASED NANO TUBE ARRAYS"** submitted by **Manoj. N.**, to University of Calicut. The content in CD and hard copy is same.

Thrissur
16 April 2019

Dr. V. Kumar
Supervising Guide

DECLARATION

I hereby declare that the thesis entitled **"INFLUENCE OF MORPHOLOGY AND SURFACE MODIFICATIONS ON THE PHOTOCATALYTIC ACTIVITY OF TITANIA-BASED NANO TUBE ARRAYS"** submitted to University of Calicut, is based on the original research work carried out under the guidance and supervision of **Dr. V. Kumar**, Senior Scientist, Centre for Materials for Electronics Technology, Thrissur. No part of this work has been presented for any other degree from any other institution.

29-08-2018

Thrissur

Manoj. N.

ACKNOWLEDGEMENT

I, personally wish to express my hearty gratitude towards God for his blessings in my life which cannot be expressed in a single word.

I would like to thank all those people who made this thesis possible and unforgettable experience for me. At the end of my thesis, it is a pleasant task to express sincere gratitude to all those who contributed in many ways to the success of this study.

At this moment of accomplishment, First of all, I would like to extend my sincere gratitude to my research supervisor Dr. V. Kumar, Senior Scientist and former Director, C-MET, Thrissur for his dedicated help, patience, advise, inspiration, encouragement and continuous support throughout my Ph.D. He is a great scientist of material science and an eminent teacher. Under his guidance I successfully overcame my difficulties and learnt a lot. His care and advice help to face problematic situations during the entire research work.

I am grateful to the C-MET Executive Director Dr. N. R. Muniratnam, Director Dr. Raghu, former Executive Director Dr D. P. Amelnekar and former Director Dr. K. R. Dayas for permitting me to carryout research activities at this institution.

I would like to express my sincere gratitude to all scientists in C-MET, especially to Dr. S. N. Potty, Dr. N. C. Pramanik, Dr. R. Ratheesh, Dr. A. Seema, Dr. Radhika, Dr. Stanly Jacob, Dr. M. N. Muralidharan and Dr. K. P. Murali (former Scientist C-MET, Thrissur) for their constant support and encouragement. I am also thankful to all technical staffs of

Words really fail to express the love, care, support and encouragement that I enjoyed from my Mother (Ms. Varada Mani. N) and Father (Mr. N. Vishnu Unni). I am indebted to my Brother (Mr. N. Vishnu Anand) for all his support and encouragement without which I was not able to do my research work. They motivated and encouraged me with their valuable advice, care and love throughout my life. I mention my sincere gratitude to Ms. Vinitha Anand, Master Niranjan Vishnu and Navaneeth Vishnu for their deep affection and love. Their presence always makes me energetic. I express my sincere gratitude to Ms. Sathyabhama for her support during my research work

I am also grateful for the support and love received from my sisters (Ms. Seethadevi Vasudevan and Ms. Sreevidya Kesavadas) and their family. Their constant encouragement and care helped me to face difficult situations during the research work.

I am thankful to all other family members for their constant support and encouragement throughout this study. Besides this, several people have knowingly and unknowingly helped me in the successful completion of this Ph. D work.

Manoj. N.

Dedicated to

My Family Especially to
my Mother, Father and Brother for their immeasurable love and Care

PREFACE

Semiconductor photocatalysis is an interesting field of research, due to its excellent applicability in various areas such as, removing or degrading the contaminants present in the environment, self-cleaning of glass, production of hydrogen by splitting of water, conversion of carbon dioxide into gaseous hydrocarbons in presence of water etc. Photocatalysts are also used as good antibacterial agents. Advantages like environment friendly nature, sustainability, energy saving, and cheaper material cost make photocatalysis a suitable phenomenon for rectifying energy and environmental related problems like pollution. Properties of semiconductor plays vital role in deciding the photocatalytic activity of the materials. A good photocatalyst should be photostable and non-toxic nature. Chemical/biological stability are also important. The band-gap of the semiconductor decides the life-time of excited species and photocatalytic activity of the semiconductor. TiO_2 has all the above mentioned properties that a good photocatalyst should possess. Morphological features have also a key role to control the photocatalytic activity, since the morphology can affect the surface properties like porosity and surface area which in turn decides the catalytic activity of the material. Hence 1-dimensional nanomaterial like nanowires, nanorods and nanotubes were widely studied for such applications due to their morphological importance. Among them photocatalytic applications of 1-dimensional nanotube arrays has attracted much interest due to their unique morphological properties, which include high porosity and surface area. Another advantage of TiO_2-nanotube arrays is that it can be easily converted to nanotubes of

other materials like $SrTiO_3$ and $BaTiO_3$. Construction of heterogeneous nanostructure and doping are the two important strategies which are extensively employed to tune the band-gap. Redox potential of reactions involved during the fabrication of heterostructures has an important role to determine the properties of the heterostructure. Even though a lot of research were carried out about the heterogeneous structure of TiO_2 nanotube arrays, surface modified heterostructures of TiO_2-nanotube arrays and influence of redox potential during the fabrication of heterostructure was not studied and reported in detail. In this research work we have studied the photocatalytic activity of surface modified TiO_2 nanotube arrays using different characterization techniques. Our research work has also focused on the extension of the photocatalytic application of $BaTiO_3$ nanotube arrays, (ferroelectric material) synthesized by hydrothermal method using TiO_2 nanotube array as template. We fabricated heterogeneous nanostructure of $BaTiO_3$ with SnO_2 and studied photocatalytic applications by considering the redox potential of the reactions involved during the fabrication process of heterostructure. Another way to introduce defect energy levels within the valence and conduction bands of materials is doping. In this research work, we have also tuned the band-gap of $BaTiO_3$ nanotubes to visible light region through B-site doping with Mn^{3+} ions. The applicability of ferroelectric material in photocatalysis is an area which is not at all fully studied and explored.

The thesis is organized into five chapters. Chapter-1, deals with the motivation for the present research work, general introduction consisting of importance of semiconductor photocatalysis, factors effecting photocatalysis, and general methods used for modifying the

photocatalysts. Introduction section also explains the structural properties of TiO_2 and the suitability of TiO_2 for photocatalytic applications. In addition to this Chapter-1 discusses the importance of 1-dimensional TiO_2 nanotube arrays prepared by anodisation method in photocatalytic studies. Detailed discussions of anodisation process, factors affecting the nanotubular growth, important methods used for modifying the TiO_2 nanotube arrays for photocatalytic applications are provided in Chapter-1. The last sections of this chapter deals with importance of ferroelectric material like barium titanate for photocatalytic applications. This section also discusses the structural properties of $BaTiO_3$, and the advantages of $BaTiO_3$ nanotube arrays for photocatalytic applications. Besides these discussions, last section contains the reported studies which give in light to the photocatalytic applicability of $BaTiO_3$ nanotube arrays. A brief outline of the present research work is given in the last section of the chapter.

Chapter-2 is dedicated to the discussions regarding the techniques used for preparation and modification of TiO_2 nanotube arrays. The general experimental procedure adopted for anodisation process and detailed discussion of hydrothermal synthesis, which is used for modifying TiO_2 nanotube arrays are given in the first section of this chapter. Also this chapter briefly explains the principles and theory behind major characterization techniques used in the present study such as XRD, Raman spectroscopy, UV-Vis spectroscopy, Scanning Electron Microscopy (SEM), Photoluminescence spectroscopy, X-ray photoelectron spectroscopy, Electron Paramagnetic Resonance (EPR) spectroscopy, Vibrating Sample Magnetometry (VSM) etc:- This chapter also discusses the experimental set up used for the

photocatalytic studies of the modified and unmodified TiO_2 nanotube arrays.

Chapter-3 deals with the fabrication and UV photocatalytic studies of TiO_2-nanotube arrays with ZnO having different morphology. In this work, well ordered titanium dioxide nanotube arrays (TNA) of average diameter 129 *nm* and wall thickness of 25 *nm* were fabricated through potentiosatic anodisation of titanium (Ti) metal substrates. Such TNA were subsequently surface-modified with various amounts of zinc oxide (ZnO) nanopowders using hydrothermal technique to obtain heterogeneous TNA/ZnO nanostructures. The crystalline phase and surface microstructure of the heterostructures were determined by X-ray diffraction, Raman spectroscopy and scanning electron microscopy respectively. The morphology of the heterostructures strongly depended on the hydrothermal conditions employed. The photocatalytic activity of the heterostructures have also been investigated and correlated with their surface morphology and texture. It was observed that the TNA/ZnO heterogeneous nanostructure exhibited higher photocatalytic activity than unmodified TNA. The maximum photocatalytic activity was observed for the TNA/ZnO heterostructure where the surface of TNA was composed of delaminated petals from ZnO nanoflower.

Chapter-4 discusses the fabrication and visible photocatalytic application of heterogeneous nanostructure of $BaTiO_3$ nanotube arrays with SnO_2 possessing different morphological features. The photocatalytic properties of this heterogeneous nanostructure was studied by giving importance to the redox potential of the reactions

involved during the construction of heterogeneous nanostructure. Well-ordered and aligned $BaTiO_3$ nanotube arrays were prepared through hydrothermal method using TiO_2 nanotubes as precursor. SnO_2 nanoparticles were deposited on the surface of $BaTiO_3$ nanotube arrays surface to fabricate novel $SnO_2@BaTiO_3$ heterostructure for photocatalytic applications. Morphology of the SnO_2 surface layer on BTNTA was found to be dependent on the pH during hydrothermal synthesis. The $SnO_2@BaTiO_3$ heterostructures were found to exhibit enhanced photocatalytic activity under visible-light irradiation when compared to unmodified BTNTA. Results obtained from the X-ray Photoelectron Spectroscopic (XPS) and Scanning electron microscopic (SEM) studies have been combined to establish the influence of defect chemistry and surface morphology on the enhanced visible photocatalytic activity of the heterostructures.

Doping is a widely used technique to modify the band-gap of materials. Chapter-5 describes the influence of B-site Mn-doping on the visible light photocatalytic properties of $BaTiO_3$ nanotube arrays. This chapter also discusses the influence of defect-chemistry on magnetic properties of Mn-doped $BaTiO_3$ nanotubes. Well-ordered and aligned Mn-doped $BaTiO_3$ nanotube arrays (BMnxTNTA) were prepared by hydrothermal method using anodized TiO_2 nanotube arrays as template. The study reports the suitability of such band-engineered $BaTiO_3$ for visible light photocatalytic application. Photocatalytic studies demonstrated that BMnxTNTA exhibit enhanced visible light photocatalytic degradation of Methylene blue (MB) when compared to unsubstituted $BaTiO_3$ nanotube array (BTNTA). Results obtained from UV-visible spectroscopic, X-ray

photoelectron spectroscopic (XPS), photoluminescence spectroscopic (PL) and magnetic studies have been combined to establish the influence of defect chemistry on the enhanced visible light photocatalytic activity of BMnxTNTA.

The last section contains the highlights of the present work. The major findings of the present research work have led five research publications in international journal and one patent.

CONTENTS

LIST OF FIGURE

LIST OF TABLES

CHAPTER 1
INTRODUCTION

CONTENTS

1.1 Motivation of the present study

One of the major problems that we are facing today is pollution. Polluted environment can cause long term health effects on living beings on the earth. At the extreme level, the pollution can cause serious problems even on the existence of life. So we need suitable and advanced technologies to remove pollutants from the environment. Advanced oxidation technologies are widely used to degrade the organic pollutants present especially in air and water. One of the advanced and most commonly used oxidation methods to degrade the organic pollutants is photocatalysis. Photocatalysis is an interesting and highly developing area of research with a high potential of application such as in decomposition of organic pollutants, disinfection of water, air and also in the production of hydrogen. Photocatalysts also serve as good antibacterial agents. In addition to the above mentioned features, the area of research related with photocatalysis is gaining more attention from the researchers due to its several advantages such as low cost and good efficiency. Overall we can say photocatalysis is a unique and simple process for rectifying many environmental issues. Removal of pollutants from water and environment is one of the major and important applications of photocatalysis. Hence, the studies related with photocatalysis are the need of today and tomorrow. In this work we have selected for our studies the photocatalytic activity of titania based materials and also explore the possibilities of improving the photocatalytic activity and range of application of TiO_2 based materials. TiO_2 is an ideal and powerful photocatalyst due to its low cost, ease of production, high

chemical stability, high reactivity and low toxicity. Hence we have chosen titania based materials as the photocatalyst for this work. The wide band-gap of TiO_2 semiconductor restricts its application to UV region. In order to extend its application range to visible light region, its band-gap should be modified. Ferroelectrics like $BaTiO_3$ are also gaining increasing importance for photocatalytic applications Construction of heterogeneous nanostructures and suitable doping are the two important strategies that are used to modify the band-gap of a material. We adopted the above mentioned strategies (fabrication of heterogeneous nanostructures and doping method) to modify the band-gap of TiO_2 and $BaTiO_3$ materials. Redox chemistry of reactions involved during the heterogeneous nanostructure formation has a vital role in deciding their properties. The importance of redox chemistry of reactions during the construction of heterogeneous nanostructures have not been studied in detail and reported. This has motivated us to fabricate heterogeneous nanostructures by giving importance to the redox potential of reactions involved during their synthesis. Morphology of the materials also plays a crucial role in deciding their photocatalytic activity. We have chosen TiO_2 and $BaTiO_3$ having tubular morphology in this research work. The tubular parameters such as length, wall thickness, and diameter can be easily modified by changing the synthetic conditions. Hence the tubular structures are more appropriate to compare the photocatalytic activity with the surface properties like pores, surface area, and surface morphology. The importance of photocatalysis and applicability of titania based materials as a photocatalyst have prompted us to use it as the base

materials to carry out further surface and structural modifications to extend its range of application, especially to the visible light region.

1.2 Water Pollution

Water is one of the essential factors that enable life on the earth. About 3.2 million people die per year because of unsafe water, inadequate hygiene and poor sanitation [1, 2]. In the present era water pollution has turned out to be one of the important areas of discussion, since quality of water directly affects the life standard of human beings. As the population increases the availability of water becomes less, due to improper water harvesting methods. The major pollutants responsible for water pollution are the effluents from the industry. Industrial revolution intensified the amount of water pollution. The humans unintentionally contaminated the source of drinking water with raw and sewage which are directly released to the water. According to UNESCO, in the developing world 70% of industrial waste is dumped into the rivers and lakes without any treatment. The impurities released from the industries and agriculture activities are other main source of water pollution. Industrial dyes and textile dyes are the main organic compounds responsible for environmental threats especially as these types of organic wastes pollute the water sources [3, 4]. Organic dyes are the major pollutants released into water from textile and other industrial process. About 0.7 million tons of organic dyes are manufactured every year for different industrial purpose that makes serious ecological problems [5]. The main polluted wastage in textile waste are released during dying process. About 50% of the dyes used in the textile industry are of azo-type organic dye.

Fig. 1.1: Environmental scenario near by the textile industries.

Hence removal of these types of organic wastes from water is one of the major challenges that we are facing. Advanced oxidation technologies are widely using to degrade the organic pollutants present in water.

1.3 Advanced Oxidation Process (AOP)

Advanced Oxidation Processes (AOP) are effective to convert toxic organic compounds into biodegradable materials [6]. The importance of AOPs is that it will work where the conventional biological method fails. Advanced oxidation commonly uses strong oxidizing agents like H_2O_2 or ozone (O_3), catalysts (metal oxides ,iron ions, electrodes) and irradiation (solar light, UV radiations, ultrasounds) directly or in combination under mild conditions such as low temperature and pressure) [7]. Mainly there are two types of AOP

i) **AOP in presence of light -** examples are photolysis (UV irradiation in presence of chemical oxidant such as H_2O_2), photocatalyst (UV/solar light irradiation in presence of catalyst) and photo-fenton (solar light irradiation in presence of a

solution containing ferrous iron with H_2O_2 known to be Fenton's reagent)

ii) **AOP in the absence of light (dark AOP) -** examples are electrolysis, sonolysis, degradation using oxidants like fenton (solution of Fe in H_2O_2) and ozone (O_3) [8]. Sulphate-based radical systems are also reported to be used as oxidising agents in advanced oxidation process.

The mechanism of AOP involves the formation of strong oxidizing agents like hydroxyl or sulphate radicals, which reacts with organic compounds to form biodegradable intermediates. Then the biodegradable substances react with the oxidants to form water or inorganic salts known to be mineralization. AOPs, those driven by light appear to be the most general technologies for wastewater treatment [9]. Among the light driven AOPs, one of the easiest and more applicable methods for the degradation organic contaminant present in the water is photocatalysis.

1.4 Photocatalysis

The word photocatalysis is originated from the Greek language (Photo from *phos* means light and catalysis from *katalyo* means break apart, degrade). Generally the term photocatalysis explains a process in which light is used to activate a material which acts as a catalyst for a reaction. Two types of photocatalytic process are known i) Homogeneous and ii) Heterogeneous process [11]. In homogeneous photocatalysis the reactant and catalyst exists in same phase. Homogeneous photocatalyst mainly uses transition metal coordination

complex as catalyst. In presence of photon (light) the higher oxidation state metal ion complex generates hydroxyl radicals. This hydroxyl radical react with organic materials. Photo-fenton (ferrous iron in H_2O_2 solution) systems and ozone are good examples of homogeneous catalysts [1]. In heterogeneous catalysis the catalyst and the reactant are in different phases. The process of heterogeneous photocatalysis comprise of the formation of interface layer between the solid (semiconductor or metal) and reactants in the liquid phase, and consequently the light hits on the semiconductor, or metal in which active species like holes and electrons are generated leading further to formation of highly reactive radicals in the system. These reactive species react with organic matter and degrade them [12]. Even though both photocatalysis process are using for degrading the organic compounds, heterogeneous catalysis has more acceptability for these kind of application due to its enhanced rate of degradation [13]. Heterogeneous photocatalysis commonly uses reusable semiconductor catalysts and further addition of any oxidant is not required. The catalyst itself produces highly reactive species and hence heterogeneous photocatalysis have enhanced rate of degradation. Important advantages of heterogeneous photocatalysis are i) requirement of only mild temperature and pressure conditions, ii) complete mineralization, iii) low cost and iv) no waste disposal problem.

1.4.1 Heterogeneous photocatalysis

The area of heterogeneous photocatalysis has a long history of more than four decades. In 1972, Fujishima and Honda discovered the

phenomenon of photocatalytic splitting of water, using TiO_2 as an electrode under UV light heralding a new era in heterogeneous photocatalysis [14]. Since then extensive research has been carried out to produce hydrogen in oxidation reduction reactions using a number of semiconducting materials [15, 16, 17] and now the area related with photocatalysis is a rapidly developing field expanding its application to environmental protection especially for degrading the organic contaminants present in both water and air. Photocatalysis requires considerable attention of surface science, semiconductor characteristic like band-gap etc. In this research work we are giving attention to the influence of surface modified structures and morphology of the semiconducting inorganic systems on their photocatalytic activity. We have studied in detail heterogeneous photocatalysis, in this work.

1.4.2 Mechanism of heterogeneous photocatalysis.

Classical heterogeneous catalyst process can be divided into 5-steps, as follows. i) the reactants in the liquid phase transfer to the surface of the catalyst, ii) Adsorption of the reactants on the catalyst surface, iii) Reaction in the adsorbed phase, iv) Desorption of the products and v) Removal of the product from the interface region. The photocatalytic reaction occurs in the adsorbed phase. In this step, the catalyst is activated with UV/Visible light irradiation. In heterogeneous photocatalysis semiconductors are usually used as catalysts. Various Metal oxides and sulphides like TiO_2, ZnO, ZrO_2, SnO_2, CeO_2, ZnS, CdS, PbS, etc are widely used as catalyst [18]. Recent studies show that, perovskite oxides like $BaTiO_3$, $PbTiO_3$ etc. are also gaining importance as photocatalysts [19, 20]. In order to explain the suitability

7

of the semiconductors for photocatalytic process, we should discuss the structural properties of semiconductors.

1.4.3 Semiconductor photocatalysis

Photocatalysis is a process in which light is used to activate some materials which act as catalyst for many reactions. Inorganic oxide semiconductors are the most suitable for photocatalysis. In photocatalysis, creation of active species like exited electrons and holes are very important. These active species react with the surrounding medium to produce highly reactive radicals like intermediates. So the generation of active species is an important step of photocatalysis process.
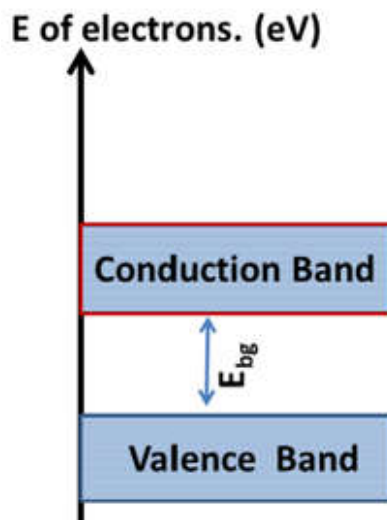
Fig. 1.2: Energy bands diagram in semiconductors.

The number of active species available for the reaction also affects the rate of photocatalysis. The material which produces active species easily, upon the irradiation of photons is said to be an appropriate catalyst for photocatalysis process. The band-gap of the semi-conductor is very suitable to the easy production of active species like exited electrons and holes (Fig. 1.2), upon the irradiation of light with suitable wavelength. The pictorial representation of the creation of active species in a semiconductor is shown below in Figure 1.3
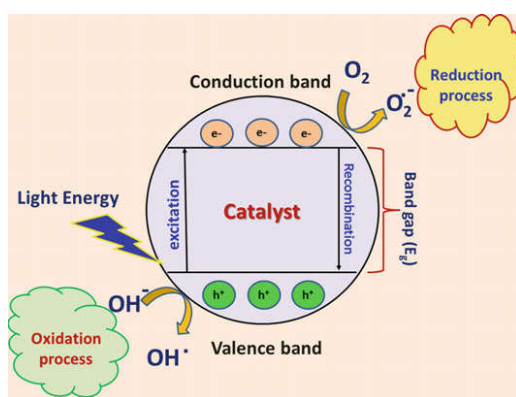
Fig. 1.3: Pictorial depiction of semiconductor photocatalysis.

[Source: R. Saravanan et al, Basic principles, Mechanism and challenges of photocatalysis , in :A. M. M. Khan, D. Pradhan, Y. Sohn (Eds.), Nanocomposites for Visible light induced Photocatalysis, (2017) Springer].

As shown in the above Figure 1.3, upon the irradiation of a suitable wavelength of energy equivalent to the band-gap, the electrons in the valence band are excited to conduction band. As a result of this excitation holes are created in the valence band. These excited electrons recombine with holes in the valence band. However for higher life times, both the electrons and holes undergo reaction with

the surrounding medium/adsorbed layers. Usually the surrounding medium contains water, hence the active species (electrons and holes) reacts with water to produce highly reactive radicals like $OH\cdot$ etc. The schematic equations are shown below [1].

$$\text{Light energy} + \text{Semiconductor} \longrightarrow \text{Semiconductor } (e_{cb}^- + h_{vb}^+) \quad (1.1)$$

$$\text{Semiconductor } (h_{vb}^+) + \text{Dye} \longrightarrow \text{Oxidation process.} \quad (1.2)$$

$$h_{vb}^+ + H_2O \longrightarrow H^+ + OH\cdot \quad (1.3)$$

$$h_{vb}^+ + OH^- \longrightarrow OH\cdot \quad (1.4)$$

$$\text{Semiconductor } (e_{cb}^-) + \text{Dye} \longrightarrow \text{Reduction process} \quad (1.5)$$

$$e_{cb}^- + O_2 \longrightarrow O_2^- \quad (1.6)$$

$$O_2^- + H^+ \longrightarrow HO_2\cdot \quad (1.7)$$

$$HO_2\cdot + HO_2\cdot \longrightarrow H_2O_2 + O_2 \quad (1.8)$$

$$H_2O_2 + O_2^- \longrightarrow OH\cdot + OH^- + O_2 \quad (1.9)$$

$$\text{Dye} + OH\cdot \longrightarrow \text{Degradation products} \quad (1.10)$$
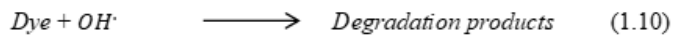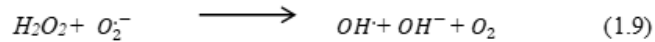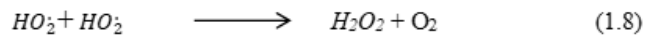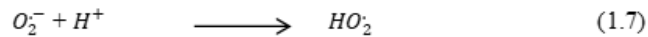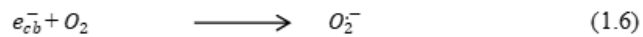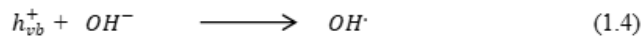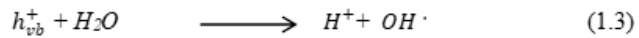
Therefore the factors which favor the generation and the life of the active species like electrons and holes should favor the photocatalytic activity of the materials.

1.5 Factors affecting photocatalytic activity of semiconducting material

The photocatalytic activity of materials mainly depends upon the properties of semiconducting materials like crystallinity, structure, size, morphology, surface area of the catalyst. In addition to these the amount of catalyst used, contaminant concentration, reaction

conditions such as light intensity, reaction temperature, pH of the medium etc. also play significant roles [1, 21].

1.5.1 Influence of crystallinity, size, and surface area

Crystalline sample has higher activity than amorphous samples. The crystalline structure of the catalyst plays an important role to decide its photocatalytic activity. TiO_2 is one of the best examples to explain the influence of crystalline structure on the photocatalytic activity of samples. TiO_2 has mainly three crystalline phases namely anatase, rutile and brookite. Anatase has highest photocatalytic activity due to its high stability, suitable position of the conduction band, adsorption capability and higher degree of hydroxylation [1].
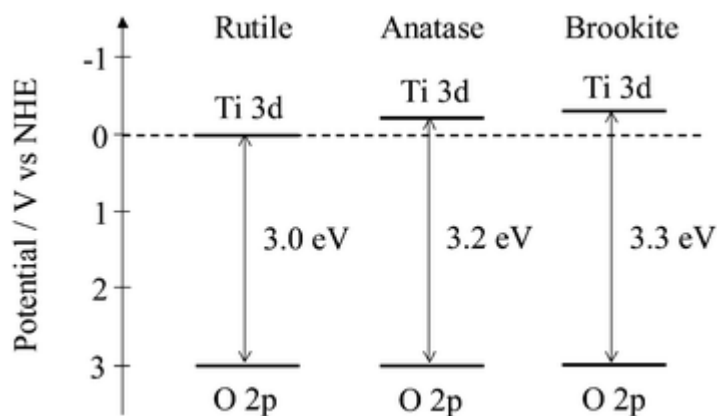
Fig. 1. 4: Band structure of TiO_2 crystalline polymorphs at pH=0.

[Source: K. Shimura et al, Heterogeneous photocatalytic hydrogen production from water and biomass derivatives, Energy Environ. Sci. 4 (2011) 2467-2481]

Crystalline size also plays a vital role in determining the photocatalytic activity of the materials. Band-gap engineering can be effectively done

by controlling the crystalline size of the sample. It is observed that in semiconducting materials with *nm* size range have large band-gap compared with that of bulk one. This is due to various quantum mechanical properties of the nanoparticles, like quantum confinement effect. A typical example is zinc oxide nanoparticles. R. Viswanatha et al prepared zinc oxide nanocrystals having size 3.0, 3.5, 4.7 and 5.4 *nm* and they calculated the band-gap of the nanocrystals as a function of the crystallite size by constructing tight binding model for ZnO valence and conduction bands. They observed a red shift in the band-gap of zinc oxide nanoparticles from 3.3 *eV* to 3. 59 *eV* as the size of the particle changes from bulk to 3.0 *nm* [22].

Photocatalytic property also depends on the number of active site present in the material. When the particle size of catalyst is small, a huge number of atoms are gathered at the surface of material, which increases surface to volume ratio, thereby increasing the active sites on the surface of material. These active sites enhances charge transfer rate and hence the rate of photocatalytic activity of the sample. As the crystalline size of the sample is less the surface area of the sample is high and therefore higher the photocatalytic activity. So normally nanomaterial has comparatively high photocatalytic activity than bulk materials, due to less size and high surface area of nanoparticles [23-25]. Photocatalysis is a surface phenomenon. Hence the surface properties like surface area, pore size, active adsorption sites can influence the photocatalytic efficiency of materials.

1.5.2 Role of Morphology (shape) of material on the photocatalytic activity

The morphology of photocatalyst is another key factor influencing the photocatalytic activity of materials. As morphology of material changes automatically the surface properties will also change which in turn influence the photocatalytic efficiency of material. The influence of morphology and photocatalytic efficiency was studied by a number of researchers, especially in semiconducting materials like ZnO, TiO_2 [26-28]. N. Khaldoon et al prepared nanosized ZnO having different morphology (nanoflowers, nanorods and nanoparticles) and studied the influence of morphology on the photocatalytic activity of the material. To obtain different morphology the authors changed the pH of the precursor solution and the hydrothermal treatment time. They observed that ZnO nanoparticles show high photocatalytic activity in comparison with that of nanoflowers and nanorods due to the increased surface area and increased defect density of nanoparticles [26]. The influence of morphology on the surface properties of TiO_2 was studied by S. Bashir Khan et al. TiO_2 nanofilms having different morphology like nanorod, nanohelics and nanozigzag were prepared by them using galancing angle deposition technique (GLAD). The photocatalytic activity of these titania nanofilms for degrading different organic dyes was evaluated. The authors observed that TiO_2 nanofilm of zigzag morphology shows enhanced photocatalytic activity. The enhanced activity is mainly due to increased surface area and porosity [27]. TiO_2 nanotube arrays are one of the important classes of TiO_2 nanostructures. In these nanostructures the tubular parameter like

length, tubular diameter and wall thickness influence the surface properties. C. A. J. Adan et al co-related the length of nanotube with the surface properties of nanotubes. The authors observed that as the length of the tube increases surface area and absorption of light increases thereby increases the photocatalytic (PC) and photoelectrocatalytic (PEC) activity. Up to an optimum nanotube length the enhancement in both PC and PEC observed after that there is reduction in the PEC enhancement is observed. This reduction is attributed to the increased transport resistance of electrons generated in the nanotubular material [28].

1.5.3 Amount of catalyst
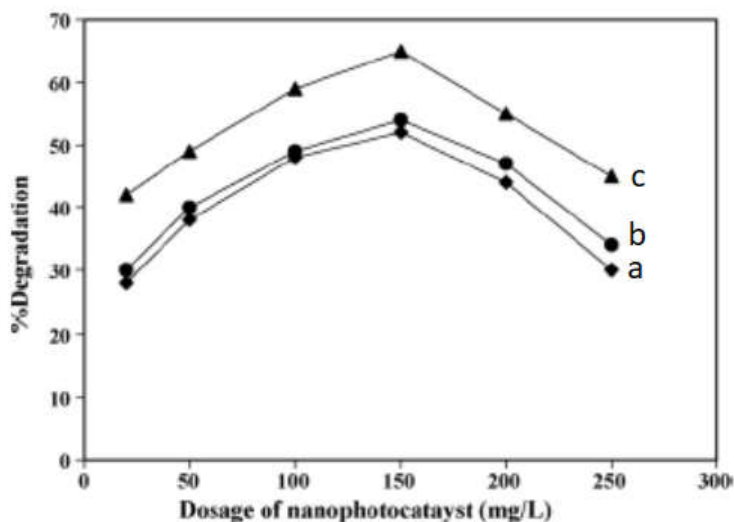
Fig. 1.5: Effect of catalyst amount on photocatalytic activity of samples for degrading methylene blue dye for: a) Mn doped ZnS b) Ni doped ZnS d) Cu doped ZnS.

[Source: H. R. Pouretedal et al, Nanoparticles of zinc sulfide doped with manganese, nickel and copper as nanophotocatalyst in the degradation of organic dyes, J. Hazard. Mater.162 (2009) 674–681]

As the amount of photocatalyst increases, the available active sites for the photocatalytic reactions increase. Hence more number of active species will be available in the medium for the degradation of organic impurities. At lower catalyst amount, degradation of organic pollutant is less since the number of available active sites is less. But in certain cases beyond the optimum amount of catalyst, the photocatalytic activity decreases, due to increase in the opacity of suspension leading to the increase in the amount of light scattered by the catalyst particles. Thus the infiltration depth of the light consequently reduces and less photocatalyst get activated. Also after the optimum concentration, the catalyst may tend to agglomerate and hence availability of active sites may decrease (Fig. 1.5). This also leads to the reduction of photocatalytic activity of the material [29].

1.5.4 Amount of organic contaminants

For a given concentration of the catalyst, it is noted that as the concentration of the organic contaminants increases the rate constant reduces. This may be explained as follows. The tendency for the formation of $OH^{\cdot}$ radicals on the catalyst surface and the reaction of the thus generated $OH^{\cdot}$ with the organic dyes (contaminants) regulates the rate of the reaction. As the initial concentration of dye increases, more and more dye molecules are adsorbed on the surface of catalyst and significant amount of light is absorbed by the dye rather than the semiconducting catalyst material. Hence the penetration of light on the surface of catalyst decreases. This decreases the number of active sites in the catalyst and hence the production of active species likes $OH^{\cdot}$ radicals also reduces. This will decrease the rate of reaction [21].

1.5.5 Reaction temperature and intensity of light source

As the reaction temperature increases up to an optimum limit the photocatalytic rate increase. The higher temperature favours the creation of number of active species, and the increased temperature may also be responsible for reduction of electron-hole recombination. But at a very high temperature like boiling point of water the photocatalytic rate get reduced. At such high temperatures exothermic adsorption of reactants is not favored leading to reduction in the reaction rate. Some studies pointed out that the optimum temperature varies within the range of 293 to 353 K [21]. Intensity of light source is also an important parameter to decide the photocatalytic activity of materials. It is also observed that as the intensity of light source increases the reduction rate of the contaminant (dye) increases. As the intensity of light source increases more number of electron-hole pairs are generated which is responsible for the creation of more number of active species [29, 21].

1.5.6 pH of the medium

pH of the contaminant (organic dye) solution is a potential factor that influences the photocatalytic rate. pH affects the adsorption and dissociation of organic molecules and surface charge of the catalyst. When the pH of photocatalyst increases above its isoelectric point, the surface of the photocatalyst becomes negatively charged. If the pH is reduced the functional group becomes protonated, this protonation leads to increase in the positive charge on the surface of photocatalyst. The negative charge on the surface of catalyst at basic pH value

adsorbs more amount of cationic molecule to the surface while at lower pH it will adsorb anionic molecules. The increased value also favours the production of hydroxyl radical ions. These above factors lead to increased photocatalytic rate at higher pH value as reported in some literatures [30, 31]. But at very high (above 12) pH the hydroxyl ions compete with organic molecules to adsorb on the catalytic surface. This leads to reduction in the photocatalytic rate [21]. Thus depending on the type of organic dyes, whether it is cationic or anionic; there will be an optimum pH value for high photocatalysis rate [32]. So we can conclude for every photocatalytic reaction there is an optimum pH value for the effective photocatalytic reactions.

1.5.7 Preparation methods

Most of the above said parameters may vary according to the preparation methods that may be adopted for the catalyst preparation. The particle size, morphology, crystallinity all may change according to the method of preparation and conditions employed. Important methods that are used for the photocatalyst synthesis are

i) Sol-gel method - Sol-gel method is a chemical solution or wet solution method. The process involves the dissolution of starting material is in a suitable solvent then the precipitating agent is added drop wise to the solution of starting material with vigorous stirring. Then the obtained sol (colloidal suspension) dried at desired temperature in order to remove the solvent from the system, which leads to the formation of gel. Then the obtained gel is calcined at suitable temperature to obtain the photocatalyst material [33, 34].

ii) Hydrothermal method - It is a heterogeneous process in the presence of aqueous solvents or mineralizers under high pressure and temperature. Hydrothermal synthesis are usually carried out in autoclaves or in teflon lined hydrothermal vessels [35, 36]. This is one of the most common methods used for the preparation of nanoparticles of photocatalyst which will be explained more in detail later

iii) Co-precipitation method - This method involves the synthesis of the products that are generally insoluble formed under conditions of high super saturations. Nucleation is a main step in co-precipitation method. Aggregation and Ostwald ripening are responsible for the morphology and size of the products formed [37].

iv) Anodisation method - Recently anodisation methods are widely used to prepare titania nanotube arrays which act as good photocatalyst. This method will be discussed detail in later.

1.6 Band-gap structure of semiconductor photocatalysts and general methods used for tuning of the band-gap of photocatalyst materials

Photocatalyst absorb UV radiations or visible radiations according to their band-gap energy. If the band-gap energy of the photocatalyst is large enough or equivalent to UV radiations, then the material is active in UV light and if it is equivalent to visible light it absorbs visible light and create active species. By using different methods we can tune the band-gap of the material. Tuning of the band-gap of the material will extend its applications from one region to other. Some

methods used for band-gap tuning also increase the life time of active species and promote the photocatalytic activity of the samples.

1.6.1 Band-gap structure of semiconductor materials

The band-gap energy of a material is the energy difference between the lowest point of the conduction band (also known as conduction band minimum) and the highest point of the valence band (known as valence band maximum). Direct band semiconductors, indirect band semiconductors and Fermi energy levels are some of the important terms used during the discussion of band-gap structure of semiconductors. A photon of energy E_g corresponding to band-gap energy can create an electron-hole pair in direct band-gap semiconductor, where as in an indirect band-gap semiconductor the electron also undergoes noticeable change in its momentum for a photon of energy to produce electron-hole pair. Fermi level is the term used to explain the top of the group of electronic energy levels at absolute zero temperature. Normally in the case of semiconductors the Fermi energy levels have energy at the center of the band-gap. Doping with suitable elements will change the position of the Fermi energy levels in the semiconductors. The addition of donor impurities which are responsible for n-type conductivity will create additional electron energy level near the bottom of the conduction band from where they are easily excited to the conduction band. Thus the effective Fermi level in n-type semiconductor shifts to a point about mid- way between the donor levels and the conduction band (Fig. 1.6b). The addition of acceptor impurities introduces energy levels in the band-gap near the valence band maximum of the semi-conductor. The electrons in the

valence band can easily be excited to these acceptor energy levels. This shifts the effective Fermi energy level to about mid-way between acceptor level and valence band (Fig. 1.6c). So it is possible to tune the band-gap of semiconductor materials by different doping mechanisms.
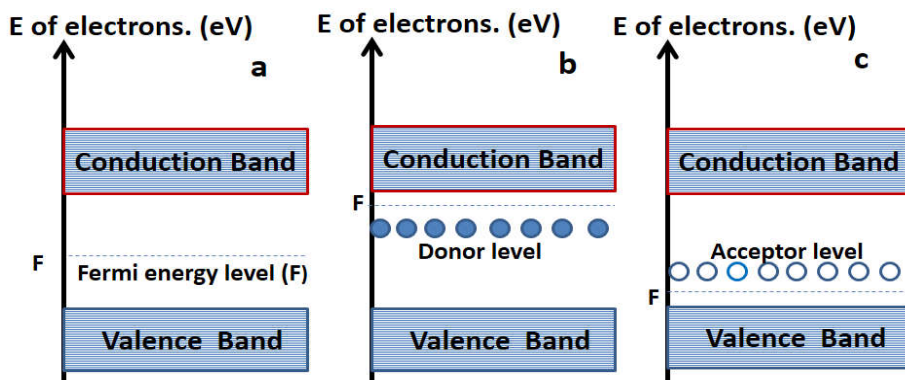
Fig. 1.6: Position of Fermi energy levels in a) undoped (intrinsic) semiconductor b) n-type semiconductor, c) p-type semiconductor.

The important methods used for tuning the band-gap energy of materials are i) construction of heterogeneous nanostructures of the photocatalyst with suitable materials and ii) modification of band-gap of the photocatalyst with suitable dopants.

1.6. 2 Heterogeneous nanostructures

The main challenge of semiconductor photocatalysis is the short life time of electron-hole pair generated during the photocatalysis and the incomplete visible light absorption of some semiconducting materials due to their large band-gap. Recently considerable works have been carried out on the design and fabrication of heterogeneous nanostructures for enhancing the photocatalytic activity [38]. Mainly four types of heterojunctions have been reported. They are i) semiconductor-semiconductor heterojunctions; ii) semiconductor-

metal heterojunctions; iii) semiconductor-carbon group heterojunctions (carbon group: activated carbon, carbon nanotubes etc), and iv) multi component heterojunctions [39]. As discussed the life time of active species generated in photocatalysis decides the photocatalytic activity of the material. Heterogeneous nanostructures increases the life time of active species and in some case shift the band gap of the material which will be discussed in detail in the following sections.

1.6.2.1 The semiconductor-semiconductor (S-S) heterostructures.
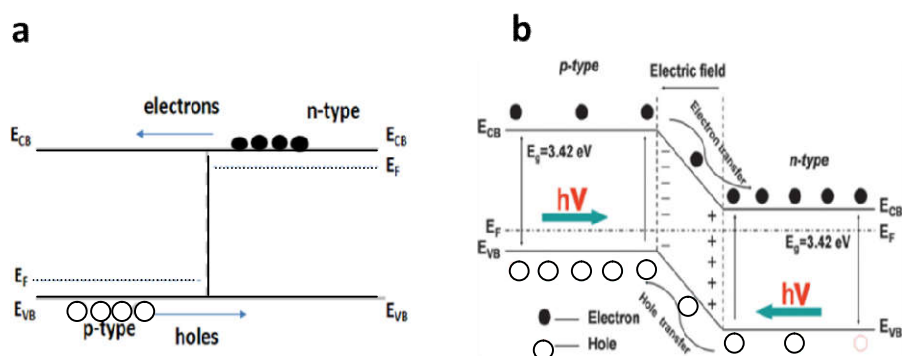
Fig. 1.7: Schematic diagram representing the band-gap and electron-hole transport of p-n hetero junction formed in between *p* and *n* type semiconductors, a) before the formation of built-in electric field b) after the formation of built-in electric field.

[Source: H. Wang et al, Semiconductor heterojunction photocatalysts: design, construction, and photocatalytic performances, Chem. Soc. Rev. 43 (2014) 5234-5244.]

Semiconductor-semiconductor heterostructures can be divided into *p-n* type heterostructures and non *p-n* type heterostructures. When *p* and *n* type semiconductors are in contact (Figs. 1. 7a and 1. 7b) as in the case of NiO@SnO$_2$ heterostructure [40], they form a *p-n* junction at the interface with the movement of electron-hole pairs. This movement of electrons and holes continue until the positions of Fermi energy levels

of both the semiconductors attaining equilibrium which responsible for creation of space charge region with a built-in electrical potential as shown in figure 1. 7b. This brings down the energy of valence band and conduction band of *n*-type semiconductor to lower level than *p*-type semiconductor. The built in electrical potential can direct the movement of electrons and holes in opposite direction. When this *p-n* heterojunction is irradiated by photons, having energy greater or equal to the band-gap of the photocatalyst material the photo generated electron-hole pair rapidly separate due to the electric field within the space-charge region. Electrons are transferred to conduction band of the *n*-type semiconductor, whereas the holes are transferred from *n*-type to *p*-type semiconductor [39, 41]. The advantages of *p-n* type heterojunctions are i) effective charge separation; ii) quick charge transference to the catalyst; and iii) longer life time of active species (charge carriers).
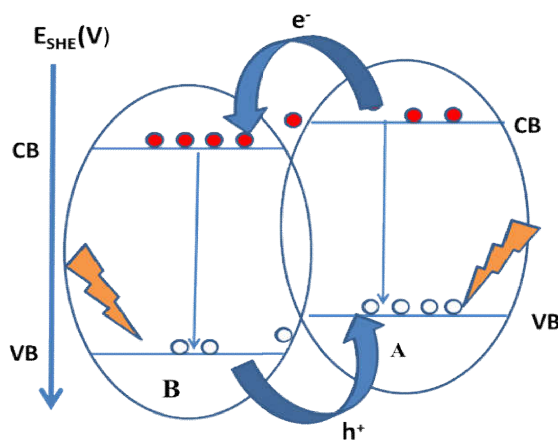
Fig. 1.8: Schematic representation and electron-hole transport in a non *p-n* heterojunction.

Non *p-n* type heterostructures as in the cases of Bi_2WO_6@TiO_2, TiO_2 (anatase)@TiO_2 (rutile) etc [42, 43] are also important. The schematic representation of a typical non *p-n* type heterojunction is shown in Figure 1.8. In this type the semiconductors *A* and *B*, which are building the heterostructure, have comparable band potentials. When the conduction band of the semiconductor *B* is lower than that of semiconductor *A*, the electrons in the conduction band of the semiconductor *A* will move to the conduction band of the semiconductor *B*. If the valence band of the semiconductor *B* is lower than that of semiconductor *A*, then the holes in the semiconductor *B* will move to the valence band of the semiconductor *A*, under photon radiation. This creates an internal field that promotes the separation and movement of photogenerated carriers. So chance of electron-hole recombination can be minimized. Hence in this type of heterostructures, the available number of electrons and holes participating directly or indirectly in redox reaction may increase and thus the photocatalytic activity is greatly enhanced. Band-gap potentials of common semiconductors are provided in Figures 1.9 and 1.10. The band position and the standard electrode potential value of the valence and conduction band of semiconductors can be obtained from Figures 1.9 and 1.10, which helps to construct heterostructres of semiconductors with suitable combination. For example, from Figure 1.9, a heterojunction as shown Figure 1.8 can be formed between ZnO (A) and TiO_2 (B).

In some cases,   the ions in the semiconductor, constituting the heterostructure may undergo oxidation or reduction according to the

standard electrode potential of the reactions involved during the synthesis of the heterostructure. This reduced or oxidized state may form intermediate energy levels within the valence and conduction bands. The position of these energy levels within the band-gap of the semiconductor depends upon the standard electrode potentials of that particular oxidation state of the ion. Thus redox chemistry has an important role in fabricating a new heterogeneous material. In addition to this there may be a chance for formation of oxygen vacancies, during the fabrication of heterostructure. This oxygen vacancy related defects also form an intermediate energy level within the band-gap. Construction of heterogeneous nanostructure giving importance to the redox chemistry of the reactions has not yet been studied in detail and is reported here for some heterostructures.
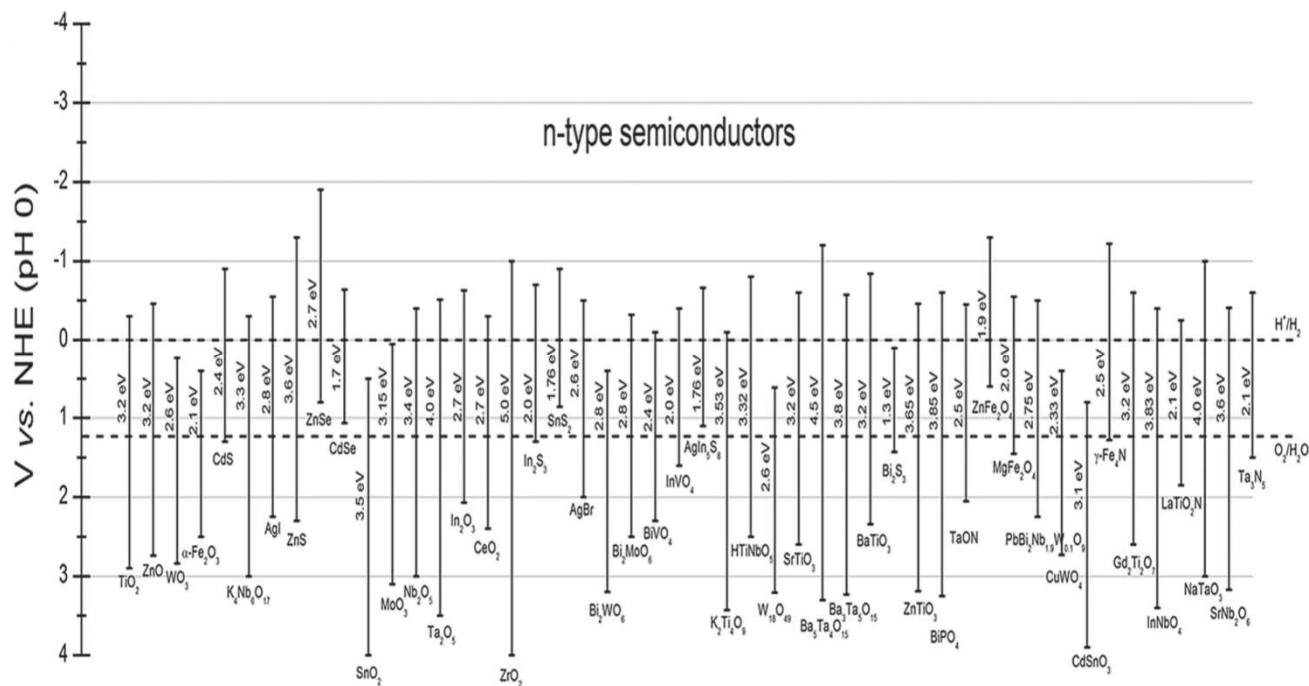
Fig. 1.9: Band-gap position of n-type semiconductors in standard electrode potential scale.

[Source: R. Marschall et al, Semiconductor Composites: Strategies for Enhancing Charge Carrier Separation to Improve Photocatalytic Activity, Adv. Funct. Mater, 24 (2014) 2421-2440]
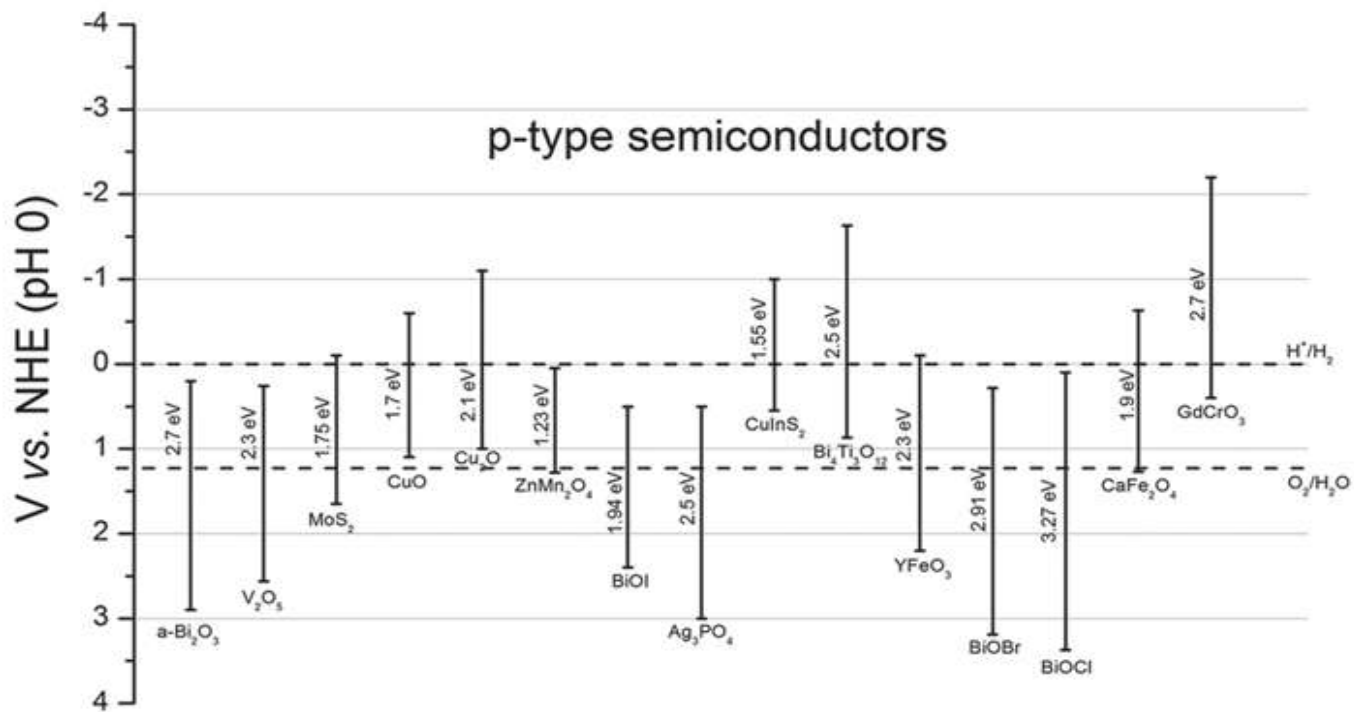
Fig. 1.10: Band-gap position of p-type semiconductors in standard electrode potential scale.

[Source: R. Marschall et al, Semiconductor Composites: Strategies for Enhancing Charge Carrier Separation to Improve Photocatalytic Activity, Adv. Funct. Mater, 24 (2014) 2421-244]

1.6.2.2 Semiconductor-metal (S-M) heterostructures

Another important method to generate space-charge separation region (known as Schottky barrier) is to construct semiconductor-metal (S-M) heterojunctions. For example Au@TiO$_2$, Ag@AgCl etc heterostructures [44, 45] have been reported. A Schottky barrier is formed between a semiconductor and a metal when it comes in contact provided that the work function (ϕ_m) of that metal is higher than that of the semiconductor (ϕ_s) (Fig. 1.11a). In such a case the electrons flows from higher Fermi levels of the semiconductor to the empty levels above the Fermi level of the metal. The Fermi levels of semiconductor and the metal line-up at equilibrium (Fig. 1.11c). Semiconductors have low charge density in comparison with that of metals. Therefore electrons are moved not only from the surface but also from certain depth region of the semiconductor.
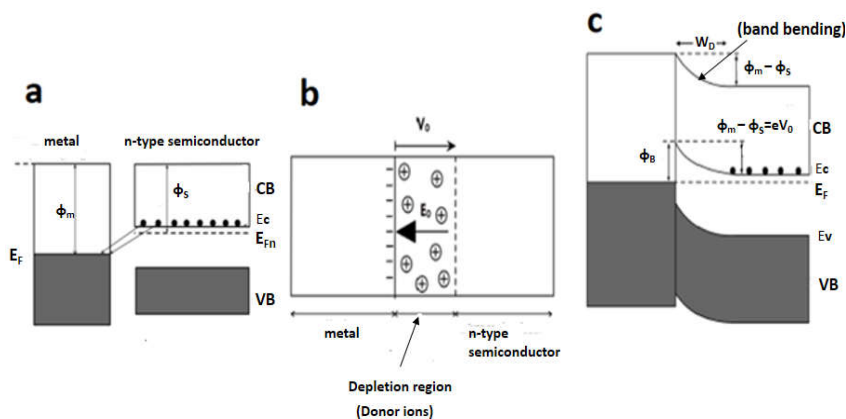
Fig.1.11: Representation of a typical metal-semiconductor heterojunction a) before contact b) after contact (formation of Schottky junction) c) shows band bending and Schottky barrier.

This kind of electron movement from the semiconductor to metal induces the formation of a depletion region within the semiconductor. The energy bands on the semiconductor side bends due to the

extension of depletion region within a certain depth in the semiconductor. Figure 1.11c shows the representation of Schottky barrier of a typical semiconductor-metal heterojunction. Generally n-type semiconductors are used to construct semiconductor-metal heterojunctions. In addition the Schottky region can function as an efficient electron trap, preventing the electron-hole recombination. Hence semiconductor-metal heterojunctions can also be used for increasing the photocatalytic activity of the materials.

1.6.2.3 Semiconductor-carbon (S-C) heterostructures

Heterostructures from Semiconductors like TiO_2, CdS, Bi_2WO_6 etc. and carbon containing material like carbon nanotubes (CNT), activated carbon, graphene etc. have been reported [46-48]. The schematic representation of semiconductor- graphene heterostructure is provided in Figure 1.12 which also explains the working mechanism of semiconductor- graphene heterostructures.
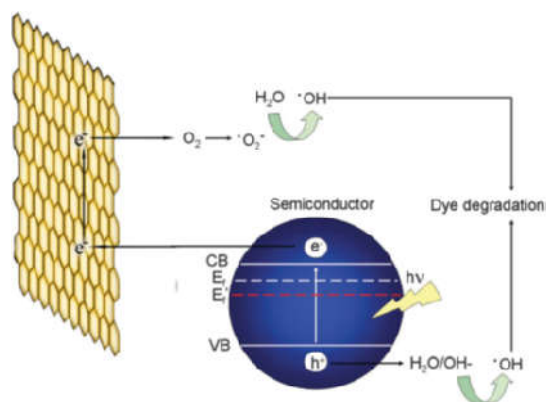
Fig.1.12: Schematic picture of semiconductor-graphene heterostructure.

[Source: H.Wang et al, Semiconductor heterojunction photocatalysts: design, construction, and photocatalytic performances, Chem. Soc. Rev. 43 (2014) 5234-5244.]

Semiconductor-Carbon type heterostructures have slightly different working principle from the other type of heterostructures. Semiconductor-carbon nanotube can form a Schottky barrier as in semiconductor-metal heterostructure and this will increase the recombination time. One of the other reasons of the increased photocatalytic activity of semiconductor-carbon nanotube heterostructure is the higher electron storage capacity of carbon nanotubes. These carbon nanotubes can receive photon-excited electrons in a mixture or their nanocomposites with semiconductors thus minimizing the recombination process [49]. In addition to this, in case of heterostructures with activated carbon, the increased photocatalytic activity is due to the large surface area of activated carbon [50]. Carbon nanotube also has large surface area. This large surface area is one of the reasons for the improved photocatalytic activity of semiconductor-carbon nanotube heterostructures. Semiconductor-graphene is another type of semiconductor-carbon heterostructure which has wide applications in photocatalysis. Graphene is a single layer of graphite and has two dimensional structure. High conductivity, high surface area, high electron mobility are other important properties of graphene. The production cost of graphene is less now days. These factors make semiconductor-graphene heterostructures suitable for wide applications [38, 51]. The graphene in the heterostructure can support charge separation, restrain the hole-electron recombination, and can provide large surface area for the reactions. The photogenerated electron produced during photon irradiation of the semiconductor, will transfer to graphene, this electron is scavenged by dissolved oxygen present in the medium and prevent

electron-hole pair recombination. In some cases the electronic interaction and charge equilibrium between graphene and semiconductor can lead to a shift in the Fermi level of the conduction band of the semiconductor. The negative shift of the Fermi energy level (Ef_i in Fig.1.12) and high migration efficiency of photo induced electrons can minimize the charge combination effectively. Thus the semiconductor-graphene heterostructure increases the photocatalytic activity.

1.6.2.4 Multicomponent heterostructure

Multicomponent heterostructures are recently developed systems to achieve more efficient photocatalysis. The pictorial representation of this type of heterostructure is provided in Figure 1.13. Typically it consists of two or more visible-light active material and an electron transfer component. An example is the AgBr-Ag-BiWO$_6$ multicomponent heterostructure system [52].
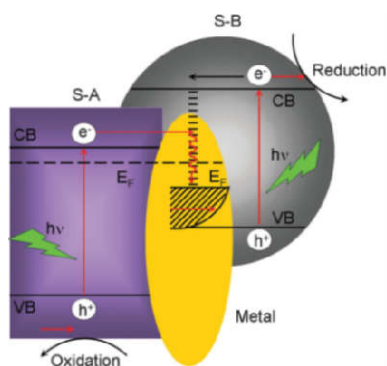
Fig. 1.13: Pictorial representation of multi component heterostructure.

[Source: H.Wang et al, Semiconductor heterojunction photocatalysts: design, construction, and photocatalytic performances, Chem. Soc. Rev. 43 (2014) 5234-5244.]

Suppose *A* and *B* are the two semiconductors in the multicomponent heterogeneous structure. *A* and *B* have different band-gap energy and therefore differ in their excitation wavelength. Thus it can extend the range of light absorption from UV to visible light and near IR. When light is irradiated, in this multicomponent system, electrons and holes are generated at conduction band and valence band respectively. The excited electron produced in the semiconductor *A* is transferred to the metal through the Schottky barrier since the conduction band potential of semiconductor *A* is higher than that of the metal. This electron transfer process is faster than the electron-hole recombination time between the valence band and conduction band of the semiconductor *A*. Because of this large concentration of holes are available in the valence band of the semiconductor *A*. This is responsible for generating more reactive species in the medium. Also the Fermi energy level of the metal is just above the valence band of semiconductor-*B*. Therefore the holes in the valence band of semiconductor *B* is easily transferred to the metal. Hence simultaneous electron-hole transfer to the metal occurs in the heterostructure as a result of photon excitation of electrons in the semiconductors *A* and *B*. In this heterostructure metal act as center for storage of electrons from the conduction band of semiconductor *A* and holes from the valence band of semiconductor *B*.

1.6.3 Modification of band gap of the photocatalyst material with suitable dopants

Chemical doping will shift the position of Fermi level of a semiconductor. It also introduces acceptor or donor energy levels within the band gap. Most of the dopants or impurities behave either as

donor or acceptor in a semiconductor; hence the incorporation of foreign elements in semiconductor metal oxides leads to the formation of intermediate energy levels within the band-gap. Paramasivam et al [53] theoretically studied the band-edge shift in TiO_2, doped with different elements and he observed that the location of these intermediate energy level within the band-gap is dependent on the type of dopant and the substitutional position in the crystal lattice (Fig. 1.14).
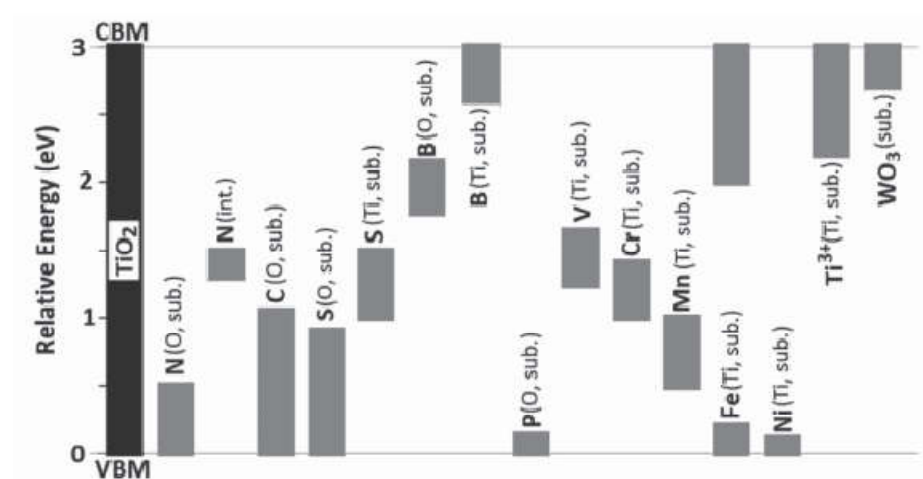
Fig. 1.14: Schematic representation of energy level position for different dopant in TiO_2 relative to band-edges.

[Source: I. Paramasivam et al, A review of photocatalysis using self-organized TiO_2 nanotubes and other ordered oxide nanostructures, Small, 8 (2012)3073-3103]

J. Wang et al studied the band structure of N-doped TiO_2 nanobelts. They observed a reduction in the band-gap value of nitrogen doped TiO_2 in comparison with that of pure TiO_2. This is due to the addition of N2p energy level near the valence band of the TiO_2 and 3d states of Ti^{3+} below the conduction band. This band-gap narrowing will help to

extend the photocatalytic application of material from UV to visible light [54]. Similarly Cobalt doped ZnO shows an additional energy band within the band-gap which leads to narrowing the band-gap of ZnO and therefore strong adsorption response in visible light region [55]. Al, Mg, Fe, Cu, Ni are other important dopants used to alter the band-gap of ZnO [56-58]. Dopants having less valence electrons than the metal ions in the semiconductor oxides may also create or enhance the native oxygen vacancy defects to compensate the charge imbalance produced as a result of doping. In this doped systems oxygen vacancy form donor levels below the conduction band minimum (CBM) [59]. For example Mg^{2+} doped TiO_2, has high concentration of oxygen vacancy defects [60]. It is also possible to create defective bands within the band-gap, by changing the preparation conditions and methods. A good example is black TiO_2, which has reduced band-gap when compared with that of commercially available TiO_2 (p-25) due to the presence of oxygen vacancy [61]. If we substitute the metal ion with dopants having higher valency extra electrons are released in the crystal. These electrons may interact with metal ions in the semiconductor and reduce them. The reduced metal state may form an extra energy level within the band-gap of semiconductor. From the above discussion it is clear that dopants or impurities may introduce defective energy levels in between the valence and conduction band of the semiconductor.

In certain semiconductors without any dopants, the inherent native defects itself may be responsible for the alteration of the band-gap. ZnO is one of the semiconductors having native defects like oxygen

vacancy $(V_{\dot{O}}, V_{\ddot{O}})$ [forming donor levels within the band gap], Zn-vacancy $(V_{Zn}^{1}, V_{Zn}^{11})$ [forms acceptor type defects], Zn-interstitial $(Zn_i,$ $Zn_i^{.})$ [acting as a shallow donor]. Defects such as Zn-antisite, oxygen interstial, oxygen antisite are also found in ZnO which form defective energy levels within the band-gap [62].

1.7 Magnetic interactions in Dilute Magnetic Semiconductors (DMS)-Tool for identifying defects.

An electron in a defect center such as V_{Zn}', $V_{O}^{.}$ etc. can induce exchange interactions between magnetic ions leading to ferromagnetism in materials. Thus the presence and type of defects can be identified from its magnetization study. Hence it is good to discuss the defect induced magnetic interactions, for a better understanding of the defects present in the material. The ferromagnetic ordering in DMS materials can be explained based on various exchange interactions like RKKY interaction (exchange interaction between magnetic ions with electrons in the conduction band), direct exchange interaction (direct interaction between d electrons of adjacent transition metal atoms), super exchange interaction (p-orbitals of oxygen mediates the exchange interaction between d electrons of transition metal), double exchange interaction (magnetic exchange interaction between ions in different oxidation states) and bound magnetic polarons (defect mediated magnetic exchange interaction). The mechanism of bound magnetic polarons interaction is based on the type of donor defects present in the material [63-66].

1.7. 1 Bound Magnetic Polarons (BMP)

An electron trapped in a donor defect such as singly ionised oxygen vacancy ($V_O^{\cdot}$), can be modeled as an electron in a hydrogenic orbital and form bound magnetic polarons (BMP) facilitating exchange interactions between magnetic cations in its influence [67]. The schematic representation of bound magnetic polaron is shown in Figure 1.15
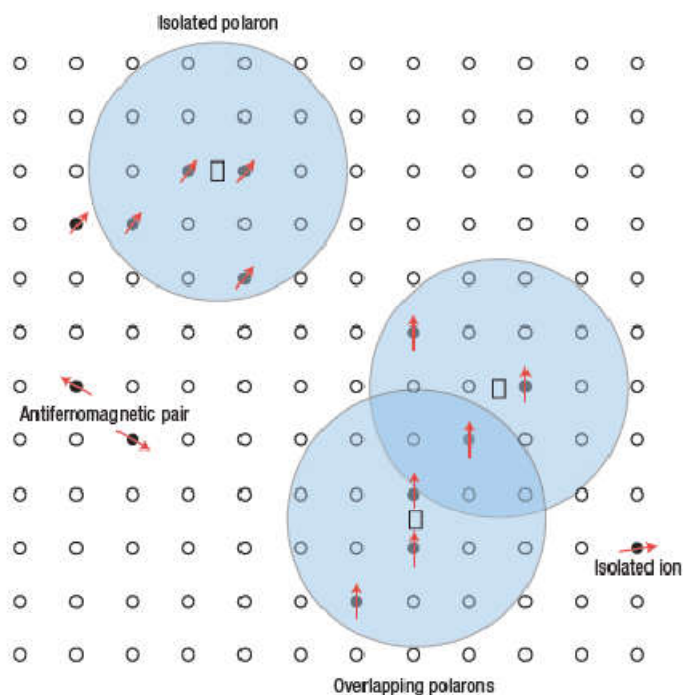
Fig. 1.15: Schematic representation of bound magnetic polaron model. Small circles represent cation sites, squares represents unoccupied oxygen sites. Oxygen is not shown.

[Source: J. M. D. Coey et al, Donor impurity band exchange in dilute ferromagnetic oxides, Nat. Mater. 4 (2005) 173-179]

Thus magnetic data may also help in understanding the nature of defects present in a material.

1. 8 Importance of TiO$_2$

For a semiconductor to have application as photocatalyst its morphology, structure, surface characters and electrical properties are important. In addition to these, a good photocatalyst should be i) able to absorb UV/Visible light (according to the band-gap in order to extend the photocatalytic applications); ii) chemically inert and photo stable; iii) inexpensive for production and iv) nontoxic in nature [68]. Among the various semiconductor oxides TiO$_2$ is one of the most suitable candidates for photocatalytic application which have all the characters (mentioned above) that a good photocatalyst should have. Hence in this work we have selected TiO$_2$- based materials for photocatalytic studies. Hence in the following discussions, focus is on the structural, morphological and electronic properties of TiO$_2$.

1.9 TiO$_2$-photocatalyst.

TiO$_2$ in its different crystalline modifications has shown good photocatalytic applications due to their favourable properties like nontoxicity, chemical stability, and suitable band-gap energy. Research of well-defined photocatalytic reaction systems and of their thorough reaction mechanisms and kinetics using different molecular spectroscopy have led to the growth of various Ti−oxide-based photocatalytic materials. TiO$_2$ based photocatalyst finds different important applications such as purification of water, air, self-cleaning glasses, tiles and hydrophobic coatings. Studies have also been

reported on the use of visible light active TiO_2 photocatalysts through the following strategies, i) altering the band-gap with suitable dopants; and ii) tailoring their defect chemistry. It is also possible to tune the band-gap of TiO_2 based materials, through the design of appropriate heterostructures to extend the window of application from UV to near IR [69].

1.9.1 Structure of TiO_2

TiO_2 occurs in nature mainly in three polymorphic crystal forms namely 1) rutile 2) anatase and 3) brookite in which rutile is the stable form, while the brookite and anatase polymorphs are metastable states [70-72]. Both rutile and anatase have tetragonal crystal structure. In rutile and anatase structures, each Ti-is coordinated to 6 oxygen atoms. TiO_6 octahedra is slightly distorted in both rutile and anatase forms and it is more in anatase. The structure of anatase and rutile consists of chains of TiO_6 octahedra having common edges. Two edges of octahedra are shared in rutile whereas four edges are shared in anatase [73, 74]. The third form, brookite has orthorhombic crystal structure, and has eight formula unit per cell. The structure of brookite is more complicated than rutile and anatase. The important difference between the brookite structure with other polymorphs is that there are six different type of Ti-O bond lengths and 12 types of O-Ti-O bond angles in brookite whereas in case anatase and rutile only two types of Ti-O bond length and O-Ti-O bond angles have been found. Brookite structure is formed by linking together the distorted TiO_6 octahedra by sharing three edges [74]. Figure 1.16 presents schematic crystal structures of rutile, anatase and brookite.
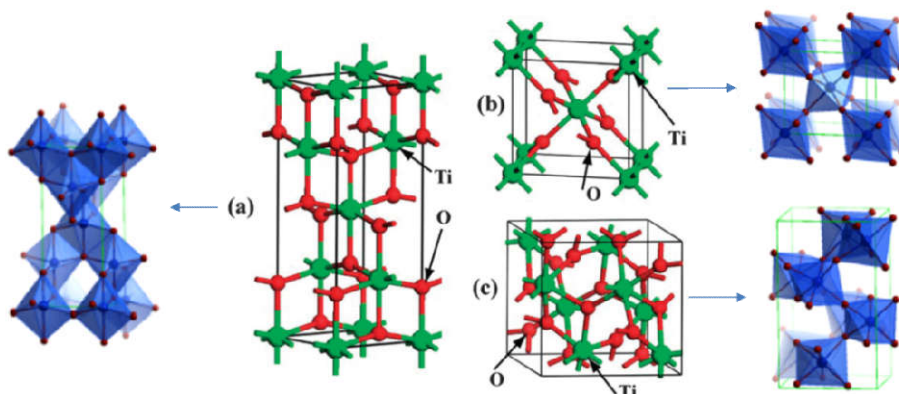
Fig. 1.16: The Schematic representation of unit cells of a) anatase b) rutile c) brookite.

[Source: J. Zhang et al, New understanding of the difference of photocatalytic activity among anatase, rutile and brookite TiO_2, Phys. Chem. Chem. Phys. 14 (2014) 20382-20386.]

Major characteristics of anatase, rutile and brookite are provided in Table 1.1

Table 1.1

Properties	Anatase	Rutile	Brookite
Crystal structure	Tetragonal	Tetragonal	Orthorhombic
Lattice constant (A^0)	a=3.784 c=9.515	a=4.5936 c=2.9587	a=9.184 b=5.447 c=5.154
Space group	$I4_1$/amd	$P4_2$/mnm	Pbca
Molecule(cell)	2	2	4
Volume $(A^0)^3$	34.061	31.2160	32.172
Density	3.79	4.13	3.99
O-Ti-O bond angle	77.7^0, 92.6^0	81.2^0, 90^0	77.0^0-105^0

38

1.9. 2 Electronic band structure of TiO$_2$

The main focus of this work is to modify the band-gap of TiO$_2$ to extend its application to visible light as a photocatalyst. In this context, it is necessary to discuss about the electronic band structure of TiO$_2$. Molecular orbital diagram help to understand the nature of molecular orbitals contributing to the valence band and conduction band (Fig. 1.17). Anatase TiO$_2$ consists of chains of TiO$_6$ octahedra. The formation of molecular orbitals by mixing of atomic orbitals of Ti and six O atoms can be explained by molecular orbital diagram as shown in Figure 1.17 where both σ and π- bonding are considered. From the molecular orbital diagram it is clear that the valence band has a major contribution from non-bonding O2p orbital whereas the conduction band has major contribution of Ti3d orbital. It is reported that in anatase TiO$_2$, valence band consists of the non-bonding O2pπ orbital which exists on the top of the valence band (VBM) and the Ti3dxy states at the bottom of the conduction bands (CBM) of TiO$_2$ [75, 76]. A similar band structure is seen in rutile also [75]. It is possible to create Density of State (DOS) diagram from the molecular orbital diagram as sown in Figure 1.18a. By understanding the band structure and position of valence and conduction band, it is easy to tune the band-gap of TiO$_2$ by using different strategies like doping and fabrication of heterogeneous structures with suitable material.
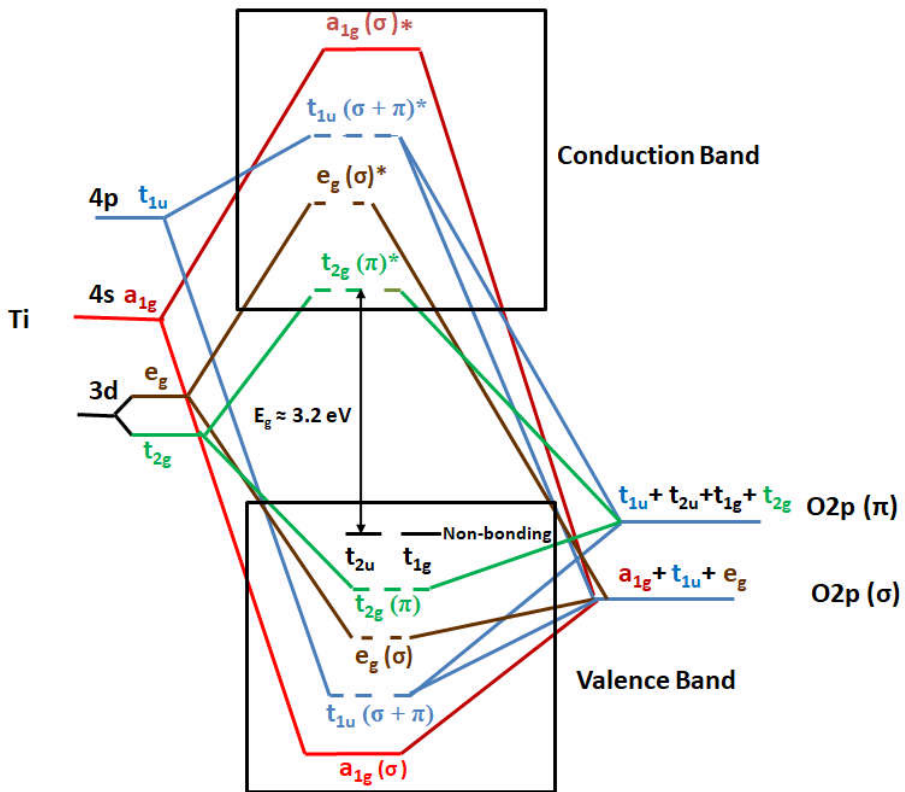
Fig. 1.17: Molecular-Orbital-diagram of anatase TiO$_2$.

N-C co-doped TiO$_2$ is a typical example for material having additional energy levels in between the valence and conduction band. Introduction of N and C introduce new energy levels within the band-gap as shown in Figure 1.18b. This additional energy bands brings down the band-gap energy to visible region [77].
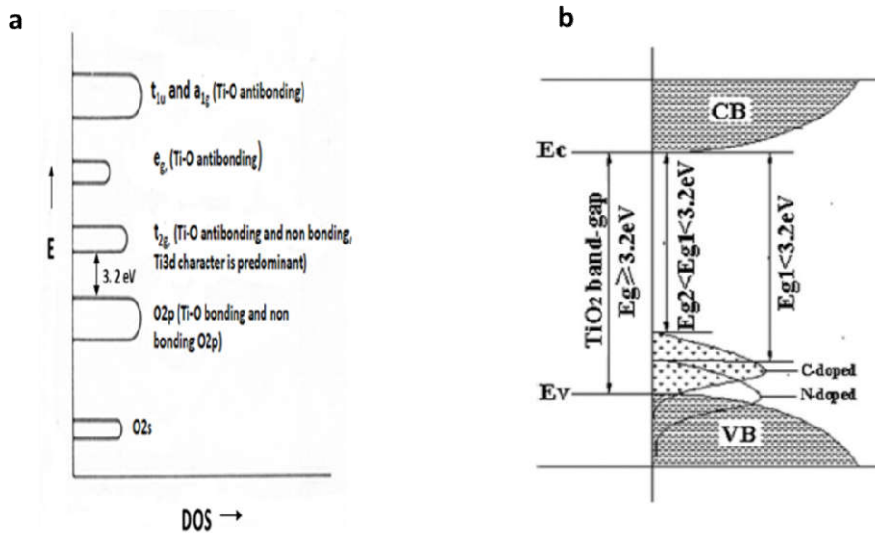
Fig. 1. 18: Schematic representation of the Density of States of a) TiO₂ and b) C-N co-doped TiO₂, showing introduction new energy bands within the band-gap.

[Source: J. Zhang et al, Development of modified N doped TiO₂ photocatalyst with metals, nonmetals and metal oxides, Energy Environ. Sci. 3 (6) (2010) 715-726]

1. 9. 3 Band-gap values of anatase and rutile

Anatase has band-gap energy of 3. 2 *eV*, where as that of rutile is 3. 0 *eV*. The band-gap difference is due to the structural dissimilarities of the two polymorphs. Even though, anatase and rutile consists of chains of TiO_6 octahedra, the arrangement of octahedral units is different in each case. In rutile structure corners of each octahedron shares with eight neighbors, and edges shares with two other neighbors forming a linear chain, while for anatase, corners and edges of each octahedra shares with four other neighbors forming a zigzag structure with a screw axes [Fig. 1. 19]. The reconstructive phase modification of anatase to rutile involves a contraction in the screw axes and an overall

volume contraction ≈ 8%. Hence anatase has less density than rutile [78]. The metal-metal bond distance in anatase is greater (5.2 A^o) than that of rutile (2.96 A^o), whereas Ti-O bond distance is smaller in anatase. These structural changes in rutile leads to pronounced localization of 3d states than anatase which is responsible for the comparatively narrow band gap of rutile (3.0 eV) compared to that of anatase (3.2 eV) [74].
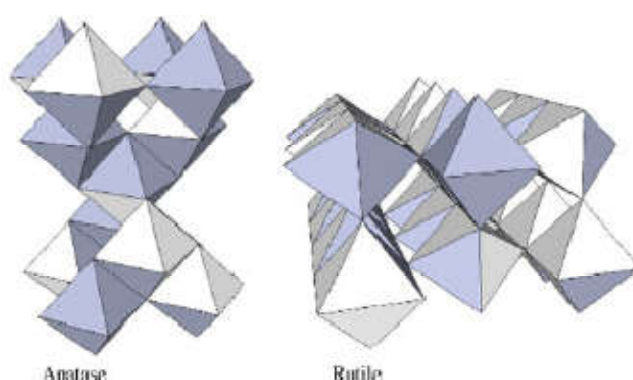
Fig. 1. 19: Schematic representation TiO$_6$ octahedra of both anatase and rutile, showing four edge sharing connectivity in anatase and two edge sharing connectivity in rutile.

[Source: D. A. H. Hanaor et al, Review of the anatase to rutile phase transformation, J. Mater. Sci. 46 (2011) 855–874]

1.10 Photocatalytic activities of anatase, rutile and brookite crystalline modification of TiO$_2$

Even though the photo absorbability of anatase is lower than rutile due to their large band gap (3.2 eV) when compared with that of rutile (3.0 eV), anatase phase exhibit higher photocatalytic activity than rutile and brookite in normal situations. This can be due to the following reasons. It is reported that anatase TiO$_2$ with (101) orientation exhibit higher

photocatalytic activity than rutile having (100), (110) orientations. Rutile with (001) orientation shows comparable activity with that of anatase having (101) orientation. Generally anatase TiO_2 consists of predominantly thermodynamically stable (101) plane, whereas the rutile consists of thermodynamically stable (110) plane. Therefore among the three polymorphic forms of titania, anatase crystals show higher photocatalytic activity [79]. The other important reasons of higher photocatalytic activity of anatase are (i) the higher surface adsorption ability of anatase to hydroxyl group; (ii) lower charge recombination rate than that in rutile; (iii) higher surface area and lower grain size of anatase particle [80, 81]; iv) wide-indirect band-gap while rutile and brookite have direct and smaller band-gap [82]. So the life time of electrons and holes is more in anatase than in the other polymorphic forms. It is also observed that in case of TiO_2 powders having more defects the brookite shows highest photocatalytic activity than other polymorphs [83]. The depth of the defect level or electron trapping center is at different positions for different polymorphs (Fig. 1.20). This defect level, due to oxygen vacancy and Ti-interstitials (trapping centers) traps the electrons and hence increases the life time of holes responsible for oxidative reaction. The trapped electrons can partially participate in reduction reaction also. The depth of the trapping center is important for optimum life time of trapped electrons as shown Figure 1.20. Comparing with anatase and rutile titania, brookite has defective trapping center at optimum depth in some case [83] and in such case brookite has highest photocatalytic activity.
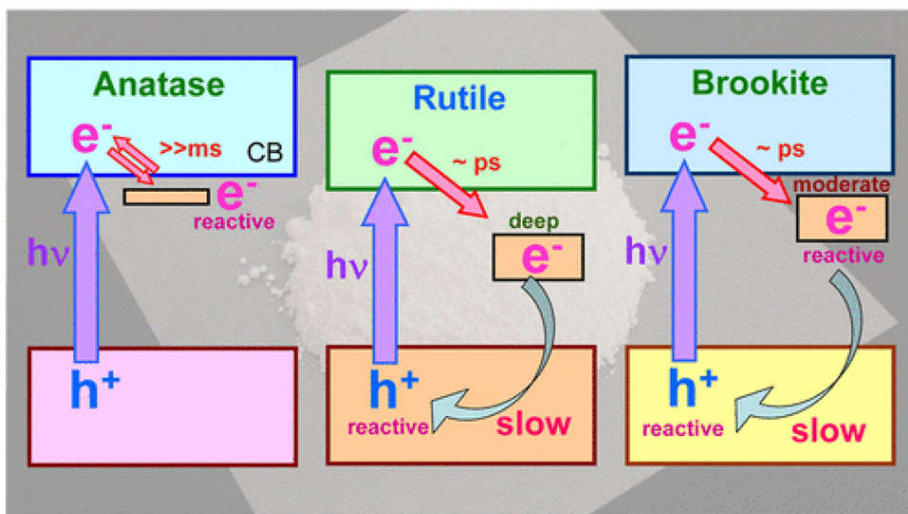
Fig. 1.20: Schematic representation of the position of defect levels (electron trapping center) in anatase, rutile and brookite.

[Source: J. J. M. Vequizo et al, Trapping-Induced Enhancement of Photocatalytic Activity on Brookite TiO$_2$ Powders: Comparison with Anatase and Rutile TiO$_2$ Powders, ACS Catal.7 (2014), 2644-2651]

1.11 Morphological features of TiO$_2$.

Morphology of the catalyst plays a crucial role in deciding its photocatalytic activity, since morphology has direct influence on its surface area, and also porosity. Among the TiO$_2$ materials, 1-D nanostructure of TiO$_2$ has attracted much interest due to their exceptional physicochemical properties [84]. The particular exposed facets and the exceptional anisotropic structure of these types of 1D nanostructures lead to the enhanced photocatalytic properties. They possess large surface/volume ratio which make them appropriate candidates for photocatalysis [85]. The important 1-D nano structures of titania are nanowires, nanosheets, nanorods, nanofibers, nanobelts and nanotubes. The enhanced photocatalytic activity of these

nanostructures is reported [86-91]. TiO_2 nanotubes are one of the important classes of titania nanostructures, due to their unique morphological features and high porosity. The electron transport property and charge separation efficiency are more in these type of nanostructure, which reduces the charge recombination rate. These properties make titania nanotube arrays as suitable candidates for photocatalytic and photoelectronic applications than the other nano-structures of titania.

A variety of methods have been used to prepare titania nanotubes such as hydrothermal treatment of TiO_2 in NaOH, template assisted method, electrospinning and anodisation method [28]. Among these methods anodisation method is the simplest and less expensive. Using anodisation method, we can fabricate well-ordered and vertically aligned nanotubes arrays having wide range of nanotube dimensions, directly attached to the Ti-substrate. Based on the fabrication process of the nanostructure, the material synthesized may be powder or film in type. If we use powder sample for air or water purification, it has some disadvantage. The powder sample requires stirring for their effective dispersion and then for effective degradation of the pollutants present in water. The separation of photocatalyst in powder form, after reaction, is difficult. Hence it is more advantageous to use thin films immobilized on a substrate for improved photocatalytic efficiency. Considering the above facts we selected nanostructured titania nanotube arrays which were fabricated by anodisation method as the base material for this research work. Titania nanotube synthesized by anodisation method has advantages of having 1D nanostructures and

whose tubular parameters can be controlled effectively and easily. Also they can be obtained in thin film form where the titania nanotubes are vertically aligned perpendicular to the substrate surface. Not only that the fabrication process of titania nanotube arrays through anodisation is relatively simple and less expensive.

1.12 Titania nanotube arrays (TNTAs)

The important advantages of TNTAs are that the dimensions of TiO_2 nanotubes can be exactly tuned by controlling the anodisation parameters. It is possible to fabricate uniform TiO_2 nanotubes of various pore sizes (20-100 *nm*), lengths (0.2-1000 *μm*), and wall thicknesses (10-30 *nm*). The obtained nanotube film will offer new chances to design various 1D TiO_2-related useful material systems by doping, deposition, and sensitization, due to their large specific surface area, high pore volume, and appropriate morphology [92]. All the above mentioned properties make TNTAs as suitable candidates for photocatalytic applications.

1.12.1 Anodisation process/ Fabrication process of TNTAs

We can fabricate well-ordered and vertically aligned TNTAs through potentiosatic anodisation process. The anodisation (electrochemical) process comprises of applying a constant potential between the titanium metal foil and the platinum counter electrode in an ethylene glycol-fluoride electrolyte solution. The titanium metal foil acts as the anode whereas the platinum electrode acts as the cathode. The schematic diagram of a typical anodisation set up is provided in Figure 1.21. The first report about the fabrication of TiO_2 nanotube arrays

through anodisation was reported in 1999 [93]. Subsequent research works have focused on the modification of the anodisation process by changing the electrolyte and other anodisation parameters to optimize the anodisation conditions which are discussed in detail in the following sections. These studies also helped in a better understanding of the effect of anodisation parameters on the tubular morphology.
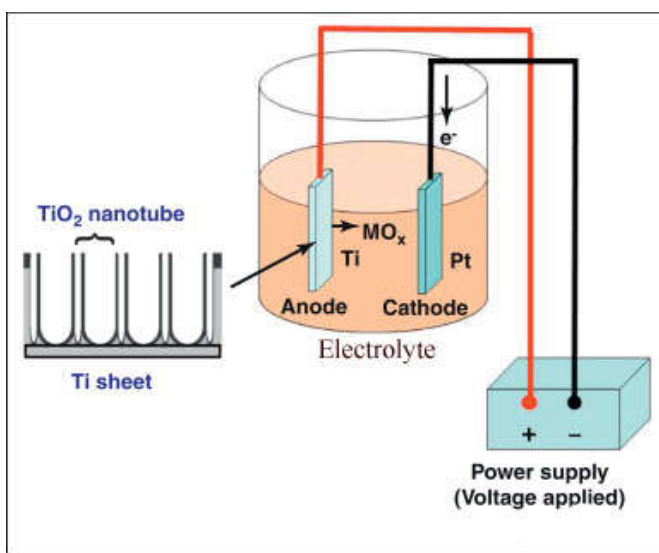
Fig. 1. 21: Schematic representation of electrochemical anodisation process used to fabricate TNTAs on Ti metal foil.

[Source: K. S. Brammer et al, TiO$_2$ nanotubes for bone regeneration, Trends. Biotechnol. 30 (2012) 315-322]

1.12.2 Mechanism of TNTAs formation

The mechanism of TNTAs formation during potentiostatic anodisation process in fluoride ion based electrolyte consists of three steps; the field aided oxidation of Ti metal to form TiO$_2$. The field helps dissolution of Ti metal in the electrolyte and the chemical dissolution of Ti and TiO$_2$ due to etching by fluoride ion, which is promoted by H$^+$

ions [94]. Naturally Ti-metal foil has a thin layer of TiO_2. The formed TNTAs are aligning on this thin TiO_2 layer of Ti-metal substrate. Hence the mechanism of TNTAs formation is associated with oxidation and dissolution kinetics. The mechanisom of TNTAs formation is depicted in the following Figure 1.22.
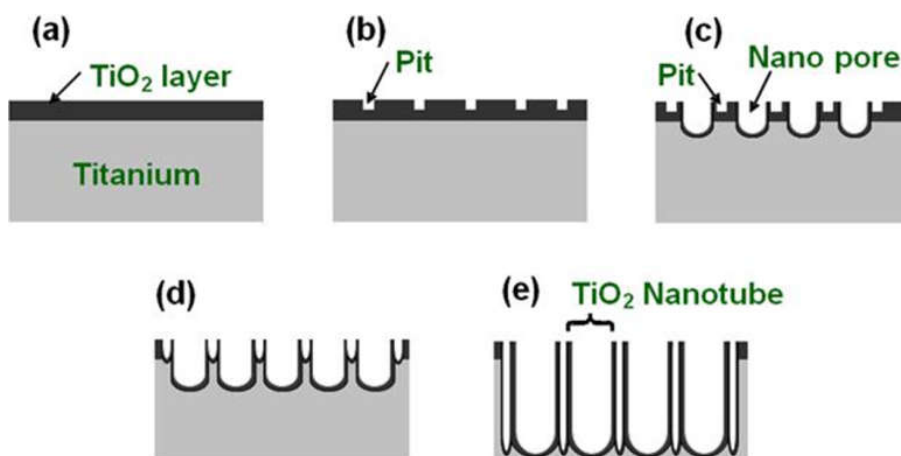
Fig. 1.22: Mechanism of TiO_2 nano tube array formation, where (a) naturally occurred thin TiO_2 layer on Ti-metal substrate (b) forming of pits on TiO_2 layer due to the constant potential applied (c) the pits are growing larger as the anodisation time increases (d) barrier layer formation of the small pits and nanopores (e) completely developed TiO_2 nanotube after the optimum anodisation time.

[Source: K. S. Brammer et al, Biomaterials and Biotechnology Schemes Utilizing TiO_2 Nanotube Arrays in Biomaterials Science and Engineering. eds. R. Pignatelo, 2011, InTech publishers.]

1.12.3 Nature of electrolyte

The electrolyte used in anodisation process control the formation and the dissolution of the oxide layer. The rate of the dissolution process control the pore formation which affects the formation of TiO_2 nanotubes. Mainly three different kinds of electrolytes have been reported in literature. Electrolytes made up of aqueous HF solutions

were the first kind. The pH of this HF based solution is slightly acidic (pH-5), and the length of the nanotubes in this case is approximately 500 *nm* [95]. Second type of electrolyte used was buffered aqueous solution at higher pH, in this case NaF or KF was used as the source of F ions. At high pH value the hydrolysis rate of Ti is more and hence the dissolution rate decreases which leads to the formation of longer TiO_2 nanotubes. Hence using this solution it is possible to increase the tubular length up to micron length [96]. The third type of electrolyte solution, which is commonly used nowadays, consists of polar organic electrolytes such as ethylene glycol, dimethyl sulphoxide with or without water. Ammonium fluoride is commonly used as the source of F ions in these electrolytes. The length of the TNTAs obtained by using these types of electrolytes varies from $\approx$15-200 *nm* [97].

1.12.4 Importance of fluoride-ions in the electrolyte.

The concentration of fluoride ions in the electrolyte solution used for the anodisation process has a key role to decide the tubular structure and tubular parameters. In the absence of fluoride ions a compact layer of TiO_2 is formed on the substrate as shown Figure 1.23a. After the beginning of anodic oxidation process, the development of an anodic oxide layer is controlled by the field-assisted transfer of mobile ions through the oxide layer as shown Figure 1.23b. Fluoride ion concentration in the electrolyte strongly influences the anodisation process, as the fluoride ions react with Ti^{4+} to form easily water soluble $[TiF_6]^{2-}$. F ions complex with Ti^{4+} ions that are ejected to the oxide-electrolyte interface or by the direct attack of the fluoride ions at the TiO_2 layer as indicated by the equations 1. 11 and 1. 12 given below [98].

$$\text{Ti}^{4+} + 6\text{F}^- \longrightarrow [\text{TiF}_6]^{2-} \text{————————1.11}$$

$$\text{TiO}_2 + 6\text{F}^- \longrightarrow [\text{TiF}_6]^{2-} + 2\text{H}_2\text{O} \text{————————1.12}$$
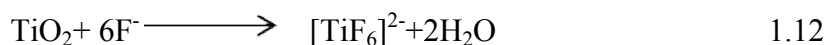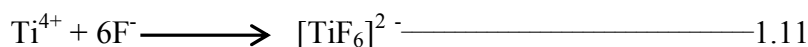
Optimum concentration of fluoride ion in the electrolyte is needed for the formation of TiO$_2$ nanotubes. If the fluoride ion concentration is very low (≤ 0.05 *wt* %), characteristics as observed in the fluoride free case are observed [98]. If the fluoride concentration is more, oxide generation is not observed. When the concentration of fluoride ion is high, all the Ti^{4+} formed directly react with F$^-$ ions to form $[\text{TiF}_6]^{2-}$, which is soluble in water. For optimum intermediate concentration of fluoride ion, a competition among oxide formation and Ti^{4+} solvatization takes place which leads to the formation of TiO$_2$ nanotubes [99]. Thus the accumulated fluoride layer at the oxide-metal interfaces and at grain boundaries plays an important role during the transition from a porous hexagonal structure to a tubular structure.
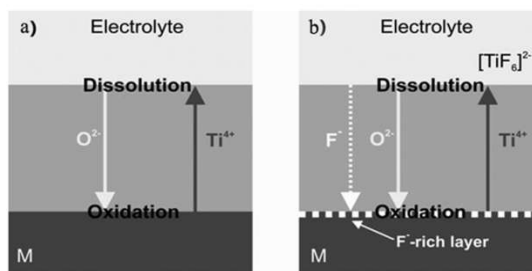
Fig. 1.23: Schematic representation showing field assisted transport of mobile ions through the oxide layers a) in the absence of fluoride ions b) in the presence of fluoride ions.

[Source: P. Roy et al, TiO$_2$ Nanotubes: Synthesis and Applications, Angew. Chem. Int. Ed. 50 (2011) 2904 – 2939]

1.12.5 Factors influencing the parameters of TiO$_2$ nanotube

All the parameters that affect the anodisation process greatly influence the tubular dimensions of titania nanotubes. As already discussed, the type of electrolyte and the pH of the electrolyte play crucial roles in determining the dimensions of TiO$_2$-nanotubes. In addition to these the important parameters that affect the TiO$_2$ nanotube structures are electrolyte temperature, current density and anodisation time [100]. The nature or the type of electrodes used also has a role to modify the structural parameters of TiO$_2$ nanotubes. Normally up to a temperature of 40^0 C well oriented tubular structure is obtained, above 40^0 C unstable bundles of nanotubes are formed on the Ti-surface [101, 102]. Up to 40^0 C as we increase the temperature of electrolyte, the pore size increases due to the fast etching rate by the fast movement of F$^-$ion. Current density also influences the pore size of titania nanotubes, as the current density increases etching rate, intensity of electric field and power also increases [100, 103]. This may responsible for the pit widening, before the formation of channels and pores are formed separately, hence as the current density increases the pore size of nanotube materials can also be improved. Anodisation time has also an important role to decide the tubular parameters. A minimum time duration (15 *min)* is needed for the tubular formation in the anodisation process [104], and by extending the anodisation time, highly ordered tubes can be produced, the length of the nanotube can also be increased by extending the anodisation time [104]. Counter electrodes that are used as cathode during anodisation, has its own role to decide the aspect ratio of nanotubes. Studies conducted by researchers using

various cathode materials like iron, carbon, stainless steel, aluminum, nickel, platinum, palladium, cobalt, copper, tungsten, and tin proves that the dimensions and the arrangements of titania nanotubes on Ti metal foil is greatly influenced by the type of the counter electrode that are employed during the anodisation process [105, 106]. The distance between the electrodes also determines the pore size, and the morphology of the titania nanotubes fabricated by anodisation process [107].

1.13 TiO$_2$ nanotubes-modifications for photocatalytic applications

The importance and the applicability of TiO$_2$ as a photocatalyst is well known. The morphology of the photocatalyst has an important role to decide the photocatalytic activity of the materials. We can easily tune tubular dimensions of titania nanotubes by changing the anodisation parameters. Hence TiO$_2$ nanotubes are one of the best materials to study both the influence of material morphology and the effect of surface modifications on the photocatalytic activity of a material. The initial attempt to fabricate TiO$_2$- nanotubes was started only in 1999. After that researchers have succeeded in obtaining well-ordered titania nanotubes of desired length, pore size and wall thickness by varying the electrolytes and parameters used in the anodisation process. A lot of research work related with the photocatalytic application of titania nanotubes are reported by making use of the advantages of its morphology and the film nature. Modifications done on the titania nanotubes were also reported to increase the photocatalytic activity of nanotube materials or to extend the application region of the material. One of the best methods that is adopted for enhancing the

photocatalytic activity is the construction of heterogeneous nanostructures with suitable materials.

1.13.1 Heterogeneous nanostructures of TiO$_2$ nanotubes

The mechanism and principle of heterogeneous nanostructures involved in the photocatalytic process have already been discussed. The important heterogeneous nanostructures of TiO$_2$- include the modification of TiO$_2$ nanotube arrays with semiconductors like CdS [108-111], PbS [112, 113], CdSe [114, 115], Ag$_2$S [116], Fe$_2$O$_3$ [117], NiO [118], TiO$_2$ [119], ZnO [120-123] and graphene [124].

1.13.1.1 Modification of TiO$_2$ nanotube array with CdS

Different methods were adopted to modify the TiO$_2$-nanotube arrays with CdS nanoparticles, like cathodic reduction [108], close space sublimation technique [109], sequential chemical bath deposition (S-CBD) [110], and electrochemical atomic deposition [111]. The fabricated photoelectrode or catalyst of CdS@TiO$_2$-nanotube heterostructure shows enhanced photocatalytic activity for degrading organic dyes under visible light irradiation. The improved activity is due to the extended visible light absorption of CdS particle and the separation of photogenerated electrons and holes that improves the photoactivity of modified TiO$_2$-nanotube arrays.
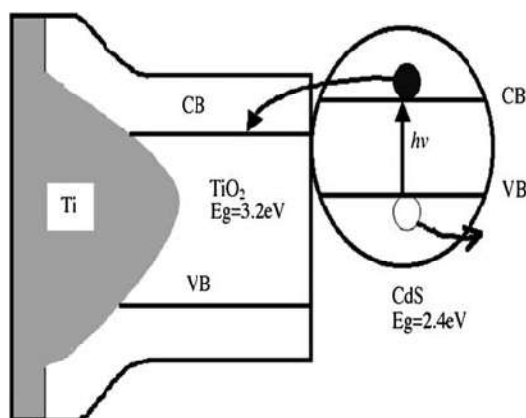
Fig. 1.24: Illustrative diagram of charge transfer from CdS to TiO₂ (TiO₂ grown on Ti-metal substrate).

[Source: S. Chen et al, Electrochemically synthesized CdS nanoparticle-modified TiO₂ nanotube-array photoelectrodes: Preparation, characterization and application to photoelectrochemical cells, J. Photochem. Photobiol. 177 (2006) 177-184]

1.13.1.2 Modification of TiO₂ nanotube arrays with PbS

Q. Kang et al reported that TiO₂-nanotube arrays can be effectively modified with PbS [112] nanoparticles to extend the photocatalytic activity of TiO₂ nanotubes to the visible region of solar spectrum. In this study, successive ionic layer adsorption and reaction method (SILAR) was used to deposit, PbS particle on TiO₂-nanotubes. PbS plays an important role in enhancing the charge separation in the heterogeneous nanostructure with TiO₂. The increased photocurrent in the visible light region in this case is attributed to enhanced charge separations, improved electron transport and increased visible light absorption (band-gap of PbS-0.88 *eV*). But for significantly large PbS particle size, the activity has been reported to be decreased. This may be due to the decrease in band-gap energy leading to faster electron-

54

hole recombination. N. B. Rahna et al prepared PbS sensitized TiO_2 nanotube arrays by SILAR method and studied the visible light photocatalytic activity of these heterostructures [113]. The amount of PbS particles on TiO_2 nanotube arrays were varied by changing the number of SILAR cycles. The maximum photocatalytic activity was observed for PbS@TiO_2 when 3 SILAR cycles were used for PbS deposition. The recyclability of these heterostructures was also studied. It was reported that the efficiency of the heterostructure depends upon the amount of PbS particles on the surface of TiO_2. At an optimum amount of PbS, the heterostructure exhibits maximum photocatalytic activity. They also noted that as number of SILAR cycle increases the amount of PbS particle increases which contain fraction of large and small particles. The size and stability of this PbS layer on the surface of TiO_2 was also analyzed by X-ray Photoelectron Spectroscopy and reported.

1.13.1.3 Modification of TiO_2-nanotube arrays with CdSe

Heterogeneous nanostructure of CdSe@TiO_2-nanotube array found applications in visible light region due to the visible light absorption of CdSe. Direct current electrotechnique was employed by L. Yang et al for depositing CdSe nanoparticles on TiO_2-nanotube arrays. CdSe nanoparticles were deposited in inner, outer and on the top surface of TiO_2 nanotubes. The applied deposition voltage plays a crucial role for the formation of CdSe particles. The fabricated heterostructure exhibited enhanced visible light absorption due to the lower band-gap of CdSe and also steady photocurrents on visible light irradiation. CdSe modified TiO_2 nanotube arrays also exhibited enhanced

photocatalytic activity under 550 *nm* green light irradiation than that of pure TiO_2 suggesting the applicability of this heterostructure [114]. In situ deposition of CdSe, during the fabrication of TiO_2-nanotube array was also reported recently for photocatalytic application [115]. The authors studied the photocurrent and photoelectrocatalytic properties of these heterostructures. This composite material exhibited enhanced photocurrent density and photoelectrocatalytic activity than that of pure TiO_2 nanotube arrays. This enhanced properties is attributed to the synergistic effect of the nanotubular morphology and effective separation of charge carriers in the heterogeneous nanostructure [115].

1.13.1.4 Modification of TiO₂-nanotube arrays with Fe₂O₃

Modification of TiO_2 nanotube arrays by dextrin coated Fe_2O_3 has been studied. The anodized TiO_2 nanotubes were dipped in the dextrin coated iron oxide solution by simple dip coating method. Fe_2O_3 particles are deposited on the top walls of the nanotube arrays. The composite structure simultaneously shows enhanced UV photocatalytic activity and light independent wetting properties. $Fe_2O_3@TiO_2$ also exhibited magnetization anisotropy. The individual nanoparticles arranged at the top of the nanotubes undergo dipolar coupling, which is responsible for the magnetization anisotropy of the composite material. The enhanced charge separation in the composite structure was responsible for the enhanced photocatalytic activity of the modified TiO_2-nanotube arrays. The polyhydroxyl dextrin shell act as an intermediate for the charge transfer in between the constituent semiconductors of the heterostructure [116].

1.13.1.5 Modification titania nanotube arrays with Ag$_2$S

Ag$_2$S particles were deposited on TiO$_2$-nanotube arrays by successive ionic layer adsorption and reaction (SILAR) method. The distribution and morphology of Ag$_2$S particles depends on the number of SILAR cycles, employed for Ag$_2$S deposition. Maximum photoelectrocatalytic activity under solar-light illumination was observed for the Ag$_2$S@TiO$_2$-nanotubes with 10 SILAR cycles of Ag$_2$S deposition due to the uniformly distributed Ag$_2$S particle on TiO$_2$-nanotubes [117]. Ag$_2$S modified TiO$_2$-nanotube arrays shows enhanced visible light photocatalytic activity.

1.13.1.6 Modification of TiO$_2$-nanotube arrays with NiO nanoparticles

TiO$_2$ nanotube arrays were modified with NiO particles with simple chemical bath precipitation method followed by annealing at different temperatures ($450^0\,C$, $550^0\,C$, and $630^0\,C$) [118]. NiO nanoparticles modified TiO$_2$ nanotube arrays, annealed at $550^0\,C$, exhibited enhanced visible light photoresponse and photocatalytic activity than that of unmodified TiO$_2$-nanotube arrays due to charge migration from NiO to the conduction band of TiO$_2$. The photocatalytic activity and photoresponse of NiO modified sample annealed at $450^0\,C$ and $630^0\,C$ was less than that of sample annealed at $550^0\,C$, due to poor crystallinity of NiO at $450^0\,C$ and high rutile content of TiO$_2$ at $630^0\,C$.

1.13.1.7 Modification of TiO$_2$ nanotube arrays with TiO$_2$

P. Roy et al reported the modification of TiO$_2$-nanotube arrays with TiO$_2$ by simple hydrolysis process in a precursor solution of TiCl$_4$ [119]. The samples obtained are calcined at 350^0 C and 450^0 C to crystallize the TiO$_2$ sample attached to the TiO$_2$ nanotube arrays. In this case, the synthesised TiO$_2$ nanotubes were in anatase phase whereas the deposited TiO$_2$ nanoparticles contained both anatase and rutile phase in which the anatase phase is predominant. TiO$_2$ nanoparticles of average size of 3 *nm* were able to deposit inside and outside the wall of TiO$_2$-nanotube arrays by this method. The modified TiO$_2$-nanotube array shows higher solar cell efficiency due to the significantly increased surface area of the composite material. The observations in this work suggest that the sample annealed at 350^0 C has optimized efficiency in terms of electron collection and the sample annealed at 450^0 C has optimized anchoring efficiency for the dye on the surface TiO$_2$ nanotube.

1.13.1.8 Modification of TiO$_2$ nanotube arrays with ZnO

Recently heterogeneous nanostructure of ZnO@TiO$_2$ has attracted much interest in photocatalytic applications, because of the suitable band-gap properties and low toxicity of these materials. ZnO@TiO$_2$-nanotube heterostructure including, nanocomposites of ZnO nanorods and TiO$_2$ nanotubes has been studied [120]. Y. Lei et al deposited ZnO nanorods on TiO$_2$ nanotube arrays and studied its photoelectrocatalytic and photocurrent properties. The obtained ZnO@TiO$_2$ heterostructures exhibited enhanced photoelectrocatalytic activity, photocurrent density

and stability than that of pure TiO_2. The increased activity is due to the effective separation of electrons and holes in the heterogeneous nanostructure [121]. Z. Zhang et al used cathodic electrodeposition method to deposit ZnO nanorods on TiO_2 nanotubes. The authors also observed enhanced photocurrent density and photoelectrocatalytic activity for the heterostructure [122]. ZnO nanoparticles impregnated in TiO_2-nanotube arrays have also been studied [123]. In this work ZnO nanoparticles are uniformly deposited on TiO_2 nanotube through pyrolysis method. The heterogeneous nanostructure exhibited improved photocatalytic activity and photostability under UV light than that of pure TiO_2, ZnO and P-25 particulate film due to the effective charge separation in the heterogeneous nanostructure.

1.13.1.9 Modification of TiO_2-nanotube arrays with graphene

Graphene oxide is a unique material due to its high electrical conductivity, high surface area and high electron mobility. P. Song et al reported the construction and application of GO (graphene oxide) modified TiO_2 nanotube arrays [124]. The photoelectrical properties of the composite material was investigated and reported that the GO@TiO_2-nanotube arrays exhibited enhanced visible light photoelectrochemical and photocatalytic properties due to the above mentioned unique properties of graphene than that of pure TiO_2-nanotube. Above studies clearly proves the advantages of heterogeneous nanostructures of TiO_2-nanotubes for photocatalytic applications.

1.13.1.10 Multicomponent Ag$_2$S/TiO$_2$/CdS-nanotube arrays heterostructure.

H. Sun et al reported the construction of Ag$_2$S/TiO$_2$/CdS multicomponent heterostructure of TiO$_2$ nanotube arrays [125]. CdS nanoparticles were deposited on TiO$_2$ nanotube arrays by successive ionic layer adsorption and reaction (SILAR) method whereas both spotting sample and SILAR methods were used to deposit Ag$_2$S particle on CdS/TiO$_2$ nanotube arrays. The multicomponent Ag$_2$S/TiO$_2$/CdS heterostructure exhibited improved visible light absorption and high photocurrent density, 37 times than that of pure TiO$_2$ nanotube arrays. The enhanced activity was due to the visible light absorption of Ag$_2$S particle and the decreased recombination probability of electrons and holes in the multicomponent heterostructure. The schematic representation of photovoltaic conversion Ag$_2$S/TNTs/CdS is provided in Figure 1.25.
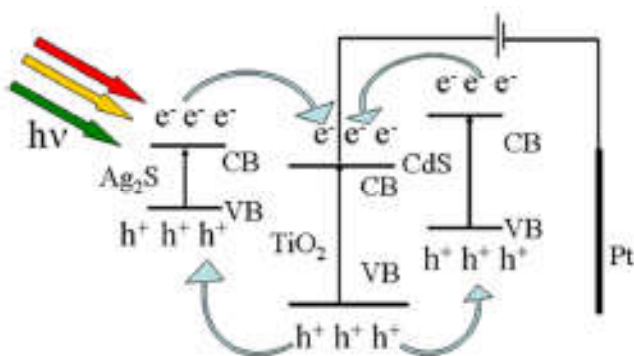
Fig. 1.25: Schematic representation of photovoltaic conversion of Ag$_2$S/TNTs/CdS heterostructure.

[Source: H. Sun et al, Ag$_2$S/CdS/TiO$_2$ Nanotube Array Films with High Photocurrent Density by Spotting Sample Method, Nanoscale. Res. Lett.10 (2015) 382]

The conduction band and valence band of CdS is located above the conduction band and valence band of TiO_2. Hence the photogenerated electrons in the conduction band of CdS is transferred to the conduction band of TiO_2 whereas the holes are transferred from valence band of TiO_2 to that of CdS. Similar electron and hole transfers take place between the bands of Ag_2S and TiO_2. Thus the transfer of electron and hole prevents the recombination of electron-hole pairs in the heterostructure and shows enhanced photocurrent density. The smaller band-gap of Ag_2S extends the absorption of the multicomponent heterostructure to visible light region.

1.13.2 Doped TiO_2-nanotube arrays

Doping is a widely used technique to alter the properties of materials. Especially the dopants may introduce energy levels in between the valence band and conduction band as shown in Figure 1.26. In addition some doped ions may be responsible for surface plasmonic effects and enhance charge transfer. Nitrogen is one of the most extensively used dopant to improve the photoresponse of TiO_2-nanotube arrays. The extended visible light absorption of nitrogen and the defect states formed within the band-gap responsible for the enhanced and extended photocatalytic activity in N-doped titania nanotube arrays have been reported [126-131]. The other dopants that are widely used to improve the photocatalytic applications of TiO_2-nanotube arrays include Si [132], B [133, 134] C [135], Fe [136, 137], Cr [138], Zr [139], W [140], Ag [141-143], and noble metals like Au, Pt and Pd [144]. Besides this, co-doped systems containing multiple dopants have also been fabricated for extended and improved application of TiO_2 nanotube arrays [145-147].
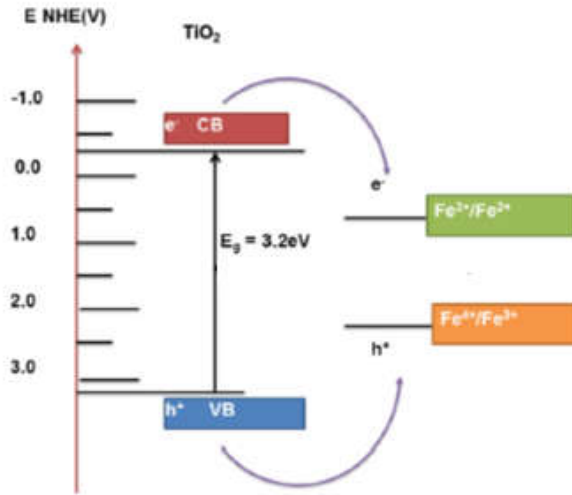
Fig. 1.26: A typical example for defective band structure of Fe doped TiO$_2$.

[Source: L. Sun et al, An electrochemical strategy of doping Fe^{3+} into TiO$_2$ nanotube array films for enhancement in photocatalytic activity. Sol. Energy Mater. Sol. C, 93 (2009), 1875–1880]

1.14 Other modifications

It is also possible to convert such TiO$_2$ nanotube arrays to nanotube arrays of materials like BaTiO$_3$ and, SrTiO$_3$ which belongs to the class of ABO$_3$ type Perovskites, by simple methods like hydrothermal synthesis [148, 149]. In the ABO$_3$ structure, A represent large divalent cations (here Ba and Sr) and B represent small tetravalent cation (here Ti); These ABO$_3$ type Perovskite structures are emerging as potential candidates for photocatalytic and solar cell applications due to its tunable band-gap property [19, 150-154]. Properties of ABO$_3$ structure is decided by the type of ions occupying the A and B site of the cubic structure. Substitution at both A and B or any one of the sites may change the properties of the perovskite. This substitution may create oxygen vacancy or donor levels, which may introduce energy levels

within the band-gap of perovskite. Thus, appropriate doping can be employed to tune the band-gap of perovskite materials [19, 150]. Band-gap engineering strategies in perovskite materials, include substitution of tetravalent ions at the B-site with aliovalent ions like $Rh^{3+/1+}$, $Mn^{3+/2+}$, $Ru^{3+/2+}$, Ir^{3+}, Cu^{2+}, Ni^{2+}, Pt^{2+} as well as construction of heterogeneous nanostructures consisting of two components for enhanced visible light absorption [20, 152, 155]. Many important ferroelectric materials also belong to the class of Perovskites. It has been reported that the inherent ferroelectricity of Perovskite type oxides like $BaTiO_3$ is responsible for the creation of internal polarization, which assist to enhance the photocatalytic rate by promoting the prevention of electron-hole pair recombination as shown in Figures1.27a and 1.27b. Ferroelectric materials have the property of spontaneous polarization. Displacement of center of negative and positive charges in the unit cell results in spontaneous polarization and the polarization creates macroscopic charges on the surface of ferroelectric material. This charge is compensated by defects and free charge carriers in the material or this charge can be externally compensated by the adsorbed charged molecule from the surroundings (Fig. 1.27a). If the spontaneous polarization is directing from the bulk to the surface, it will create a positive charge (C^+) on the surface and if it is from surface to bulk, it creates a negative charge(C^-) in the surface. The internal depolarization field will lead to accumulation of electrons near the C^+ surface resulting in downward band bending. In the (C^-) region, electrons flow away, resulting in upward band bending. This is illustrated in Figure. 1.27b. Thus the band bending, due to ferroelectricity, will effectively lead to the separation of charge carriers, which helps to prevent the recombination of electrons and holes. Ferroelectricity also helps to bind the dye molecule on material

63

surfaces tightly [156-158]. One ferroelectric material extensively investigated for such applications is BaTiO$_3$ [159, 160]. So BaTiO$_3$ is one of the suitable candidates for studying photocatalytic properties by taking advantages of both the structural features of the perovskite as well as its ferroelectric nature.
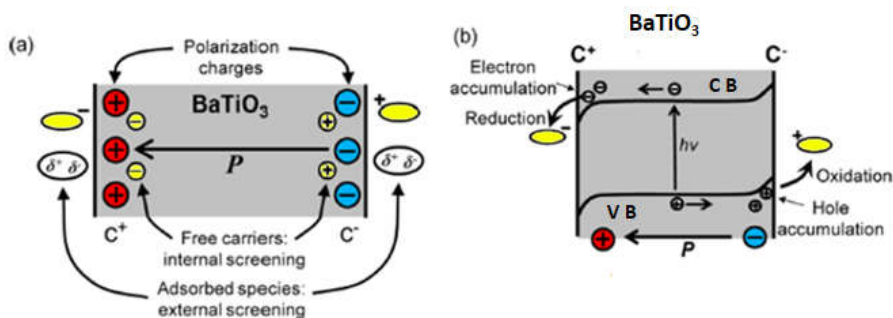
Fig. 1.27: Schematics representation of, a) internal electrical polarization in a ferroelectric material and b) band-bending due to accumulation of charges on the surfaces.

[Source: Y. Cui et al, Effect of Ferroelectricity on Solar-Light-Driven Photocatalytic Activity of BaTiO$_3$-Influence on the Carrier Separation and Stern Layer Formation, Chem. Mater. 25 (2013)4215−4223]

1.15 Structure of BaTiO$_3$

BaTiO$_3$ belongs to the ABO$_3$- type perovskite structure. The structure can be described in terms of a simple cubic unit cell with large divalent cation A (here Ba) in the corners, the small tetravalent B (here Ti) in the body center and oxygen (O) in the centers of the faces. A typical unit cell of BaTiO$_3$ is provided in Figure 1.28. BaTiO$_3$ adopts different crystalline phases like simple cubic, tetragonal, orthorhombic, rhombohedral or hexagonal structure.
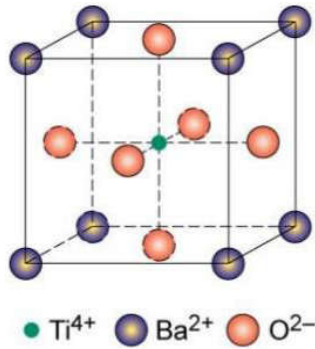
Fig. 1. 28: Unit cell representation of BaTiO₃.

1.15.1 Band structure of TiO₆ in BaTiO₃

In the cubic structure of $BaTiO_3$, Ti^{4+}-ion, which is at the center of cube, is surrounded by $6O^{2-}$ anions to form a TiO_6 octahedron. The band structure of $BaTiO_3$ can be understood from the molecular orbital diagram of TiO_6 shown in Figure 1. 29.

$BaTiO_3$ has a band gap energy of≈ 3.2 *eV*. The valence band mainly consists of O2p-nonbonding states. The band is extended by mixing this O2p nonbonding states with molecular -π and σ bands. Similarly the Conduction band has dominant contribution from Ti3d states, containing σ* and π* molecular orbital [161]. Molecular orbital diagram also helps to understand the covalent character of bonding involved between Ti and O in $BaTiO_3$. It has been reported that in $BaTiO_3$ the bonds between Ba and O is ionic whereas Ti and O is covalent in character [162].
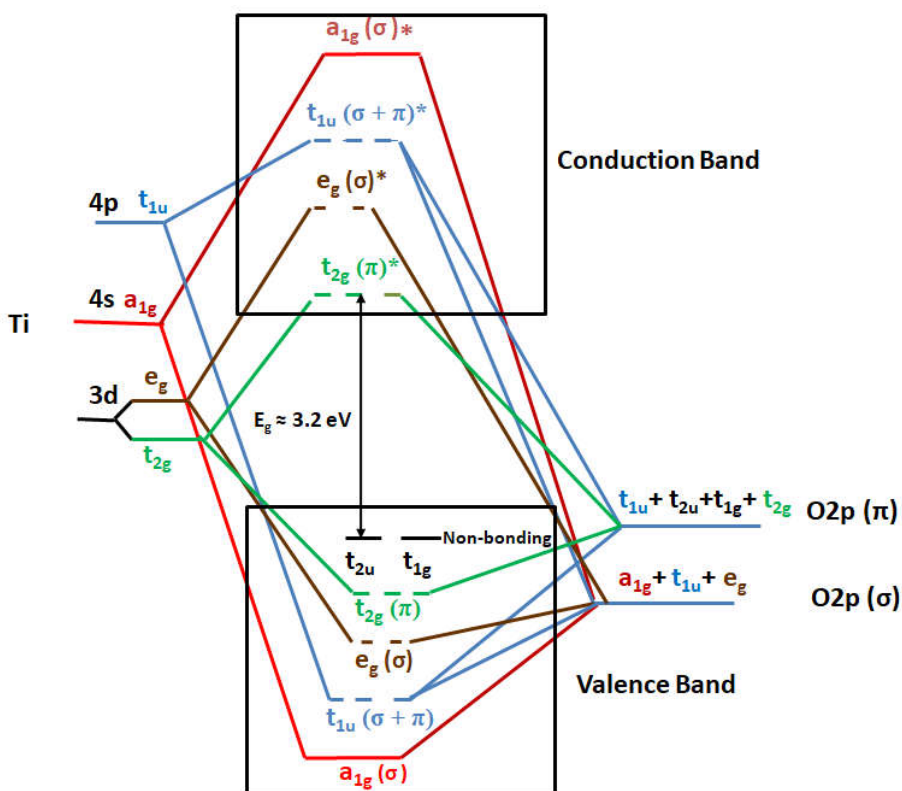
Fig. 1. 29: Molecular orbital diagram of TiO$_6$ octahedra in BaTiO$_3$ showing both σ and π bonding.

1.16 Photocatalytic properties of BaTiO$_3$

The band-gap of BaTiO$_3$ is ≈3.2 *eV* which can absorb UV radiations of solar spectrum. This band-gap can be tunable to extend its application in Visible/IR region. Besides this, properties like photostability, non-toxicity and ferroelectric character makes BaTiO$_3$ an appropriate candidate for photocatalytic applications. There are so many studies and applications based on the photocatalytic properties of TiO$_2$, but the photocatalytic applications of ferroelectric materials still needs exploitation. In order to increase the life time of active species and extend the photon absorption to visible light region, modification in the

band structure of $BaTiO_3$ is needed. One of the strategies that has been employed to engineer the band-gap of $BaTiO_3$, to enhance its photocatalytic activity is the fabrication of heterogeneous nanostructures with suitable materials like graphene [20,163]. In ferroelectric $BaTiO_3$, its visible light driven photocatalytic activity can also be enhanced through substitution of A^{2+} and B^{4+} cations in the ABO_3 perovskite structure with aliovalent ions. Mn-doped $BaTiO_3$ is a typical example having defect energy levels within the band-gap as a result of such doping [164]. The schematic representation of density of states for the Mn-doped $BaTiO_3$ is provided in Figure1.30. This clearly demonstrates that doping with suitable elements introduces energy levels due to defects within the band-gap of $BaTiO_3$. Modification of band-gap of $BaTiO_3$,doped with Rh^+, Zn^{2+}, Y^{3+}, and Ag^+ have already been reported. Their photocatalytic applications have also been reported [159, 165-167].
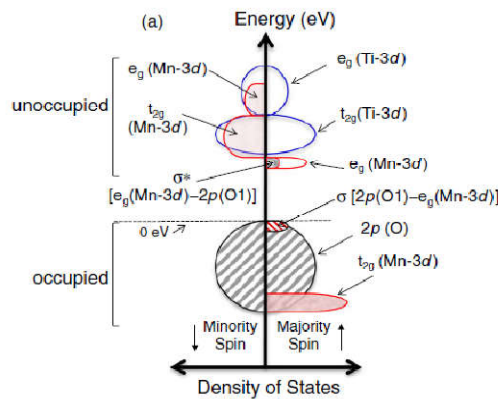
Fig. 1.30: Schematic representation of Density of States of Mn-doped BaTiO₃.

[Source: R. Inoue et al, Photocurrent Characteristics of Mn-Doped Barium Titanate Ferroelectric Single Crystals, Jpn. J. Appl. Phys.52 (2013) 09KF03 (1-6)]

1.16.1 Modification of BaTiO$_3$-nanotube arrays

BaTiO$_3$ nanotube arrays have more advantages, because the dimensions of nanotubes can be effectively tuned. Though the fabrication of BaTiO$_3$ nanotubes has been reported only very few studies have been reported on the modification of BaTiO$_3$ nanotube arrays for photocatalytic applications. Ag-modified BaTiO$_3$ was reported by Liu et al [167]. Photocatalytic activity was demonstrated by studying the degradation of methyl orange in UV-light. It was observed that the Ag-loaded BaTiO$_3$ nanotubes show maximum photocatalytic activity at low pH. The enhanced photocatalytic activity was attributed to the effective charge separation in Ag-modified BaTiO$_3$-nanotubes due to the Schottky barrier formed in between Ag and BaTiO$_3$-tubes.

R. Li et al fabricated heterogeneous nanostructure of BaTiO$_3$ nanotube array with TiO$_2$ for photocatalytic applications [168]. They synthesized this heterostructure by hydrothermal method and studied the photocatalytic degradation of methylene blue as a model dye. The heterogeneous nanostructure exhibits enhanced UV photocatalytic activity due to increased life time of active species as a result of the heterogeneous nanostructure formed in between TiO$_2$ and BaTiO$_3$-nanotubes as shown in Figure 1.31.
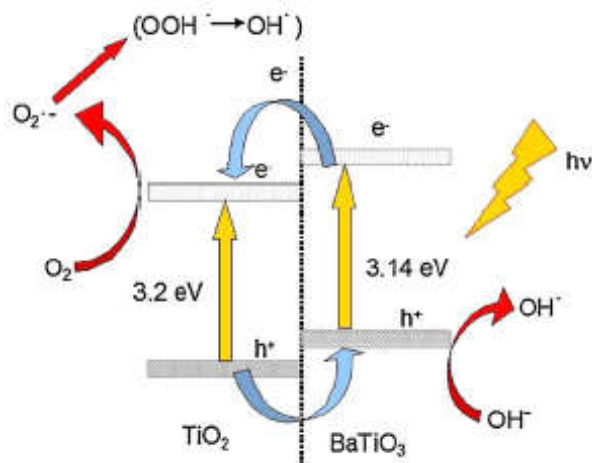
Fig. 1.31: Heterogeneous nanostructure formed in between TiO$_2$ and BaTiO$_3$.

[Source: R. Li et al, BaTiO$_3$/TiO$_2$ heterostructure nanotube arrays for improved photoelectrochemical and photocatalytic applications, Electrochim. Acta. 91 (2013) 30-35]

1. 17 Present research work

From the detailed discussions of the principle, mechanism and advantages of semiconductor photocatalytic process, it is clear that photocatalysis is a suitable process to remove impurities from the environment, especially the organic pollutants present in the water. Among the semiconductors, TiO$_2$ has all the properties that a good photocatalyst should possess. Even though TiO$_2$ is a best candidate for photocatalytic application, the wide band-gap (3. 2 *eV*) restricts its application in visible-light region. Recently photocatalytic studies of 1-dimensional TiO$_2$-nanotube arrays prepared by anodisation method have attracted more interest because of its unique physical and chemical properties. TiO$_2$ nanotube arrays can be converted into BaTiO$_3$ and SrTiO$_3$ nanotube arrays by simple methods such as

hydrothermal technique. Construction of heterogeneous nanostructures with suitable semiconductors is one of the most studied and applicable strategy to improve life span of active species that enhances the photocatalytic activity of the material. Doping is a widely used technique to bring down the band-gap of the material. Band-gap modification of TiO_2 nanotube arrays can be done by these methods. Redox chemistry has an important role to design a heterogeneous nanostructure, since the reduced or oxidized state can introduce a new energy level within the band-gap of the material. A number of studies have been reported regarding the modification of TiO_2 nanotube arrays for photocatalytic application, but the influence of surface morphology of TiO_2 heterostructures on the photocatalytic activity and the effect of redox chemistry involved during their fabrication have not yet been studied in detail. Previous research works have thrown light on the applicability of ferroelectric materials like $BaTiO_3$ for photocatalytic applications. The inherent ferroelectricity, appropriate band-gap and non-toxicity of $BaTiO_3$ make it a better candidate for photocatalytic applications. Band-gap tuning of ferroelectric materials extends its application range from UV to visible light region. Detailed studies about the modification of band-gap of $BaTiO_3$, especially in 1-dimensional nanotubular structures for photocatalytic applications have not yet been reported. In this context our present research work is mainly focused on the following areas.

➢ construction of heterogeneous nanostructures of TiO_2 nanotube arrays with suitable materials and study the effect of surface

morphology of such modified TiO_2 nanotube arrays on their photocatalytic activity

➢ preparation of $BaTiO_3$ nanotube arrays using TiO_2 nanotubes as precursor materials and tuning of the band-gap of the ferroelectric materials to extend its application to visible light region, which is not yet reported.

➢ The redox potential of the reactions involved during the fabrication of heterogeneous nanostructure has an important role to decide the properties of the heterostructure. Hence in this research work we have constructed heterogeneous nanostructure of $BaTiO_3$ nanotube arrays with SnO_2, by considering the redox chemistry of the reactions involved and studied the photocatalytic properties of the heterostructure, which is not yet reported.

➢ the study of the change in the band-structure of TiO_2 and $BaTiO_3$ resulting from formation of heterogeneous nanostructure and doping.

➢ correlation of the defect chemistry of $BaTiO_3$ nanotube arrays with their ferromagnetic ordering to further confirm the influence of defects in their photocatalytic activity

References.

[1]   R. Saravanan, F. Gracia, A. Stephan,Basic principles, Mechanism and challenges of photocatalysis, in :A. M. M. M. Khan, D. Pradhan, Y. Sohn (Eds.), Nanocomposites for Visible light induced Photocatalysis, (2017) Springer international publishing.

[2]   L. Liu , H. L Johnson, S. Cousens , J Perin, S. Scott, J. E Lawn, I. Rudan, H Campbell, R Cibulskis , M. Li, C. Mathers, R. E. Black , Global, regional, and national causes of child mortality: an updated systematic analysis for 2010 with time trends since 2000. The Lancet 379 (2012)2151–2161

[3]   V. K. Gupta , I. Ali , T. A. Saleh , A. Nayak, S. Agarwal, Chemical treatment technologies for waste-water recycling—an overview, RSC Adv. 2 (2012) 6380

[4]   M.N. Chong , B. Jin, C. W. K. Chow , C. Saint, Recent developments in photocatalytic water treatment technology: a review, Water. Res. 44(2010) 2997–3027.

[5]   K. Rajeshwar, M. E. Osugi, W. Chanmanee , C. R. Chenthamarakshan , M. Zanoni , P. Kajitvichyanukul, R. Krishnan-Ayer, Heterogeneous photocatalytic treatment of organic dyes in air and aqueous media, J. Photochem. Photobiol. C 9 (2008)171–192.

[6]   R. Andreozzi , V. Caprio, A. Insola, R. Marotta, Advanced oxidation processes (AOP) for water purification and recovery, Catal. Today 53 (1999) 51-59.

[7]   R. Munter, Advanced oxidation processes-current status and prospects, Proc. Estonian. Acad. Sci. Chem. 50 (2001) 59–80.

[8]   Y. Deng, R. Zhao, Advanced Oxidation Processes (AOPs) in Wastewater Treatment, Curr. Pollution. Rep, 1 (2015)167–176.

[9]   A. S. Stasinakis, Use of selected Advanced Oxidation Processes (AOPs) for wastewater treatment – A mini review, Global nest journal, 10 (2008) 376-385.

[10] N Serponea, Y. M. Artemev, V. K. Ryabchuk, A. V. Emeline, S. Horikoshi, (2017), Light-driven advanced oxidation processes in the disposal of emerging pharmaceutical contaminants in aqueous media: A brief review, Current Opinion in Green and Sustainable Chemistry, 6 (2017)18–33.

[11] D. I. Kondarides, Photocatalysis, in Catalysis, Ed. Gabriele Centi, in Encyclopedia of Life Support Systems (EOLSS), Developed under the Auspices of the UNESCO, EOLSS Publishers (2010) Oxford, UK

[12] A. Mill, S. Le Hunte, An overview of semiconductor photocatalysis, J. Photochem. Photobiol. A 108 (1997) 1-35.

[13] J. M. Hermman, C. Guillard, P. Pichat, Heterogeneous photocatalysis: an emerging technology for water treatment, Catal. Today, 17 (1993) 7-20.

[14] A. Fujishima, K. Honda, Electrochemical Photolysis of Water at a Semiconductor Electrode, Nature, 238 (1972) 37-38.

[15] F. T. Wagner, G. A. Somorjai, Photocatalytic and photoelectrochemical hydrogen production on strontium titanate single crystals, J. Am. Chem. Soc. 102 (1980) 5494–5502.

[16] T. Sakata , T. Kawai, Heterogeneous photocatalytic production of hydrogen and methane from ethanol and water, Chem. Phys. Lett. 80 (1981), 341–344.

[17] J. M. Coronado, A Historical Introduction to Photocatalysis. In: J. Coronado, F. Fresno, M. Hernández-Alonso, R. Portela (eds) Design of Advanced Photocatalytic Materials for Energy and Environmental Applications. Green Energy and Technology. Springer (2013) London.

[18] M. M. Khan, S. F. Adil, A. Al-Mayouf, Metal Oxides as Photocatalyst, J. Soudi. Chem. Soc. 19 (2015) 462-464.

[19] W. Wang, M. O. Tade, Z. Shao, Research progress of perovskite materials in photocatalysis and photovoltaics-related

energy conversion and environmental treatment, Chem. Soc. Rev. 44 (2015) 5371-5408.

[20] R. X. Wang, Q. Zhu, W. S. Wang, C. M. Fan, A. W. Xu, (2015) $BaTiO_3$–graphene nanocomposites: synthesis and visible light photocatalytic activity, New. J. Chem. 39 (2015) 4407-4413.

[21] K. M. Rezal, A. S. W. Kurny, F. Gulshan, Parameters affecting the photocatalytic degradation of dyes using TiO_2: a review, Appl. Water. Sci. 7 (2017) 1569-1578.

[22] R. Viswanatha, S. Sapra, B. Satpati, P. V. Sathym, B. N. Dev, D. D. Sharma, Understanding the quantam size effects in ZnO nanocrystals, J. Mater. Chem. 14 (2004) 661-668.

[23] J. Piella, N. G. Bastús, E. Casals, V. Puntes, Characterizing Nanoparticles Reactivity: Structure Photocatalytic Activity Relationship, J. Phys. Conf. Ser. 429 (2013) 012040 (1-7).

[24] D. Beydoun, R. Amal, G. Low, S. McEvoy, Role of Nanoparticles in Photocatalysis, J. Nanopart. Res. 1 (1999) 439-458.

[25] M. A. Majeed Khan, W. Khan, M. Ahamed, A. N. Alhazaa, Microstructural   properties   and   enhanced   photocatalytic performance of Zn doped CeO_2 nanocrystals, Sci. Rep. 7 (2017) 12560(1-11).

[26] K. N. Abbas, N. Biddin, Morphological Driven Photocatalytic Activity of ZnO Nanostructures, Appl. Surf. Sci. 394 (2017) 498-508.

[27] S. B. Khan, M. Hou, S. Shuang, Z. Zhang, Morphological Influence of TiO_2 Nanostructures (nanozigzag, nanohelics and nanorod) on Photocatalytic Degradation of organic dyes, Appl. Surf. Sci. 400 (2017) 184-193

[28] C. Adan, J. Marugan, E. Sanchez, C. Pablos, R. van Grieken, Understanding the effect of morphology on the photocatalytic activity of TiO_2 nanotube array electrodes, Electrochim. Acta. 191 (2016) 521-529.

[29]   A. Gnanaprakasam, V.M. Sivakumar, M. Thirumarimurugan, Influencing Parameters in the Photocatalytic Degradation of Organic Effluent via Nano metal Oxide Catalyst: A Review, Indian. J. Mater. Sci. 2015 (2015) Article ID 601827, 16 pages.

[30]   K. Bubacz, J. Choina, D. Dolat, A. W. Morawski, Methylene blue and phenol photocatalytic degradation on nanoparticles of anatase TiO_2, Pol. J. Environ. Stud. 19 (2010) 685–691.

[31]   C. M. Ling, A. R. Mohamed, S. Bhatia, Performance of photocatalytic reactors using immobilized TiO_2 film for the degradation of phenol and methylene blue dye present in water stream, Chemosphere, 57 (2004)547–554.

[32]   A. G. S. Prado, L. L. Costa, Photocatalytic decouloration of malachite green dye by application of TiO_2 nanotubes, J. Hazard. Mater. 169 (2009) 297–301.

[33]   A. Zaleska, Doped-TiO_2: a review, Recent Patents on Engineering, 2 (2008)   157–164.

[34]   J. W. Shi, J. T. Zheng, P. Wu, Preparation, characterization and photocatalytic activities of holmium-doped titanium dioxide nanoparticles, J. Hazard. Mater. 161 (2009)416–422.

[35]   M. Kang, S.J. Choung, J. Y. Park, Photocatalytic performance of nanometer-sized Fe_xO_y/TiO_2 particle synthesized by hydrothermal method, Catal. Today, 87 (2003) 87–97.

[36]   J. Yu, H. Yu, B. Cheng, M. Zhou, X. Zhao, Enhanced photocatalytic activity of TiO_2 powder (P25) by hydrothermal treatment, J. Mol. Catal A: Chem. 253 (2006) 112–118.

[37]   P. Sathishkumar, R. V. Mangalaraja, S. Anandan, M. Ashokkumar, $CoFe_2O_4/TiO_2$ nanocatalysts for the photocatalytic degradation of Reactive Red 120 in aqueous solutions in the presence and absence of electron acceptors, Chem. Eng. J. 220 (2013) 302–310.

[38]   Q. Xiang, J. Yu, M. Jaroniec, Graphene-based semiconductor photocatalysts, Chem. Soc. Rev. 41 (2012)782–796.

[39]   H. Wang, L. Zhang, Z. Chen, J. Hu, S. Li, Z. Wang, J. Liu, X. Wang, Semiconductor heterojunction photocatalysts: design, construction, and photocatalytic performances, Chem. Soc. Rev. 43 (2014) 5234-5244.

[40]   M. Alshehri, F. Al. Marzouki, A. Alshehrie, M. Hafez, J. Alloys. Compd. 757 (2018) 161-168.

[41]   L. Jiang, G. Zhou, J. Mi, Z. Wu, Fabrication of visible-light-driven one-dimensional anatase TiO_2/Ag heterojunction plasmonic photocatalyst, Catal. Commun. 24 (2012) 48–51.

[42]   M. Shang, W. Wang, L. Zhang, S. Sun, L. Wang, L. Zhou, 3D Bi_2WO_6/TiO_2 Hierarchical Heterostructure: Controllable Synthesis and Enhanced Visible Photocatalytic Degradation Performances, J. Phys. Chem. C, 113 (2009) 14727–14731.

[43]   T. Kawahara, Y. Konishi, H. Tada, N. Tohge, J. Nishii, S. Ito, A Patterned TiO_2 (Anatase)/TiO_2(Rutile) Bilayer Type Photocatalyst: Effect of the Anatase/Rutile Junction on the Photocatalytic Activity, Angew. Chem. Int. Ed.114 (2002) 2935–2937.

[44]   H. Li, Z. Bian, J. Zhu, Y. Huo, Y. Lu, Mesoporous Au/TiO_2 Nanocomposites with Enhanced Photocatalytic Activity, J. Am. Chem. Soc. 129 (2007) 4538–4539.

[45]   P. Wang, B. Huang, X. Qin, X. Zhang, Y. Dai, J. Wei, M. H. Whangbo, Ag@AgCl: A Highly Efficient and Stable Photocatalyst Active under Visible Light, Angew. Chem., Int. Ed. 47 (2008) 7931–7933.

[46]   J. Du, X. Lai, N. Yang, J. Zhai, D. Kisailus, F. Su, D. Wang, L. Jiang, Hierarchically Ordered Macro−Mesoporous TiO_2−Graphene Composite Films: Improved Mass Transfer, Reduced Charge Recombination, and Their Enhanced Photocatalytic Activities, ACS Nano, 5 (2010) 590–596.

[47]   Q. Li, B. Guo, J. Yu, J. Ran, B. Zhang, H. Yan, J. R. Gong, Highly Efficient Visible-Light-Driven Photocatalytic Hydrogen Production of CdS-Cluster-Decorated Graphene Nanosheets, J. Am. Chem. Soc. 133 (2011) 10878–10884.

[48]   E. Gao, W. Wang, M. Shang , J. Xu, Synthesis and enhanced photocatalytic performance of graphene-Bi_2WO_6 composite, Phys. Chem. Chem. Phys. 13 (2011) 2887–2893.

[49]   M. R. Hoffmann, S. T. Martin, W. Choi, D. W. Bahnemann, Environmental Applications of Semiconductor Photocatalysis, Chem. Rev. 95 (1995) 69–96.

[50]   J. F. Tanguay, S. L. Suib, R. W. Coughlin, Dichloromethane photodegradation using titanium catalysts, J. Catal. 117 (1989) 335–347.

[51]   X. Huang, X. Qi, F. Boey, H. Zhang, Graphene-based composites, Chem. Soc. Rev. 41 (2012) 666–686.

[52]   L. S. Zhang, K. H. Wong, Z. G. Chen, J. C. Yu, J. C. Zhao, C. Hu, C. Y. Chan, P. K. Wong, AgBr-Ag-Bi_2WO_6 nanojunction system: A novel and efficient photocatalyst with double visible-light active components, Appl. Catal. A, 363 (2009)221–229.

[53]   I. Paramasivam, H. Jha, N. Liu, P. Schmuki, A review of photocatalysis using self-organized TiO_2 nanotubes and other ordered oxide nanostructures, Small, 8 (2012) 3073-3103.

[54]   J. Wang, D. Nyago Tafen, J. P. Lewis, Z. Hong, A. Manivannan, M. Zhi, M. Li, N. Wu, Origin of Photocatalytic Activity of Nitrogen-Doped TiO_2 Nanobelts, J. Am. Chem. Soc. 131 (2009) 12290–12297.

[55]   Y. Lu , Y. Lin , D. Wang, L. Wang, T. Xie, T. Jiang, A high performance cobalt-doped ZnO visible light photocatalyst and its photogenerated charge transfer properties, Nano. Res. 4 (2011) 1144-1152.

[56]   R. Saleh, N. F. Djaja, UV light photocatalytic degradation of organic dyes with Fe-doped ZnO nanoparticles, Superlatt. Microstruct.74 (2014) 217–233.

[57]   R. Mohan, K. Krishnamoorthy, S. J. Kim, Enhanced photocatalytic activity of Cu-doped ZnO nanorods Solid State. Commun. 152 (2012) 375.

[58] S. C. Das, R. J. Green, J. Podder, T. Z. Regier, G. S. Chang, A. Moewes , Band gap tuning in ZnO through Ni doping via spray pyrolysis, J. Phys. Chem. C, 117 (2013)12745–12753.

[59] S. Z. Karazhanov, Z. Yong, L. W. Wang, A. Mascarenhas, S. Deb, Resonant defect states and strong lattice relaxation of oxygen vacancies in WO_3, Phys. Rev. B, 68 (2003) 233204.

[60] S. G. Ullatil, P. Periyatt, Green microwave switching from oxygen rich yellow anatase to oxygen vacancy rich black anatase TiO_2 solar photocatalyst using Mn(II) as'anatase phase purifier, Nanoscale, 7 (2015) 19184-19192.

[61] A. Naldoni, M. Allieta, S. Santangelo, M. Marelli, F. Fabbri, S. Cappelli, C. L. Bianchi, R. Psaro, V. D. Santo, Effect of Nature and Location of Defects on Band gap Narrowing in Black TiO_2 Nanoparticles, J. Am. Chem. Soc. 134 (2012) 7600–7603.

[62] A. Janoti, C. G. Van de Walle, Fundamentals of zinc oxide as a semiconductor, Rep. Prog. Phys. 72 (2009) 126501 (1-29).

[63] M. A. Ruderman, C. Kittel, Indirect Exchange Coupling of Nuclear Magnetic Moments by Conduction Electrons, Phys. Rev. 96 (1954) 99-102.

[64] C. Zener, Interactions between the d-shells in transition metals, Phys. Rev. 81 (1951) 440.

[65] H. A. Cramers, The interaction between Magnetogenic Atoms in a Paramagnetic Crystal, Physica, 1 (1934) 182-192.

[66] C. Zener, Interaction between the d-shells in the Transition Metals. II. Ferromagnetic compounds of Mangnese with Perovskite structure, Phys. Rev. 82 (1951) 403.

[67] J. M. D. Coey, M. Venkatesan, C. B. Fitzgerald, Donor impurity band exchange in dilute ferromagnetic oxides, Nat. Mater. 4 (2005) 173-179.

[68] G. C. Ibanez, C. B. Coldeira, M. F. Garcia, Nano structured oxides in photocatalysis-in Synthesis, Properties and application of Oxide Nanomaterials, in J. A. Rodriguez, M. F. Garcia (Eds) (2007), willy publication, New-Jersey.

[69]   J. Schneider, M. Matsuoka, M. Takeuchi, J. Zhang, Y. Horiuchi, M. Anpo, D. W. Bahnemann, Understanding TiO_2 Photocatalysis: Mechanisms and Materials, Chem. Rev. 114 (2014) 9919-9986.

[70]   Q. Tay, X. Liu, Y. Tang, Z. Jiang, T. C. Sum, Z. Chen, Enhanced Photocatalytic Hydrogen Production with Synergistic Two-Phase Anatase/Brookite TiO_2 Nanostructures, J. Phys. Chem. C, 117 (2013) 14973-14982.

[71]   J. Zhang, P. Zhou, J. Liu, J. Yu , New understanding of the difference of photocatalytic activity among anatase, rutile and brookite TiO_2, Phys. Chem. Chem. Phys. 14 (2014) 20382-20386.

[72]   A. Beltran, L. Gracia and J. Andres, Density Functional Theory Study of the Brookite Surfaces and Phase Transitions between Natural Titania Polymorphs, J. Phys. Chem. B, 110 (2006) 23417-23423.

[73]   D. T. Cromer, K. Herrington, The Structures of Anatase and Rutile J. Am. Chem. Soc. 77 (1955) 4708-4709.

[74]   S. D. Mo, W. Y. Ching, Electronic and optical properties of three phases of titanium dioxide: Rutile, anatase, and brookite, Phys. Rev. B, 51 (1995) 13023-13031.

[75]   R. Asahi, T. Morikawa, H. Irie, T. Ohwaki, Nitrogen-Doped Titanium Dioxide as Visible-Light-Sensitive Photocatalyst: Designs, Developments, and Prospects, Chem. Rev. 114 (2014) 9824-9852.

[76]   R. Asahi, Y. Taga, W. Mannstadt, A. J. Freeman, Electronic and optical properties of anatase TiO_2, J. Phys. Rev. B, 61 (2000) 7459-7465.

[77]   Y. Cong, F. Chen, J. L. Zhang, M. Anpo, Carbon and Nitrogen-codoped TiO_2 with High Visible Light Photocatalytic Activity, Chem. Lett., 35, (2006) 800-801

[78]   D. A. H. Hanaor, C. C. Sorrell, Review of the anatase to rutile phase transformation, J. Mater. Sci. 46 (2011) 855–874.

[79]   A. Y. Ahmed, T. A. Kandiel, T. Oekermann, D. Bahnemann, Photocatalytic Activities of Different Well-defined Single Crystal TiO_2 Surfaces: Anatase versus Rutile, J. Phys. Chem. Lett. 2 (2011) 2461-2465.

[80]   A. Sclafani, J. M. Herrmann, Comparison of the Photoelectronic and Photocatalytic Activities of Various Anatase and Rutile Forms of Titania in Pure Liquid Organic Phases and in Aqueous Solutions, J. Phys. Chem.100 (1996) 13655-13661.

[81]   Q. Zhang, L. Gao, J. Guo, Effects of calcination on the photocatalytic properties of nanosized TiO_2 powders prepared by $TiCl_4$ hydrolysis, Appl. Catal., B, 26 (2000) 207-215.

[82]   J. Zhang, P. Zhou, J. Liu, J. Yu, New understanding of the difference of photocatalytic activity among anatase, rutile and brookite TiO_2, Phys. Chem. Chem. Phys. 14 (2014) 20382-20386.

[83]   J. J. M. Vequizo, H. Matsunaga, T. Ishiku, S. Kamimura, T. Ohno, A. Yamakata, Trapping-Induced Enhancement of Photocatalytic Activity on Brookite TiO_2 Powders: Comparison with Anatase and Rutile TiO_2 Powders ACS Catal. 7 (2017) 2644-2651.

[84]   J. Wang, N. N. Wu, One dimensional titanate and titania nano structures synthesized by hydrothermal process. In X. J. Huang (Eds), Nanotechnology Research: New Nanostructures, Nanotubes and Nanofibers, (2008) Nova publishers.

[85]   M. Ge, C. Cao, J. Huang, S. Li, Z. Chen, K.Q. Zhang, S. S. Al-Deyabd, Y. Lai, A review of one-dimensional TiO_2 nanostructured materials for environmental and energy applications, J. Mater. Chem. A, 4 (2016) 6772-6801.

[86]   H. B. Wu, H. H. Hng , X. W. (David) Lou, Direct Synthesis of Anatase TiO_2 Nanowires with Enhanced Photocatalytic Activity, Adv. Mater. 24 (2012) 2567-2571.

[87]   Q. Xiang, K. Lv, J. Yu, Pivotal role of fluorine in enhanced photocatalytic activity of anatase TiO_2 nanosheets with

dominant (0 0 1) facets for the photocatalytic degradation of acetone in air, Appl. Catal. B, 96 (2010) 557-564.

[88]   J. Pan, X. Wu, L. Wang, G. Liu, G. Q. (Max) Lub, H. M. Chenga, Synthesis of anatase TiO_2 rods with dominant reactive {010} facets for the photoreduction of CO_2 to CH_4 and use in dye-sensitized solar cells, Chem. Commun. 47 (2011) 8361–8363.

[89]   S. Chuangchote, J. Jitputti, T. Sagawa, S. Yoshikawa, Photocatalytic Activity for Hydrogen Evolution of Electrospun TiO_2 Nanofibers, ACS Appl. Mater. Interfaces, 1, (2009) 1140–1143.

[90]   N. Wu, J. Wang, D. N. Tafen, H. Wang, J. G. Zheng, J. P. Lewis, X. Liu, S. S. Leonard, A. Manivannan, Shape-Enhanced Photocatalytic Activity of Single-Crystalline Anatase TiO_2 (101) Nanobelts, J. Am. Chem. Soc. 132 (2010) 6679-6685.

[91]   T. Kasuga, M. Hiramatsu, A. Hoson, T. Sekino, K. Niihara, Titania Nanotubes Prepared by Chemical Processing, Adv. Mater. 11 (1999) 1307-1311.

[92]   J. Yu, G. Dai, B. Cheng, Effect of Crystallization Methods on Morphology and Photocatalytic Activity of Anodized TiO_2 Nanotube Array Films, J. Phys. Chem. C, 114 (2010) 19378–19385.

[93]   V. Zwilling, E. Darque-Ceretti, A. Boutry-Forveille, D. David, M. Y. Perrin, M. Aucouturier, Structure and physicochemistry of anodic oxide films on titanium and TA6V alloy, Surf. Interface Anal. 27 (1999) 629-637.

[94]   M. Paulose, K. Shankar, S. Yoriya, H. E. Prakasam, O. K. Varghese, G. K. Mor, T. A. Latempa, A. Fitzgerald, C. A. Grimes, Anodic Growth of Highly Ordered TiO_2 Nanotube Arrays to 134 μm in Length, J. Phys. Chem. B, 110 (2006) 16179–16184.

[95]   L. Salou, A. Hoornaert, G. Louarn, P. Layrolle, Bone Apposition on Nanoporous Titanium implants, in A. S. H. Makhlouf, D. Scharnweber (eds) Handbook of Nanoceramic

and Nanocomposite Coatings and Materials, (2015) Elsevier publications.

[96]   S. Sreekantan, Z. Lockman, R. Hazan, M. Tasbihi, L. K. Tong, A. R. Mohamed, Influence of electrolyte pH on TiO_2 nanotube formation by Ti anodisation, J. Alloys. Compd. 485 (2009) 478-483.

[97]   S. Sreekantan, K. A. Saharudin, Z. Lockman, T. Wah Tzu, Fast-rate formation of TiO_2 nanotube arrays in an organic bath and their applications in photocatalysis, Nanotechnology, 21 (2010) 365603.

[98]   P. Roy, S. Berger, P. Schmuki, TiO_2 Nanotubes: Synthesis and Applications, Angew. Chem. Int. Ed. 50 (2011) 2904 – 2939.

[99]   R. Beranek, H. Hildebrand, P. Schmuki, Self-Organized Porous Titanium Oxide Prepared in H_2SO_4/HF Electrolytes, Electrochem. Solid State Lett. 6 (2003) 6, B12.

[100]   K. Indira, U. Kamachi Mudali, T. Nishimura, N. Rajendran, A Review on TiO_2 Nanotubes: Influence of Anodization Parameters, Formation Mechanism, Properties, Corrosion Behavior, and Biomedical Applications, J. Bio. Tribo. Corros. (2015) 28 (22 pages)

[101]   J. M. Macak, H. Tsuchiya, L. Taveira, S. Aldabergerova, P. Schmuki, Smooth anodic TiO_2 nanotubes. Angew. Chem. Int. Ed. 44 (2005) 7463–7465.

[102]   K. Indira, S. Ningshen, U. Kamachi Mudali, N. Rajendran, Effect of electrolyte temperature on the surface morphology of anodized Ti. In: S. Jayakumar, M. D. Kannan, R. Balasundaraprabhu, S. Prassana (eds) Thin film and nanomaterials, advanced research series. Macmillan, India (2011) pp 63–66.

[103]   H. Tsuchiya, J. M. Macak, A. Ghicov , Characterization of electronic properties of TiO_2 nanotube films, Corros. Sci. 49 (2007)203–210.

[104] Y. Li, Q. Ma, J. Han, L. Ji, J. Wang, J. Chen, Y. Wang, Controlled preparation, growth mechanism and properties research of TiO$_2$ nanotube arrays, Appl. Surf. Sci. 297 (2014) 103–108.

[105] S. Sreekantan, K. A. Saharudin, L. C. Wei, Formation of TiO$_2$ nanotubes via anodization and potential applications for photocatalysts, biomedical materials, and photoelectrochemical cell. IOP Conf. Series: Mater. Sci. Eng. 21 (2011) 012002. doi:10.1088/1757-899X/21/1/012002

[106] N. K. Allam, C. A. Grimes, Effect of cathode material on the morphology and photoelectrochemical properties of vertically oriented TiO$_2$ nanotube arrays, Solar Energy Mater. Solar Cells, 92 (2008)1468–1475.

[107]   S. Yoriya, Effect of inter-electrode spacing on electrolyte properties and morphologies of anodic TiO$_2$ nanotube array films, Int. J. Electrochem. Sci. 7 (2012) 9454-9464.

[108] S. Chen, M. Paulose, C. Ruan, G. K. Mor, O. K. Varghese, D. Kouzoudis, C. A. Grimes, Electrochemically synthesized CdS nanoparticle-modified TiO$_2$ nanotube-array photoelectrodes: Preparation, characterization and application to photoelectrochemical cells, J. Photochem. Photobiol. 177 (2006) 177-184.

[109] X. F. Gao, W. T. Sun, Z. D. Hu, G. Ai, Y. L. Zhang, S. Feng, F. Li, L. M. Peng, An Efficient Method To Form Heterojunction CdS/TiO$_2$ Photoelectrodes Using Highly Ordered TiO$_2$ Nanotube Array Films, J. Phys. Chem. C, 113 (2009) 20481–20485.

[110] W. T. Sun, Y. Yu, H. Y. Pan, X. F. Gao, Q. Chen, L. M. Peng, CdS Quantum Dots Sensitized TiO$_2$ Nanotube-Array Photoelectrodes, J. Am. Chem. Soc. 130 (2008) 1124-1125.

[111] X. Zhou, F. Yang, B. Jin, L. Chen, S. Li, Fabrication of CdS/H-TiO$_2$ Nanotube Arrays and Their Application for the Degradation of Methyl Orange in Aqueous Solutions, J. Nanomater, Volume 2014 (2014), Article ID 678505, 7 pages

[112]   Q. Kang, S. Liu, L. Yang, Q. Cai, C.A. Grimes, Fabrication of PbS Nanoparticle-Sensitized TiO_2 Nanotube Arrays and Their Photoelectrochemical Properties Appl. Mater. Interfaces, 3 (2011) 746–749.

[113]   N.B. Rahna, V. Kalarivalappil, M. Nageri, S. C. Pillai, S. J. Hinder, V. Kumar, B. K. Vijayan, Stability studies of PbS sensitized TiO_2 nanotube arrays for visible light photocatalytic applications by X-ray photoelectron spectroscopy (XPS), Mater. Sci. Semicond. Process. 42 (2016) 303-310.

[114]   L. Yang, S. Luo, R. Liu, Q. Cai, Y. Xiao, S. Liu, F. Su, L. Wen, Fabrication of CdSe Nanoparticles Sensitized Long TiO_2 Nanotube Arrays for Photocatalytic Degradation of Anthracene-9-carbonxylic Acid under Green Monochromatic Light, J. Phys. Chem. C, 114 (2010) 4783–4789.

[115]   P. Xue, Y. Yin, Y. Wang, J. Wan, Y. Ma, E. Liu, X. Hu, J. Fan, In situ fabrication of CdSe/TiO_2 nanotube arrays with enhanced photoelectrical and catalytic activity, Semicond. Sci. Technol. volume 32 (2017) number 11.

[116]   A. I. Kontos, V. Likodimos, T. Stergiopoulos, D. S. Tsoukleris, P. Falaras, I. Rabias, G. Papavassiliou, D. Kim, J. Kunze, P. Schmuki, Self-Organized Anodic TiO_2 Nanotube Arrays Functionalized by Iron Oxide Nanoparticles, Chem. Mater. 21 (2009) 662–672.

[117]   Y. Shen, F. Li, D. Liu, S. Li, L. Fan, Fabrication of TiO_2 Nanotube Films Modified with Ag_2S and Photoelectrocatalytic Decolorization of Methyl Orange Under Solar Light, Sci. Adv. Mater. 4 (2012) 1214–1219.

[118]   N. K. Shrestha, M. Yang, Y. C. Nah, I. Paramasivam, P. Schmuki, Self-organized TiO_2 nanotubes: Visible light activation by Ni oxide nanoparticle decoration, Electrochem. Commun. 12 (2010) 254-257.

[119]   P. Roy, D. Kim, I. Paramasivam, P. Schmuki, Improved efficiency of TiO_2 nanotubes in dye sensitized solar cells by decoration with TiO_2 nanoparticles, Electrochem. Commun. 11 (2009) 1001-1004.

[120]   S. Benkara, S. Zerkout, Preparation and characterization of ZnO nanorods grown into aligned TiO$_2$ nanotube array, J. Mater. Environ. Sci. 3 (2010) 173–188.

[121]   Y. Lei, G. Zhao, M. Liu, Z. Zhang, X. Tong, T. Cao, Fabrication, Characterization, and Photoelectrocatalytic Application of ZnO Nanorods Grafted on Vertically Aligned TiO$_2$ Nanotubes, J. Phys. Chem. C, 113 (2009)19067–19076.

[122]   Z. Zhang, Y. Yuan, L. Liang, Y. Cheng, G. Shi, L. Jin, Preparation and photoelectrocatalytic activity of ZnO nanorods embedded in highly ordered TiO$_2$ nanotube arrays electrode for azo dye degradation, J. Hazard. Mater. 158 (2008) 517–522.

[123]   F.X. Xiao (2012), Construction of Highly Ordered ZnO–TiO$_2$ Nanotube Arrays (ZnO/TNTs) Heterostructure for Photocatalytic Application, Appl. Mater. Interfaces, 4 (2012) 7055–7063.

[124]   P. Song, X. Zhang, M. Sun, X. Cui, Y. Lin, Graphene oxide modified TiO$_2$ nanotube arrays: enhanced visible light photoelectrochemical properties, Nanoscale, 4 (2012) 1800-1804.

[125]   H. Sun, P. Zhao, F. Zhang, Y. Liu, J. Hao, Ag$_2$S/CdS/TiO$_2$ Nanotube Array Films with High Photocurrent Density by Spotting Sample Method, Nanoscale. Res. Lett. 10 (2015) 382.

[126]   A. Ghicov, J. M. Macak, H. Tsuchiya, J. Kunze,V. Haeublein, L. Frey, P. Schmuki, Ion Implantation and Annealing for an Efficient N-Doping of TiO$_2$ Nanotubes, Nano. Lett. 6 (2006) 1080-1082.

[127]   Y. K. Lai, J. Y. Huang, H. F. Zhang, V. P. Subramaniam, Y. X. Tang, D. G. Gong, L. Sundar, L. Sun, Z. Chen, C. J. Lina, Nitrogen-doped TiO$_2$ nanotube array films with enhanced photocatalytic activity under various light sources, J. Hazard. Mater. 184 (2010) 855-863.

[128]   S. Li, S. Lin, J. Liao, N. Pan, D Li, J. Li, Nitrogen-Doped TiO$_2$ Nanotube Arrays with Enhanced Photoelectrochemical

Property, Int. J. Photonenergy, volume 2012 (2012) Article ID 794207, 7 pages.

[129]   A. B. Aritonang, H. Surahman, Y. K. Krisnandi, J. Gunlazuardi, Photo-electro-catalytic performance of highly ordered nitrogen doped TiO_2 nanotubes array photoanode, IOP Conf. Ser.: Mater. Sci. Eng. 172 (2017) 012005.

[130]   L. Sun, J. Cai, Q. Wu, P. Huang, Y. Su, C. Lin, N-doped TiO_2 nanotube array photoelectrode for visible-light-induced photoelectrochemical and photoelectrocatalytic activities, Electrochim. Acta 108 (2013) 525– 531.

[131]   H. Wang, H. Li, J. Wang, J. Wu, D. Li, M. Liu, P. Su, Nitrogen-doped TiO_2 nanoparticles better TiO_2 nanotube array photo-anodes for dye sensitized solar cells, Electrochim. Acta 10 (2014) 744-750.

[132]   Y Su, S. Chen, X. Quan, H. Zhao, Y. Zhang, A silicon-doped TiO_2 nanotube arrays electrode with enhanced photoelectrocatalytic activity, Appl. Surf. Sci. 255 (2008) 2167–2172.

[133]   N. Lu, X. Quan, J. Y. Li, S. Chen, H. T. Yu, G. H. Chen, Fabrication of Boron-Doped TiO_2 Nanotube Array Electrode and Investigation of Its Photoelectrochemical Capability, J. Phys. Chem. C, 111 (2007) 11836-11842.

[134]   M. Szkoda, K. Siuzdak, A. L. Oleksiak, J. Karczewski, J. Ryl, Facile preparation of extremely photoactive boron-doped TiO_2 nanotubes arrays, Electrochem. Commun. 60 (2015) 212-215

[135]   J. H. Park, S. Kim, A. J. Bard, Novel Carbon-Doped TiO_2 Nanotube Arrays with High Aspect Ratios for Efficient Solar Water Splitting, Nano. Lett. 6 (2006) 24-28.

[136]   L. Sun , J. Li , C. L. Wang, S. F. Li, H. B. Chen, C. J. Lin, An electrochemical strategy of doping Fe^{3+} into TiO_2 nanotube array films for enhancement in photocatalyticactivity, Sol. Energy Mater. Sol 93 (2009) 1875-1880.

[137]   Y. F. Tu, S. Y. Huang, J. P. Sang, X. W. Zou, Preparation of Fe-doped TiO_2 nanotube arrays and their photocatalytic activities under visible light, 45 (2010) 224-229.

[138]   A. Ghicov, B. Schmidt, J. Kunze, P. Schmuki, Photoresponse in the visible range from Cr doped TiO_2 nanotubes, Chem. Phys. Lett. 433 (2007) 323-326.

[139]   H. Liu, G. Liu, Q. Zhou, Preparation and characterization of Zr doped TiO_2 nanotube arrays on the titanium sheet and their enhanced photocatalytic activity, J. Solid State. Chem. 182 (2009) 3238-3242.

[140]   J. Zhao, X. Wang, Y. Kang, X. Xu, Y. Li, Photoelectrochemical Activities of W-Doped Titania Nanotube Arrays Fabricated by Anodization, IEEE Photonics Technol. Lett. 20 (2008) 1213-1215.

[141]   J. Hu, J. Cheng, S. Tong, Y. Yang, M. Chen, S. Hu, Ag-Doped TiO_2 Nanotube Arrays Composite Film as a Photoanode for Enhancing the Photoelectric Conversion Efficiency in DSSCs, Int. J. Photoenergy, Volume 2016 (2016) Article ID 2736257, 9 pages.

[142]   X. Wei, P. S. Nbelayim, G. Kawamura, H. Muto, A. Matsuda, Ag nanoparticle-filled TiO_2 nanotube arrays prepared by anodization and electrophoretic deposition for dye-sensitized solar cells, Nanotechnology, 28 (2017)135207 (8 pages).

[143]   Y. Wang , Z. Li , Y. Tian, W. Zhao, X. Liu, J. Yang, Facile method for fabricating silver-doped TiO_2 nanotube arrays with enhanced photoelectrochemical property, Mater. Lett. 122 (2014) 248-251.

[144]   M. Enachi, M. Guix, T. Braniste, V. Postolache, V. Ciobanu, V. Ursaki, O. G. Schmidt, I. Tiginyanu, Photocatalytic Properties of TiO_2 Nanotubes Doped with Ag, Au and Pt or Covered by Ag, Au and Pt Nanodots, Surf. Eng. Appl. Electrochem. 51 (2015) 3-8.

[145]   X. Zhou, B. Jin, S. Zhang, H. Wang, H. Yu, F. Peng, Preparation of boron and phosphor co-doped TiO_2 nanotube

arrays and their photoelectrochemical property, Electrochem. Commun. 19 (2012) 127-130.

[146]   X. Fana, J. Fan, X. Hu, E. Liu, L. Kang, C. Tang, Y. Ma, H. Wu, Y. Li , Preparation and characterization of Ag deposited and Fe doped TiO_2 nanotube arrays for photocatalytic hydrogen production by water splitting, Ceram. Int. 40 (2014) 15907-15917.

[147]   D. Lu, M. Zhang, Z. Zhang, Q. Li, X. Wang, J. Yang, Self-organized vanadium and nitrogen co-doped titania nanotube arrays with enhanced photocatalytic reduction of CO_2 into CH_4, Nanoscale Res. Lett. 9 (2014) 272.

[148]   Y. Mao, S. Banerjee, S. S. Wong, Hydrothermal synthesis of perovskite nanotubes Chem. Commun. 3 (2003) 408-409.

[149]   Y. Xin, J. Jiang, K. Huo, P. K. Chu, Bioactive $SrTiO_3$ Nanotube Arrays: Strontium Delivery Platform on Ti-Based Osteoporotic Bone Implants, ACS Nano 3 (2009)3228-3234.

[150]   P. Kanhere, Z. Chen, A Review on Visible Light Active Perovskite-Based Photocatalysts, Molecules, 19 (2014) 19995-20022.

[151]   G. Zhang, G. Liu, L. Wang, T. S. J. Irvine, Inorganic perovskite photocatalysts for solar energy utilization, Chem. Soc. Rev. 45 (2016)5951-5984.

[152]   R. Konta, T. Ishii, H. Kato, A. Kudo, Photocatalytic Activities of Noble Metal Ion Doped $SrTiO_3$ under Visible Light Irradiation, J. Phys. Chem. B 108 (2004)8992-8995

[153]   R. Asai, H. Nemoto, Q. Jia, K. Saito, A. Iwase, A. Kudo, A visible light responsive rhodium and antimony codoped $SrTiO_3$ powdered photocatalyst loaded with an IrO_2 cocatalyst for solar water splitting, Chem. Commun. 50 (2014)2543–2546.

[154]   K. Iwashina, A. Kudo, Rh-Doped $SrTiO_3$ Photocatalyst Electrode Showing Cathodic Photocurrent for Water Splitting under Visible-Light Irradiation, J. Am. Chem. Soc. 133 (2011)13272–13275.

[155]   H. J. Zhang, G. Chen, Y. X. Li, Y. J. Teng, Electronic structure and photocatalytic properties of copper-doped $CaTiO_3$, Int. J. Hydrogen Energy, 35 (2010)2713–2716.

[156]   Y. Cui, J. Briscoe, S. Dunn, Effect of Ferroelectricity on Solar-Light-Driven Photocatalytic Activity of $BaTiO_3$-Influence on the Carrier Separation and Stern Layer Formation, Chem. Mater. 25 (2013) 4215−4223.

[157]   Y. Inoue, K. Sato, K. Sato, and H. Miyama, Photoassisted water decomposition by ferroelectric lead zirconate titanate ceramics with anomalous photovoltaic effects J. Phys. Chem. 90 (1986)2809-2810.

[158]   V. M. Fridkin, Bulk photovoltaic effect in noncentrosymmetric crystals Crystallogr. Rep. 46, (2001) 654 -658.

[159]   K. Maeda, Rhodium-Doped Barium Titanate Perovskite as a Stable p-Type Semiconductor Photocatalyst for Hydrogen Evolution under Visible Light, ACS Appl. Mater. Interfaces 6 (2014) 2167–2173.

[160]   S. Upadhyay, J. Shrivastava, A. Solanki, S. Choudhary, V. Sharma, P. Kumar, N. Singh, V. R. Satsangi, R. Shrivastav, V. Umesh, U. V. Waghmare, S. Dass, Enhanced Photoelectrochemical Response of $BaTiO_3$ with Fe Doping: Experiments and First-Principles Analysis, J. Phys. Chem. C 115 (2011) 24373–24380.

[161]   A. Kolezynski , K. T. Smiech, From the Molecular Picture to the Band Structure of Cubic and Tetragonal Barium Titanate Ferroelectrics, 314 (2005) 123 — 134.

[162]   S. Saha, T. P. Sinha, A. Mookerjee, Electronic structure, chemical bonding, and optical properties of paraelectric $BaTiO_3$, Phys. Rev. B, 62, (2000)8828-8834.

[163]   M. Rasthogi, H. S. Kushwaha, R. Vaish, Highly Efficient Visible Light Mediated Azo Dye Degradation Through Barium Titanate Decorated Reduced Graphene Oxide Sheets, Electron. Mater. Lett. 12 (2016) 281-289.

[164]   R. Inoue, S. Ishikawa, Y. Kitanaka, T. Oguchi, Y. Noguchi, M. Miyayama, Photocurrent Characteristics of Mn-Doped Barium Titanate Ferroelectric Single Crystals, Jpn. J. Appl. Phys. 52 (2013) 09KF03 (1-6).

[165]   Z. Ping Zou, L. Zhu Zhang, S. Lian Luo, L. Hui Leng, X. Biao Luo, M. Jian Zhang, Y. Luo, G. Cong Guo, Preparation and photocatalytic activities of two new Zn-doped $SrTiO_3$ and $BaTiO_3$ photocatalysts for hydrogen production from water without cocatalysts loading, Int. J. Hydrogen Energy, 37 (2012) 17068-17077.

[166]   Z. Shen, Y. Wang, W. Chen, H. Lai Wah Chan, L. Bing, Photocatalysis of Yttrium Doped $BaTiO_3$ Nanofibres Synthesized by Electrospinning, J. Nanomater. Volume 2015 (2015) Article ID 327130, 6 pages.

[167]   J. Liu, Y. Sun, Z. Li, Ag loaded flower-like $BaTiO_3$ nanotube arrays: Fabrication and enhanced photocatalytic property, Cryst. Eng. Comm. 14 (2012)1473-1478.

[168]   R. Li, Q. Li, L. Zong, X. Wang, J. Yang, $BaTiO_3/TiO_2$ heterostructure nanotube arrays for improved photoelectrochemical and photocatalytic applications, Electrochim. Acta. 91 (2013) 30-35.

CHAPTER 2
MATERIALS AND METHODS

CONTENTS

2.1 Introduction

In this chapter, a brief description of the experimental methods adopted for the fabrication and modification of titania nanotube arrays and the basic principle, working and experimental set up of instrumentation used for studying structural, optical, and photocatalytic properties of titania nanotube arrays based films are given.

2.2 Electrochemical potentiosatic anodisation process

Anodisation process is one of the simplest and advanced technique for production titania nanotubes [1]. The details of anodisation process are already we discussed in the introduction section. Electrochemical anodisation process involves the application of constant potential in between the anode and cathode, immersed in an electrolyte solution. The pictorial representation of anodisation process is given in the Figure 2.1
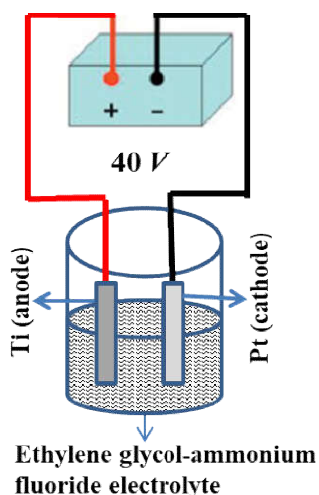
Fig. 2.1: Schematic representation of anodisation process adopted for fabrication of titania nanotube arrays (TNA).

We used Pt metal as cathode, Ti-metal foil as anode and ethylene-glycol ammonium fluoride solution as electrolyte, for potentiosatic electrochemical anodisation process. A constant potential of 40 V is applied in between the electrodes up to 24 hrs. Well-ordered TiO_2-nanotube arrays of 129 nm diameters, wall thickness 25 nm and length of 30 μm were fabricated through the above specified potentiosatic anodisation process. The important advantages of the anodisation process are i) simplicity ii) cost effective iii) easy to prepare nanotubes of desired length, diameter, and wall thickness. We can control the tubular parameter of nanotube arrays of TiO_2 nanotubes. The titania nanotubes thus synthesized is further modified for photocatalytic applications.

2.3 Hydrothermal synthesis

Hydrothermal synthesis can be defined as any heterogeneous chemical reaction in an aqueous media carried out above room temperature and at a pressure greater than 1 atm in a closed system [2]. The word hydrothermal synthesis was first used by British geologist Sir Roderick Murchison (1792-1871) to explain the action of water at elevated temperature and pressure which brings changes at the earth crust leading to the creation of various minerals and rocks [3]. Normally water is used as solvent for hydrothermal technique. Water is known to be a universal solvent, and have so many advantages. One of the biggest benefits of using water is the environmental friendly nature of the solvent and inexpensive than other solvents, and it can act as a catalyst for the development of desired materials by altering the temperature and the pressure. It is nonhazardous, nonflammable,

noncarcinogenic, nonmutagenic, and thermodynamically stable. Another advantage is that water easily volatile, so it can be removed from the product very simply.

2.3.1 Advantage of hydrothermal synthesis

Hydrothermal synthesis has many advantages compared to other conventional and nonconventional synthetic methods. The costs for the instrumentation, energy utilization during the process and amount of precursor needed are very less for hydrothermal process. A large variety of forms of desired products can be synthesized by hydrothermal methods. Other important merits of hydrothermal method of synthesis are given below.

1) Environmental friendly synthetic procedure.

2) Only low temperature is needed for this method, comparing with others, hence it helps to avoid problems related with high temperature.

3) Crystallinity can be achieved even at low temperature; the experimental conditions like high pressure at closed system may help to form crystalline materials at low temperature itself.

4) It is possible to control the rate of nucleation, growth and aging which effects size and morphology of the product formed.

5) Thus we can control the size, and morphology of the product formed during hydrothermal synthesis

6) This method can hybridized with other process like microwave, electrochemistry, optical radiation and hot pressing to give advantages such as enhancement of reaction kinetics, and to make new materials.

7) This easy method does not need any catalyst, harmful and expensive vessels and surfactants. Thus hydrothermal method is a advantages method for the production of high quality crystalline products in large amount having low cost.

2.3.2 Autoclave used in hydrothermal synthesis

Usually hydrothermal reactions are carried out in a teflon lined hydrothermal vessel which enclosed in closed vessel known to be as autoclave. Because of high pressure working conditions, sometimes the hydrothermal autoclave which is used for the hydrothermal synthesis are known as to be hydrothermal bomb. The different parts of an autoclave are given in the Figure 2. 2. In general hydrothermal reaction uses highly corrosive salts for synthetic applications. Hence the autoclave must have the capability to sustain high corrosive solvent at high temperature, high pressure at long duration of time.

Fig. 2.2: Parts of a typical autoclave used for hydrothermal process.

The other advantages of ideal autoclaves are that it can be easily assemble and dissemble, inert to acids, bases and other oxidizing mediators. A perfect autoclave should have certain characteristic features such as it should be leak proof, at required temperature and pressure and have adequate length to obtain a desired temperature gradient and should have capacity to withstand high temperature and pressure.

We used an ideal hydrothermal system (autoclave) manufactured by par instrument company UK (Fig. 2. 3) for all hydrothermal synthetic procedure.

Fig. 2.3: Autoclave used for hydrothermal synthesis.

We changed the temperature, duration of hydrothermal process and the solvent used in the hydrothermal process for different synthetic procedure. The important advantage of hydrothermal technique is that even at moderate temperature it is possible to obtain highly crystalline samples without doing further calcinations after hydrothermal process. The formation of crystalline sample is assisted by the high pressure formed inside the vessel with the applied temperature. The other advantages are i) one can control the morphology of thee sample ii) simple and less expensive iii) generally water is used as solvent for hydrothermal reaction hence the process is environment friendly.

2.4 Fundamental characterization techniques

The obtained titania nanotube arrays and modified nanotube arrays are characeraised by various technique like X-ray Diffractometer (XRD), Raman spectrometry, UV-Visible spectrometry, Diffused reflectance spectrometry, Scanning electron microscopy (SEM), Photoluminescence spectrometry, X-ray photon electron spectroscopy

and Electron paramagnetic spectrometry (EPR) and BET analysis. Photocatalytic activities of these samples were investigated with the help of immersion type photoreactors. The magnetic characterization was done by using vibrating sample magnetometer (VSM).

2.5. X-ray diffraction

X-ray powder diffraction is an efficient, rapid and non-destructive analytic technique primarily used for phase identification of a crystalline material and can provide information about the crystalline structure [4]. XRD analysis is also used to determine the grain size, composition of solid solution, lattice constants, and degree of crystallinity in a mixture of amorphous and crystalline substances. In an advanced manner this technique useful to study phase equilibria, texture analysis, stress measurement and to identify orientation of one crystal or the ensemble of orientations in polycrystalline aggregates.

2.5.1. Theory and Instrumentation

The theory behind the X-ray diffraction technique is based on Brags law [4, 5]. Brags law gives the relationship between the wavelength of the incident X-rays, angle of incidence and spacing between the crystal lattice planes of atoms, expressed as: $n \lambda = 2d \sin\theta$.
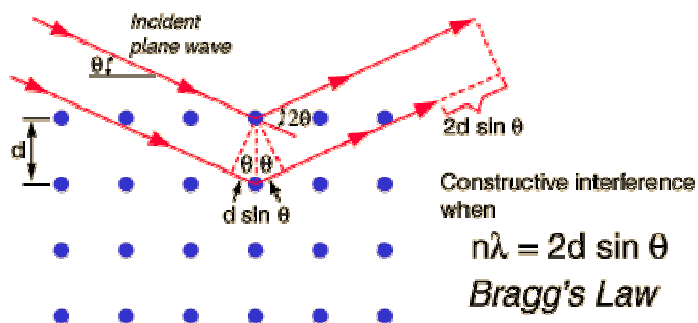
Fig. 2.4: Diffraction of X-rays by crystal planes.

In order to obtain effective diffraction pattern the incident radiation should be coherent, monochromatic and parallel. The spacing between the planes (d) of crystalline substance should be comparable with that of the order of λ. The X-ray radiation produced by a cathode ray tube, filtered to produce monochromatic radiations, then it is collimated to concentrate and directed towards the sample. The constructive interference of these monochromatic X-rays and a crystalline sample produce the diffraction pattern. The constructive interference produces when the conditions obey Bragg's law. All the diffracted rays from the different directions of the lattice planes are detected, processed and counted. Thus we can summaries that X-ray diffraction peaks are formed by constructive interference of a monochromatic beam of X-rays scattered at specific angles from each set of lattice planes in a sample. The peak intensities are determined by the distribution of atoms within the lattice.

Conversion of diffraction peaks to d-spacing is help to identify the crystalline material, since each sample has a set of unique value of d-

spacing. The result obtained is compared with that of standard pattern available known to be JCPDS files.

A normal X-ray powder diffractometer comprises of the following parts:

1) X-ray generator delivering high tension current to X-ray source- a vacumm sealed X-ray tube used as X-ray source

2) Sample holder to carry the sample to be investigated.

3) X-ray detector capable of measuring X-ray photons scattered by the sample; it may contain multiple channels in 1D or 2D arrangement.

4) X-ray optics assembled at the primary beam site and on secondary (diffracted) beam site for collimation, conditioning, or focusing of X-rays.

5) *Goniometer providing exact comparative angular positioning of X-ray source, sample and detector. The geomatry of an X-ray difractometer (Fig. 2.5b) is such that the samples rotates in the path of the collimated X-ray beam at an angle θ , while the X-ray detector is mounted on an arm to collect the diffracted x-rays and rotates at an agle 2θ.*
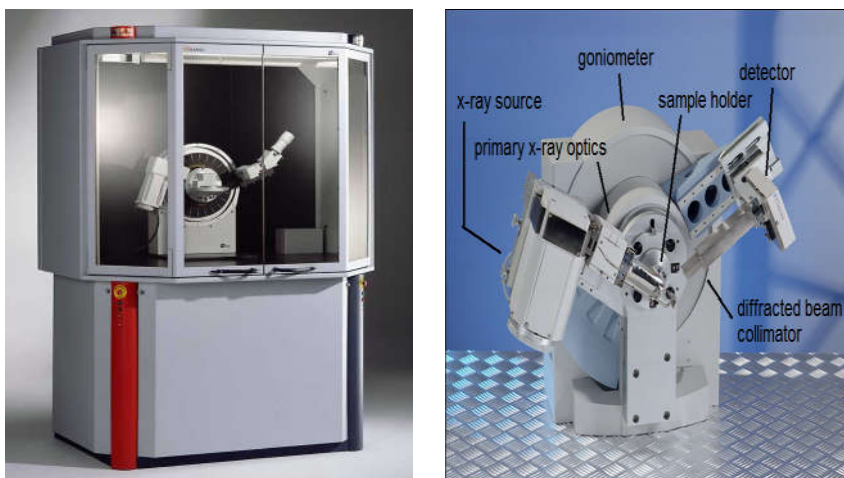
Fig. 2.5 a) Broker D8 X-ray diffractometer and b) parts of a typical X-ray diffractometer.

X-rays are produced in cathode ray tube by heating a filament to generate electrons and accelerating these electrons towards the target material by applying voltage, then by bombarding the target material with these electrons, to produce X-rays. The electron with sufficient energy removes the inner shell electrons of the target material. This produce characteristic X-ray spectrum. These spectra consists of several components, the most common being K_α and K_β, K_α consist $K_{\alpha1}$ and $K_{\alpha2}$. $K\alpha_1$ has slightly shorter wavelength and twice the intensity to that of $K\alpha_2$. The wavelength of X-rays is the characteristic of the target material (Cu, Fe, Mo, Cr). These X-rays are filtered by monochromators and produce monochromatic X-rays needed for the effective diffraction pattern. Cu is the most common target material for single-crystal diffraction, with CuKα radiation= 1.5418 A^0. As the detector and samples are rotated so that diffracted X-rays is recorded. When the diffracted ray obeys the Brag's law constructive interference

occurs and peak intensity occurs. Detectors records and process this X-ray signal and converts the signal to a count rate.

2.6 Raman spectroscopy

Raman spectroscopy is widely used for studying the structure of the materials. Raman effect is based upon the scattering of light. Solids, liquids, and gases are able to scatter the light according to molecular structure; hence the application of this technique can be extended to analyze wide variety of organic and inorganic compounds. This spectroscopy can be used for both qualitative as well as quantitative purpose. Qualitative analysis can be achieved by measuring the frequency of scattered radiations whereas quantitative analysis can be done by measuring the intensity of scattered radiations [6]

2.6.1 Theory and Instrumentation

Raman spectroscopy is based on scattering of radiation from the material. Scattering of radiation is leading Raman Effect i.e. The scattered radiations containing a small portion of radiations having higher or lower frequency than incident monochromatic light. The radiations having different frequency are formed due to the inelastic scattering of monochromatic radiation with vibrating molecules. It analyses the molecular vibrations [5]. The monochromatic light is interacted the sample molecules and originates scattered light. Raman spectrum is constructed using the scattered light having a frequency different from that of incident light. Raman spectral lines are formed due to inelastic collision between incident monochromatic radiation and molecules of sample. Most of the scattered radiations has

frequency which is same to the frequency of incident radiation and constitute Rayleigh scattering, while a small portion of scattered radiation have different frequency than that of incident monochromatic radiation and these scattered radiations construct Raman spectrum. Raman spectrum consists of two types of scattered radiations which responsible for two type spectral lines. The spectral lines arises from the scattered radiations having lower frequency with that of incident radiations known as Stockes line, where as the ones arises due to the scattered radiations having higher frequency is known to be anti-stockes lines (Fig. 2.6). Scattered radiation usually measures to right angles to the incident radiation. Usually Stockes lines are intense than Anti-stokes lines in conventional Raman spectroscopy, because Stokes shifted Raman bands involve the transitions from lower to higher energy vibrational levels. The magnitude of Raman shifts does not depend on wavelength of incident radiation, while Raman scattering depends on wavelength of incident radiation. Change in polarizability during molecular vibration is a vital condition (selection rule) to obtain Raman spectrum of a sample. Raman spectrum is meaningfully simpler than their Infrared spectrum because in normal Raman overtones, combination and difference bands are rare.

The figure shows energy level transitions for Rayleigh, Stokes Raman, and Anti-Stokes Raman scattering, with labels: $\tilde{v}_0$, $\tilde{v}' = \tilde{v}_0 - \tilde{v}_M$, $\tilde{v}' = \tilde{v}_0 + \tilde{v}_M$, $\tilde{v}_M$, "Excited States", "Ground vibrational States", "Rayleigh", "Stokes Raman", "Anti-Stokes Raman".
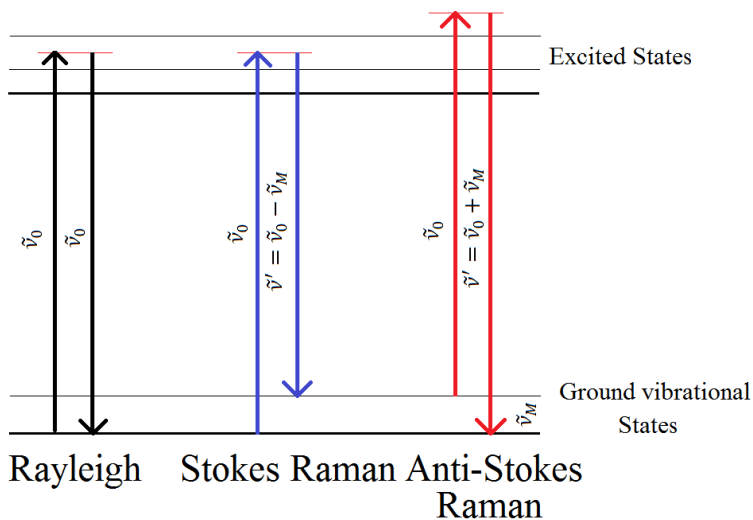
Fig. 2.6: Schematic representation of formation of Rayleigh, Stokes and Anti-stokes line.
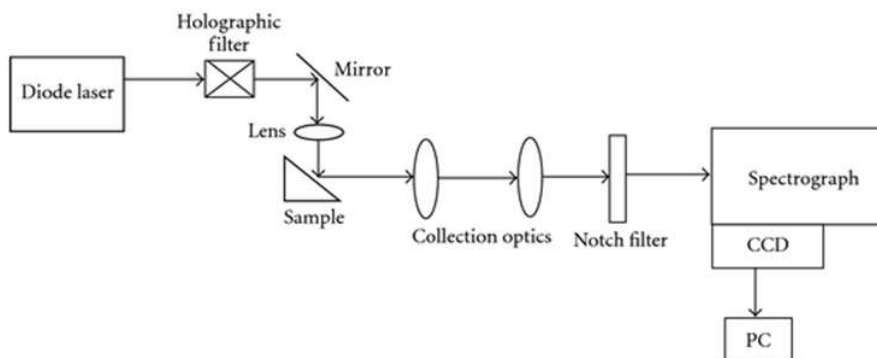
Fig. 2.7: Schematic representation of instrumentation of Raman spectrophotometer.

The following are the important parts of a typical Raman spectrometer [8, 9].

103

1).   Sample holder which holds the sample to be analyzed.

2).   A light source (laser).

3).   A collection optic to collect the Raman scattered photons.

4).   A monochromator to distinct the Raman signals into its constituent wavelengths.

5).   A detector to detect the photons at the various wavelengths where the Raman signal is produced by the sample. The detector gives an output which is a measure of the comparative intensities of the signals at these different wavelengths

6).   A computer system to store and display the spectral lines

Fig. 2.8: Photograph of thermo scientific laser (532nm) Raman spectrometer.

2.7 UV-Vis spectrometer

UV-Vis spectroscopy involves the study of the interaction of ultraviolet rays (300-400nm) or visible light (400-765 nm) with the molecule and the consequent energy changes occurring in the molecules [10]. When UV or visible light passed through the sample, it may absorb or reflect depends upon the sample nature. Hence this spectroscopy also known as absorption spectroscopy or reflectance spectroscopy. The energy of UV-visible light is sufficient to make electronic transitions in molecules and atoms. So UV-Vis spectroscopy is widely used for the understanding of band-gap potential and to characterize a material [11].

2.7.1 Theory and Instrumentation

Interaction of UV-vis light with mater brings electronic transition between molecular energy levels. The energy levels of matter are quantized, hence light energy with specific wavelength will needed to excite electrons from one lower energy level to higher energy levels. The absorbed light cause transition of electrons from different energy levels to exited states as shown in Figure 2. 9.
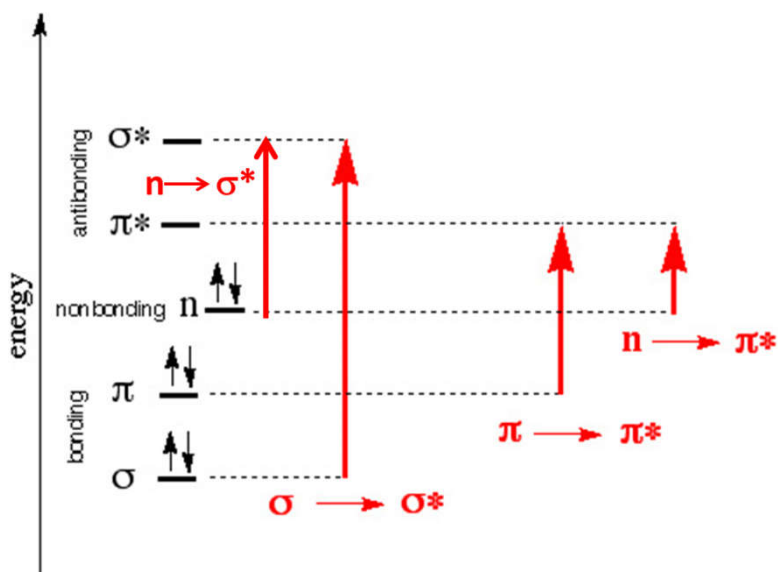
Fig. 2.9: Schematic representation of electronic transitions involves in different molecular orbital having different energy.

If the band-gap energy is very high, then transition to exited state is only possible by absorbing radiations having higher energy or frequency equivalent to that of band-gap energy. Thus the absorption is characteristic and depends on the type of electrons present in the system (σ, □ and n-electrons)

Types of transition

1) σ-σ* transitions

By absorbing radiations of specific wavelength the electrons excited from σ to corresponding antibonding σ* orbital. The energy needed for this transition is large and this type of transition is observed in saturate compounds. An Example is, C-H bond in CH_4 which can only undergo these types of transitions.

2) π-π* transitions

π electrons present in bonding orbital is exited to corresponding antibonding molecular orbital by absorbing specific amount of energy which is lee than that of σ-σ* transitions and n-σ* transitions, compounds having multiple bonds shows this type of transitions.

3)   n-σ* transitions

Saturated compounds containing hetero atom with unshared pair of electron (n) like oxygen, sulphur, nitrogen and halogens undergo this type of transition, need less energy than σ-σ* transition.

4)   n-π* transition

In this transition electron from non bonding orbital is transferred to π* antibonding molecular orbital. Energy required is less compared to other transitions. Compounds having double bonds with hetero atoms shows this kind of transition (N=O, C=O etc)
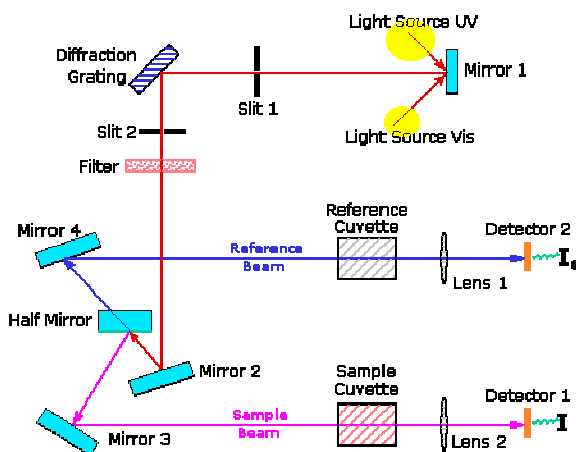
Fig. 2.10: Instrumentation of a typical UV-vis spectrometer.

In UV-vis spectroscopy the electromagnetic radiations involved are UV-vis light. Deuterium lamps and tungsten lamps are usually using as the source of UV and visible light respectively. The sample is illuminated by the entire band of UV or visible light by the source. The grating or monochromator changes the entire region of UV or visible light to small bands and sent these radiations to beam splitter. The beam splitter sent separate light to sample and to reference. Then the detectors measures the difference between the transmitted light through the sample (I) and reference (I_0) and sends this information to the recorder and then process it. The result obtained may in terms of absorbance ($A = \log I_o/I$) or in term of transmittance or reflectance against the wavelength. Reflectance spectra obtained by measuring the reflectance produced by the sample. The amount of absorption of UV-vis light by the sample is based on Beer lambert law, which states that the intensity of absorption of light by a sample is directly proportional to concentration and length of the sample ($A = \varepsilon c\, l$, where ε is molar absorptivity constant) [11].

Fig. 2.11: Photograph of UV-Vis spectrometer (Perkinelemer-lamda).

2.8 Photo-luminescence spectroscopy

Luminescence is a phenomenon which involves absorption of energy and successive emission of light. Based on the nature of emission process there are two types of emission process, fluorescence and phosphorescence. Fluorescence is "fast" (*ns* time scale) while phosphorescence is "slow" (longer time scale, up to *hours* or even days). PL spectroscopy widely used to identify the intermediate energy levels present within the band-gap in the molecules. It also helps to identify the nature of band structure [12].

2.8.1 Theory and Instrumentation

There is mainly two type of molecular luminescence spectroscopy 1) Fluorescence spectroscopy 2) Phosphorescence spectroscopy. In fluorescence spectroscopy the chemical species at exited state undergo some internal energy transition (from singlet to singlet state) before relaxing to ground state, by emitting photons. Some of the absorbed energy may dissipate during this process. So the emitted photons have less energy than the absorbed photons energy since some of the absorbed energy in the system is dissipated. Fluorescence emission taking place within seconds (10^{-8} to $10^{-4}s$). The life time of phosphorescence emission is more than that of fluorescence spectroscopy (10^{-4} to 10^{-2} s) hence the chance for occurring phosphorescence is less when comparing with that of fluorescence. It is a radiational transition, in which the exited chemical species undergo intersystem crossing having different multiplicity as shown in Figure 2.12. The diagram which provides the detailed emission of photon

energy from the exited state is given in the Jablonski diagram (Fig 2.12)
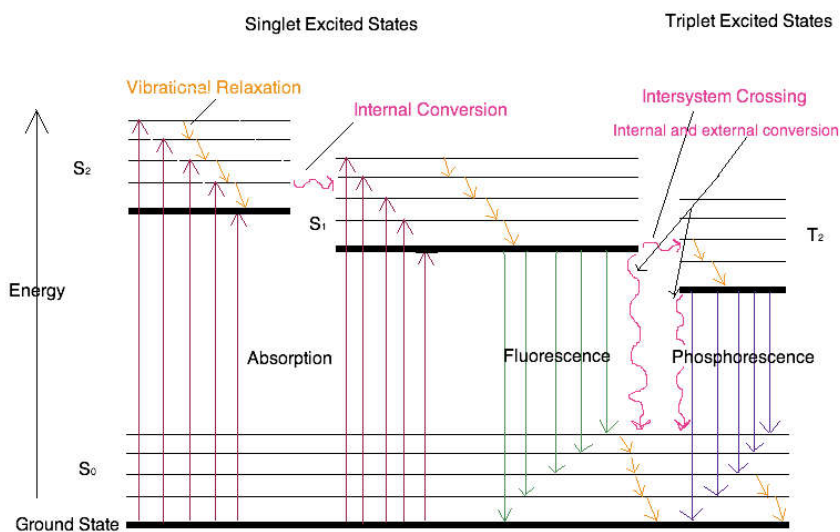
Fig. 2.12: Jabolonski diagram representing the fluorescence and phosphorescence transitions.
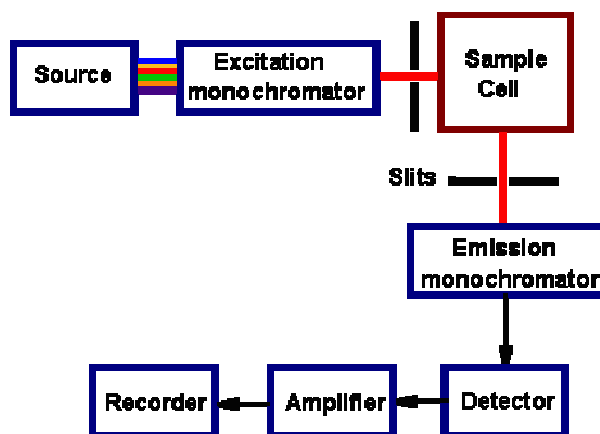
Fig. 2.13: Schematic diagram of the components in a typical PL spectrophotometer.

Low pressure mercury lamp fused with silica window, A 75 -100 *W* high pressure xenon-arc lamp and LASER are the different kinds of sources used   in spectrofluorometer. For wavelength selection of both the excitation beam and the resulting luminescence radiation interface and absorption filters have been used in PL-spectrometer. Most spectrofluorometers are equipped with at least one and occasionally two grating monochromators. The most general transducer used in a sensitive fluorometer is photomultiplier tubes. The schematic representation of the components of PL-spectrophotometer is given in Figure 2. 13.

2.9 X-ray photo electron spectroscopy

X-ray photoelectron spectroscopy (XPS), is a surface sensitive electron spectroscopic technique for chemical analysis (ESCA), which is widely used for analyzing the surface chemistry of a material. XPS can measure the, electronic state, binding energy of electrons, chemical state, elemental composition and empirical formula, of the elements in a material [13].

2.9.1 Theory and Instrumentation

The theory of XPS is based on photoelectric effect. Surface properties of different chemical species are different and it may be different from the interior of the material. An intense beam of X-rays or UV rays will ionize the molecules or atoms. The source light used must have energy to ionize the material. Electrons may also eject from deeper levels. When X-rays were incident to the surface, the inner electrons will

eject. XPS spectrum is obtained according to the characteristics of ejected electrons [14].
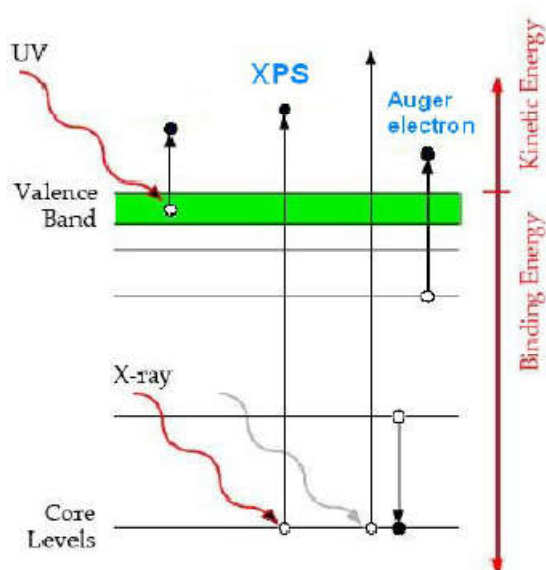
Fig. 2.14: Photoelectron ejection from a material due to an incident photon.

When the surface of the material is irradiated by X-ray having energy of 'hν'. Some of the (mono-energetic) photons hit out the electron from atoms in the surface region. Photons having higher energy 'hν' enter deeper into the samples surface. Electrons released by photons from lower energy X-rays creates from inner atomic energy levels are known to be photoelectrons and these electrons were bound to atomic nuclei with the binding energy E_b. When an electron from inner orbital is ejected, a hole is created and to compensate this an electron from outer orbital is transferred to this hole site, by releasing energy. This energy transferred another electron present in the outer orbital and is ejected from the orbital, this ejected electrons are known to be Auger

electrons. XPS instrument measures the kinetic energy of all ejected electrons (electrons of both photoelectrons and auger electrons). The kinetic energy of emitted electrons can be calculated by using the equations 2.1and 2.2

$$\text{KE (Kinetic energy)} = h\nu - \text{BE} - \phi_{spec} \underline{\hspace{2cm}} 2.1$$

$$\text{BE (electron)} \quad = h\nu - \text{KE} - \phi_{spec} \underline{\hspace{2cm}} 2.2$$

Where KE= electron kinetic energy, BE= Binding energy of electron, ϕ_{spec}= spectrometer work function.

Thus the binding energy of emitted electron is calculated and compared with that of the reference samples. The result obtained in XPS measurement is in the form emission intensity vs binding energy graph. The area of XPS peak can be used to obtain the concentration of elements. So both binding energy and area of peak will help to analyze the material. XPS measurements can be only applicable to the elements having atomic number 3 or greater than 3. Ultra high vacuum condition is necessary during XPS analysis. High vacuum condition prevents contamination of the surface and hence gets accurate results.
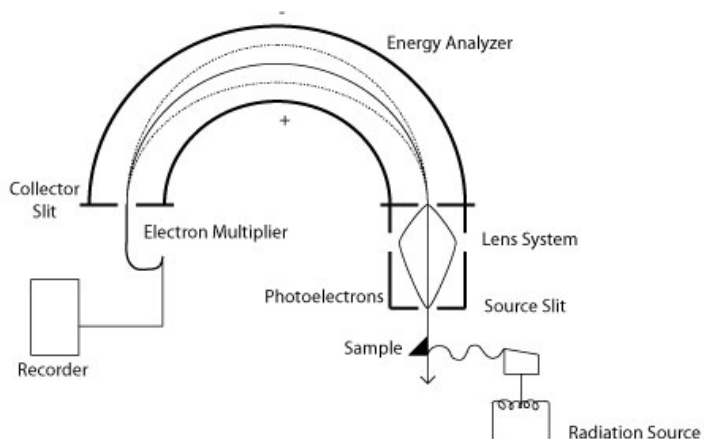
Fig. 2.15: Schematic representation of Components of XPS instrument.

Different components of XPS are provided in Figure 2.15. The important parts of XPS are radiation (X-ray) source, ultra-high vacuum stainless chamber, Lens system for electron collection, electron analyzer and an electron detector system. The source may monochromatic beam of few microns, or unfocused non-monochromatic beam of couple of centimeters. The common source material are Mg or Al Kα providing X-rays having energy 1486.7 eV and 1258 eV. Electron gun also used in combination with X-rays to eject electrons. Electron analyzers are another important component of electron spectroscopic analyzers. Mainly two classes of analyzers are there 1) Kinetic energy analyzers 2) deflection (electrostatic) analyzers. When the kinetic energy photoelectrons are high then lower the resolution of the spectra obtained, in case kinetic energy analyzers. Deflection analyzers (electrostatic analyzers) are capable to distinct out photoelectrons through an electric field by imposing electrons to follow dissimilar paths according to their velocities. The most common type analyzer used in XPS is hemispherical analyzer, which is belongs

114

to the class of deflection analyzers. As the kinetic energy of the emitted photon increases, lower the resolution intensity for the obtained results. This can be solved by using (optic) lenses in XPS, the lenses system are able to slowing own the kinetic energy of the photoelectrons through the retardation of electric field. This greatly helps to increase the resolution, but it lowers the sensitivity. The lenses can also increase the velocity of photoelectrons and help to focus a small area of the sample. Electron analyzer analyses the kinetic energy of the emitted electrons and detector count the number of electrons ejected.

Fig. 2.16: Photograph of an XPS instrument (Axis-Ultra, Kratos Analytical, Source Al-Kα).

2.10 Electron Paramagnetic Spectroscopy (EPR) or Electron spin resonance (ESR) spectroscopy

Electron paramagnetic spectroscopy (EPR) spectroscopy is a powerful and sensitive spectroscopic technique widely used for the characterization of the electronic structures of substances with unpaired electron. In this spectroscopic technique, the microwave

region of the electromagnetic spectrum is absorbed by substance having unpaired electrons, and encourages transition between magnetic energy levels of unpaired electrons. This spectroscopy helped to understand the nature of environment of unpaired electron and to study electronic state, defects, present in the materials. There are different kinds of EPR technique like continues wave EPR (CW-ESR), electron nuclear double resonance (ENDOR), electron spin echo envelope modulation (ESEEM). In continues, wave EPR, the material is exposed to a beam of microwave irradiation of fixed frequency and the magnetic field is changed. Different microwave frequencies is used in EPR, and they are denoted as S-band (3.5 *GHz*), X-band (9.25 *GHz*), K-band (20 *GHz*), Q-band (35 *GHz*), and W-band (95 *GHz* [15, 16].

2.10.1 Theory and Instrumentation

Electron is a particle having negative charge with certain mass. Electrons have two type of motion, around the nucleus and its own axis. The motion around the axis produces orbital magnetic moment, whereas the spinning motion of electron around its own axis creates spin magnetic moment. The unpaired electron's spin magnetic moment has a major contribution to the total magnetic moment. Electron paramagnetic resonance is a magnetic resonance method, based on the interaction of unpaired electron spins with external magnetic field. If an electron is placed in an applied magnetic field B0, the degenerate energy state may split into two, one corresponding to parallel spin state and the other corresponds to antiparallel state as shown below (Fig. 2. 17).
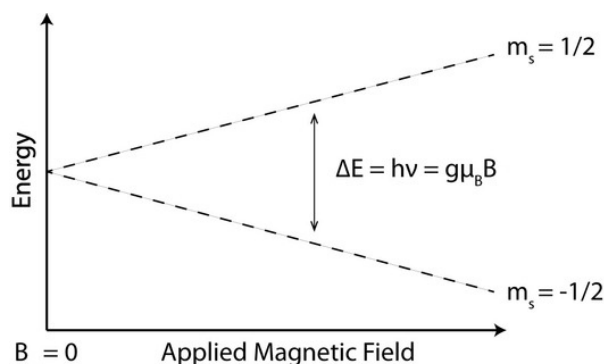
Fig. 2.17: Energy level of an electron spin in an applied magnetic field.

Energy of electron having spin $+\dfrac{1}{2} = +\dfrac{1}{2}g\mu_B B$

Energy of electron having spin $-\dfrac{1}{2} = -\dfrac{1}{2}g\mu_B B$,

Where g- is proportionality factor (free electron g-factor), μ_B=Bohr magneton, B-is the applied magnetic field.

In the absence of magnetic field the E+1/2= E-1/2=0, while in the presence of external magnetic field, the difference between the two spin energy states is given by $\Delta E=h\nu=g\mu_B B$ (as shown in Figure 2. 17). As the intensity of applied magnetic field increases, the energy difference between the two level increases and when it is equivalent to microwave radiation the electron will absorb photon of energy and flip to other spin sate or exited to other energy spin state from the corresponding antiparallel spin state. This is the basic theory involved in EPR spectroscopy. Thus EPR spectroscopy is widely used to species having unpaired electrons like radicals, transition metal compounds etc. EPR signal may split number of signal peaks by interacting with

117

neighboring nuclei known to be hyperfine splitting. This hyperfine splitting provides information about the number of identity nuclei and distance of unpaired electrons from the neighboring nuclei. If there is N number of nuclei having spin value I then, the EPR signal split into (2NI+1) numbers and the intensity follow binomial distribution [15].
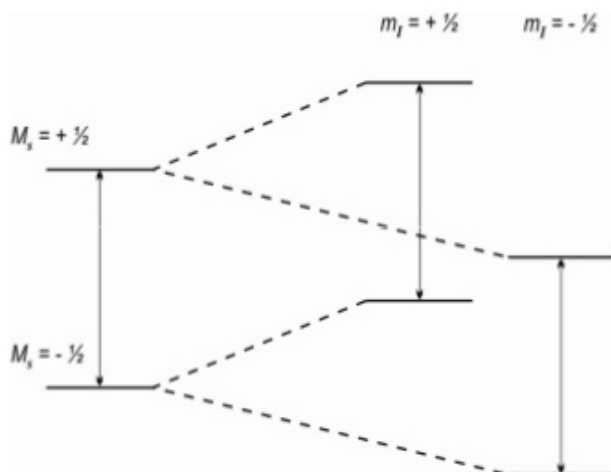
Fig. 2.18: Interaction of an EPR signal with single nucleus of ½ spin.
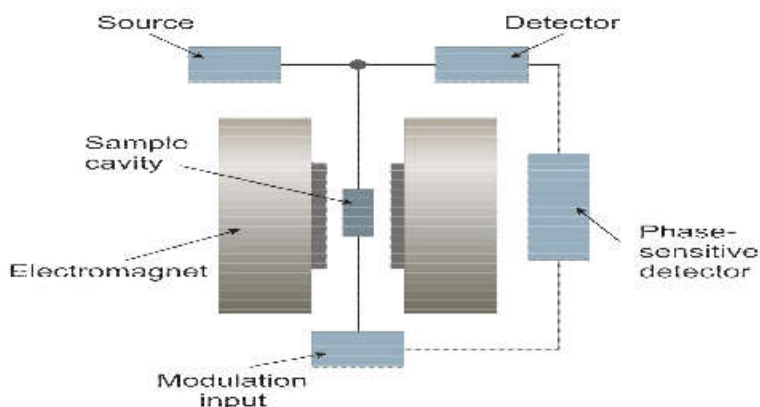
Fig. 2.19: Components of a typical EPR spectrometer.

In EPR spectroscopy, normally Klystron tube act as source of microwave radiation. The frequency of the monochromatic radiation is controlled by voltage applied to Klystron source and it is fixed in fixed frequency level. Wave guide or wave meter is one of the major parts of the instrument, the wave guide (wave meter) used to know the microwave frequency produced by the Klystron source, which is placed in between the oscillator and attenuator. The wave meter usually made up of hollow, rectangular brass tube. Variable attenuator is used to varying the power of sample from the full power Klystron. Isolators are also used to control the frequency of microwave radiation produced by Klystron and it minimizes vibrations in the frequency of microwave produced by Klystron source and it also prevent the reflection of microwave radiation back into the source. Sample cavities are the heart of the EPR spectrometer which is a resonant cavity, containing the sample. Cylindrical TE011 cavity, Rotable cavity (for

studying anisotropic effect) and Rectangular TE120 cavity have commonly been used. Rotable cavities and Dual sample cavities are widely used in EPR spectrometers, one for sample and other for reference. The quality of cavity is represented by a factor known to be Q factor. Detectors used in EPR spectroscope are generally made up of silicon, which convert the radiation in DC. Microwave bridge such as Magic T and hybrid are other common type detector. The resonant cavity is kept in the poles of an electromagnet. A magnetic field of at least 5000 *gause* is essential for EPR spectroscopy, which produced by the electromagnetic system. The produced field should be uniform and stable over the sample. The modulation of the signal at frequency steady with good signal to noise ratio in the detector is attained by modulation coil unit by a small alternating variation of the magnetic field [16, 17]. A cathode ray oscilloscope is used in EPR spectrometer to adjust the spectrometer and to observe the signal.

Fig. 2.20: Photograph of EPR spectrometer (Model- JEOL-JES).

2. 11 BET surface area analyzer

One of the important characteristics of nanomaterial is their surface area. Many of the intrinsic properties of nanomaterial is associated with their surface area/ volume ratio. As the surface area of the materiel is increases, catlytical activity also increases. Therefore the aquarate measurement of the surface area of nanomaterial is important to characterize the material. Brunnauer-Emmett-Teller (BET) surface adsorption is the most general method used to measure the surface area of the materials.

2.11.1 Theory and Instrumentation

BET surface area analysis is based on the theory put forward by Brunauer-Emmett-Teller, which explains the multilayer physical adsorption of the adsorbent (usually gas molecule) on solid surface. According to BET theory the multilayer adsorption of adsorbent molecule on solid surface is based on certain assumptions. The important assumptions are i) the adsorption is purely physical, ii) the surface of the solid material is entirely uniform there is no preferential adsorption sites, iii) the adsorbed gas molecule has limited interactions it interacts only with neighboring layer, iv) each adsorbed layer obey the Langmuir theory which is applicable to monomolecular layer, based on these assumptions Brunauer-Emmett-Teller derived an equation known to be BET equation, (given below in equation 2.3).

$$v = \frac{v_m c p}{(p_0 - p)[1 + (c - 1)\left(\frac{p}{p_0}\right)]} \qquad\qquad 2.3$$

Where V = volume of adsorbed gas; V_m = adsorbed monolayer volume; p_0 = saturation gas pressure: p = equilibrium gas pressure, c = BET constant. The equation can be re-arranged as, which is same as straight line equation y= mx+ c

$$\frac{1}{v[(\frac{p}{p_0}) - 1]} = \frac{c-1}{v_m c}\left(\frac{p}{p_0}\right) + \frac{1}{v_m c} \qquad\qquad 2.4$$

From the graphical plot of the above equation it is possible to find out BET constant (*c*) [*slope/ (intercept+1)*] and adsorbed monolayer volume (*V$_m$*) [*1/ (slope+intercept)*]. From the obtained adsorbed monolayer volume one can easily calculate the specific surface area using the following equation 2.5.

$$S_{spe} = \frac{V_m NA}{22,400\ X\ m} \qquad\qquad 2.5$$

Where N is Avogadro number, A is cross-sectional surface area of single adsorbed gas molecule, and m is the mass of nanomaterial used for measurement. Generally in BET surface area analyzers N_2 gas is used as adsorbent. The volume of the gas adsorbed on the solid surface is measured at the boiling point of liquid nitrogen

Fig. 2.21: Photograph of BET surface area analyzer (Quantachrome, Nova).

2. 12 Vibrating Sample Magnetometer (VSM)

Vibrating Sample Magnetometry is a measurement method which allows determining the magnetic moment of a sample with good precision. The basic principle of VSM technique is based on Faraday's law which states that an electromagnetic force is created within the coil when there is alteration in flux through the coil [18].

2.12.1 Theory and Instrumentation

The working principle of the VSM is relatively simple: a sample is vibrated in between a couple of pick-up coils, and then a dc magnetic field is applied to the sample (normally in a direction perpendicular to the coils). The magnetic field magnetizes the sample. The vibrating magnetic moment generates a flux that fluctuates with time and, accordingly results in an ac voltage being induced in detection coils. The signals from the coils are identified with a lock in amplifier. This lock-in amplifier gives a dc voltage output which is proportional to the magnetic moment of the material. Thus from Vibrating sample

magnetometer we can measure the magnetization of a sample as a function of magnetic field (magnetization curve) [18].
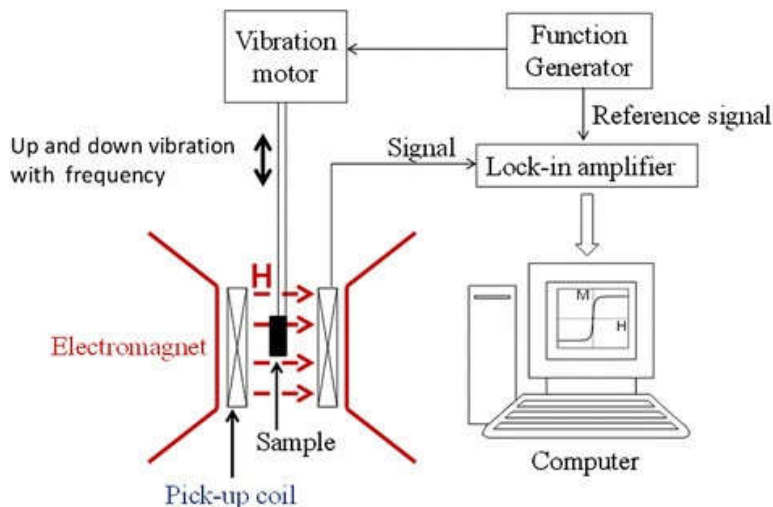
Fig. 2.22: Components of Vibrating Sample Magnetometer.

In VSM, during sample analysis the magnetic sample is moving in the proximity of two pick up coils as shown in Figure 2. 22. A sinusoidal signal provided by the oscillator is transmitted by the transducer assembly into a vertical vibration. Generally the sample is kept at sample rod vibrates with a given frequency and amplitude (60 to 80 *Hz* and 1*mm* respectively). This sample is also centered in between the two pole pieces of an electromagnet that creates a magnetic field H_0 of high frequency [18].

Fig. 2.23: Vibrating Sample Magnetometer (Lakeshore, Model: 7410 series).

2. 13 Scanning Electron Microscopy (SEM)

Scanning Electron Microscope is a superior model of electron microscope and "non-destructive" sample analysis technique. SEM widely used to find out the three dimensional image of samples especially for the surface structure and cross section image. The three dimensional image of the sample is developed due to secondary electrons, back scattered electrons (BSD), and diffracted back scattered electrons (EBSD) arising from the sample. Energy dispersive X-ray spectroscopy (EDS) attached SEM is helpful to know the elements present in the samples. For morphological and elemental identifications SEM attached with EDS is plying a crucial role in the area of research [19].

2.13.1 Theory and Instrumentation

Accelerated electrons from the source of SEM have high kinetic energy. These electrons interact with sample in inelastic and elastic manner. Due to this interaction with sample various types of signals are produced from the sample by utilizing the energy of accelerated electron. These signals include secondary electrons, back scattered electrons, diffracted back scattered electrons, photons (characteristic X-rays) and heat. Secondary electrons responsible for the production of SEM image or help to identify the morphology of the sample, back scattered electrons, and diffracted back electrons may help to know the crystal structure and the ordinations of minerals samples, whereas photons characteristics of X-rays used for elemental analysis. These various types of secondary electrons collected by the detector, and amplified. Then corresponding results are observed in the attached computer system [13, 20]
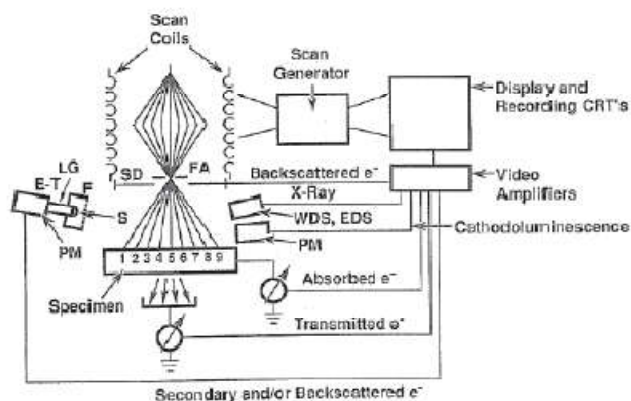
Fig. 2.24: Schematic representation of production of secondary/ back scattered electrons and production of image.

126

The important parts of Scanning Electron Microscope are

1) **Source of electron (Electron gun):** Electrons are generated by thermionic heating at the source. The electrons produced are then accelerated to a voltage 1-40 *kv,* and converted into a narrow beam. These electrons are used for analysis. The common sources of SEM are a) Tungsten filament b) Field emission gun c) solid state crystal (CeB_6 or LaB_6).

2) **Electron lenses:** In order to narrow down the electron beam as it moves from source to sample, a series of condensed lenses are used which are known to be Electron lenses. As narrower the beam, the smaller spot the electrons contacting with the sample.

3) **Sample stage (Sample chamber):** Samples are placed in a sample stage which is evacuated. The sample chamber consists of translation stage, rotation devices, tilt, temperature stages and optical cameras to assist the sample imaging process.

4) **Detectors:** Two types of detectors are used secondary electron detectors and back scattered electron detectors. Secondary electrons detectors are detectors used to detect secondary electrons having low energy and are produced from k-shell of the sample. Most general secondary electron detectors used in scanning electron microscopy is Everheart-thornley detector. Signal produced by the detector is amplified by photomultiplier tube attached to it. Back scattered electron detect back scattered electrons having high energy. These electrons are produced by

elastic scattering of electrons in the atoms. Atoms having high atomic number back scatter electrons efficiently and give compositional details of samples. Semiconductor detectors or Scintilators are most common back scattered detectors used in SEM. The components of SEM instrument is provided in Figure 2.25.
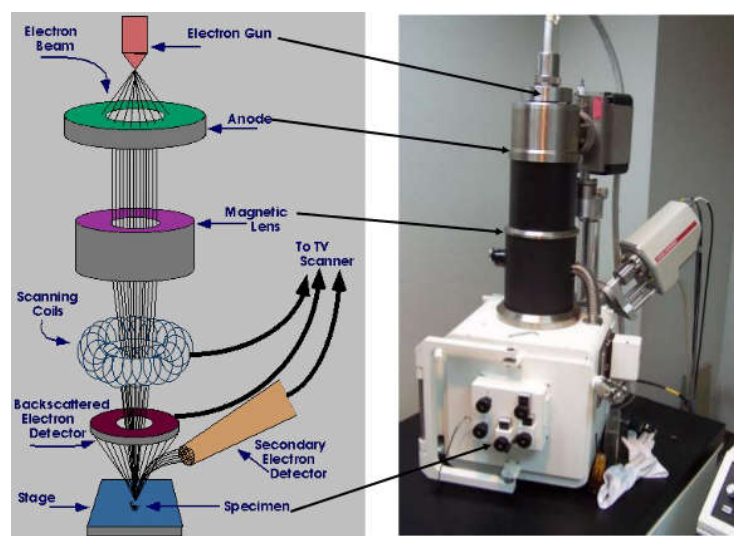
Fig. 2.25: Components of a typical Scanning Electron Microscope.

2.13. 2 Field Emission Scanning Electron Microscopy (FESEM)

FESEM is an advanced version of normal SEM. The working principle is same, but in case of normal SEM, thermionic emitters are used as source, where as in case of FESEM, field emitters are use source of the electrons. Thermionic emitters use electric current to heat up the filament material of source and when a temperature reach up to the work function of the material the electrons were ejected from the material. This method has lot of disadvantage like low brightness,

evaporation of cathode material, thermal drifting etc. All the above mentioned problems can be avoided by using field emitter as source. Electrons are emitted from the element, by placing the material within a huge electrical potential gradient. This will not heat up the filament material. Hence in FESEM the electron beam is more powerful. The magnification and resolution power is higher in case of FESEM and the picture quality obtained has better quality.

Fig. 2.26: Photograph of a typical FESEM (model FEI, Nova Nano SEM 450).

2.14 Photocatalytic study-Experimental set up

In order to study the photocatalytic activity of prepared samples in UV and visible light we need source of both UV and visible light of suitable wavelength. We used methylene blue (MB) has a model dye for photocatalytic studies. For all photocatalytic studies the films having an area 1 cm^2 was placed in cuvette containing MB solution of concentration 8.5 mg/L. The above cuvette was placed in dark in order

to acquire adsorption-desorption equilibrium. The dye solution containing the cuvette was subsequently illuminated with the corresponding UV or visible light source to study the photocatalytic activity of the samples. The dye degradation was monitored at different time intervals by measuring the concentration of MB using absorption spectra of the dye with a UV-Vis spectrometer.

2.14.1 Photoreactor

For studying photocatalytic activity in UV light, we used 6 numbers of 15W tungsten lamp (Philips UV light, G15, T8, and Holland) attached with a UV filter as UV source. For studying visible light photocatalytic activity we used immersion type photoreactor having a visible light source of 300 W, tungsten lamp (HEBER, India).The experimental set up used for visible light photocatalytic activity is shown in Figure 2.27.
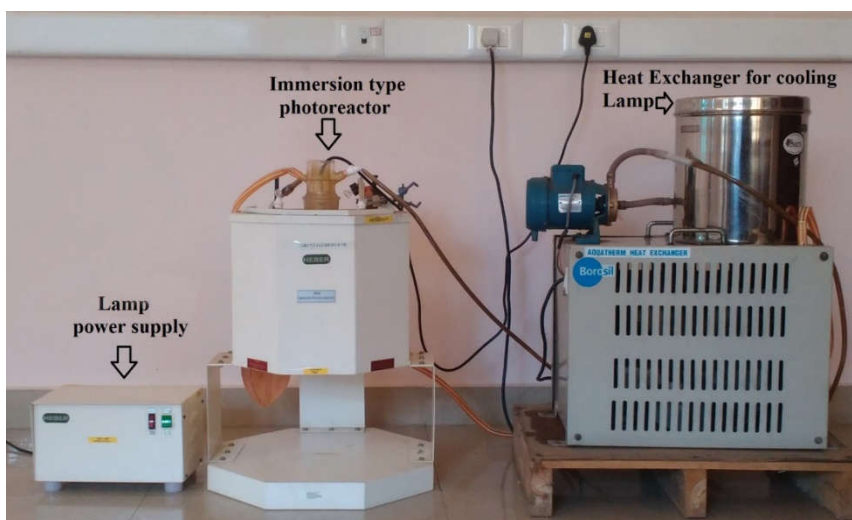
Fig. 2.27: Experimental set up used for visible light photocatalytic activity.

References

[1]   G. K. Mor, O. K.Varghese, M. Paulose, K. Shankar, C. A. Grimes, A review on highly ordered, vertically oriented TiO_2 nanotube arrays: Fabrication, material properties, and solar energy applications, Sol. Energy Mater. Sol. Cells 90 (2006) 2011-2075.

[2]   K. Byrappa, (Ed.), Hydrothermal Growth of Crystals, pp. 1–365, Pergamon Press, Oxford, UK ,1992 (170).

[3]   K. Byrappa, M. Yoshimura, Handbook of Hydrothermal Technology, Noyes Publications, New Jersey, USA, 2001 (171).

[4]   B. D. Cullity, Elements of X-ray diffraction, 2nd edition, Addison-Wesley, 1978, ISBN-10: 0201011743.

[5]   B. E. Warren, X-ray diffraction, Addison-Wesley, 1969, Dover publications New-York.

[6]   G. S. Bumbrah, R. M. Sharma, Raman spectroscopy − Basic principle, instrumentation and selected applications for the characterization of drugs of abuse, Egyptian Journal of Forensic Science, 6 (2016) 209-215.

[7]   J. R. Ferraro, K. Nakamoto, C. W. Brown (200, Introductory Raman Spectroscopy, (2003) Academic Press.

[8]   P. Pujary, K. Maheedhar, M. K. Chilkapati, K. Pujary (2011),Raman Spectroscopic Methods for Classification of Normal and Malignant Hypopharyngeal Tissues: An Exploratory Study, Patholog. Res. Int. Volume 2011, Article ID 632493, 9 pages

[9]   E. Smith, G. Dent, Modern Raman Spectroscopy, (2005) John Wiley & Sons Ltd.

[10]   D. A. Skoog, D. M. West, Principles of instrumental analysis, J. Chem. Educ. 58 (1981) A314.

[11]   G. D. Christian, Analytical Chemistry, 6th edition, John Wiley & Sons, Inc; (2004) Hoboken, New-Jersey.

[12]   R. L. Sutherland, Handbook of nonlinear optics, Marcel Dekker, (2003) New-York, 2nd Edition.

[13]   D. A. Skoog, F. A. James, S. R. Crouch, Principles of Instrumental Analysis, (2007) Brooks/Cole, Publishing, India

[14]   P. van der Heide, X-Ray Photoelectron Spectroscopy: An Introduction to Principles and Practices, (2011), John Wiley & Sons, Inc.

[15]   B. M. Beckhuysen, R. Heidler, R. A. Schoonheydt, Electron spin resonance spectroscopy, Mol. Sieves, 4 (2004) 295-335.

[16]   H. H. Willard, Instrumental Methods Of Chemical Analysis, 7th Edition, (2012) CBS Publishers And Distributers, New Delhi.

[17]   B. K. Sharma, Instrumental Methods Of Chemical Analysis, in Introduction to Analytical Chemistry, Goel Publishing House (2004) Meerut, 23rd Edition.

[18]   A. Earnshaw, Introduction to Magnetometry, Academic Press, London (1968) New-York.

[19]   J. I. Goldstein, D. E. Newbury, J. R. Michael, N. W. M. Ritchie, J. H. J. Scoot, D. C. Joy, Scanning Electron Microscopy and X-ray microanalysis, 4th Edition, Springer (2018) New-York.

[20]   J. I. Goldstein, D. E. Newbury, D. C. Joy, C. E. Lyman, P. Echlin, E. Lifshin, L. Sawyer, J. R. Michel, Scanning Electron Microscopy and X-ray Microanalysis, 3rd Edition (2003) Springer.

MANOJ N. "INFLUENCE OF MORPHOLOGY AND SURFACE MODIFICATIONS ON THE PHOTOCATALYTIC ACTIVITY OF TITANIA-BASED NANO TUBE ARRAYS". THESIS. CENTRE FOR MATERIALS FOR ELECTRONICS TECHNOLOGY [C-MET], UNIVERSITY OF CALICUT, 2018.

CHAPTER 3
Titania Nanotube Arrays surface-modified with ZnO for enhanced photocatalytic applications

CONTENTS

Some of the contents in this chapter have appeared in the following publication.

3. 1 Introduction

Heterogeneous nanostructures of semiconductors are being increasingly studied in a wide range of applications especially in photocatalysis and Dye-Sensitized Solar Cells (DSSC) [1-2]. Among the semiconductors, titania (TiO_2) and zinc oxide (ZnO) find more applications owing to their lower toxicity and cost [3-6]. Morphology of the material plays an important role to decide the photocatalytic activity of the material. In order to study the morphological influence and its role in photocatlysis, researchers were prepared materials having different morphology and studied their photocatalytic activity. D. Gong et al reported the fabrication of highly ordered titania nanotube arrays (TNA) by anodic oxidation of Ti metal and they employed anodisation process for the oxidation of Ti-metal foil. The anodisation set up employed consists of an electrolyte of 0.5 to 3.5 *wt%* of hydrofluoric acid. The authors applied different voltage across the electrodes and found that average tube diameter varies from 25 to 65 *nm* with increasing anodizing voltage, while the length has no change and independent of applied voltage. Since then several studies have focused on the nanotubular morphology in enhancing their applications in hydrogen sensing, photocatalysis and DSSC [8-10]. K. Zhu studied the Enhanced charge collection and light scattering property of nanotube arrays of TiO_2 in DSSC which shows, the advantage of nanotube array structure in such applications [10]. Modification of TNA with elements (including non metals, metalloids, metals) like N_2, C, B, Fe, V, Ag [11-16] and semiconductors like CdS, PbS, Fe_2O_3, Ag_2S have also been reported [17-20] to yield enhanced

photoresponse under visible and UV light. As we mentioned above ZnO and TiO$_2$ attracted much interest in photocatalysis due to their attractive features such as lower toxicity, low cost and easiness of preparation, suitable band-gap.
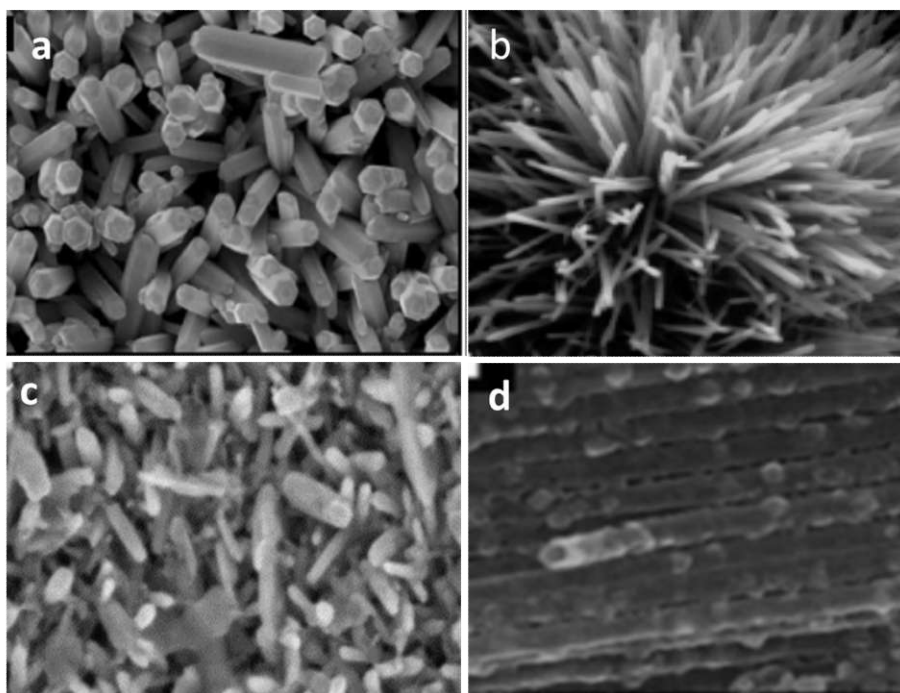
Fig. 3.1: SEM images of the surface of a) ZnO/TiO$_2$ nanocomposite reported by S. Benkara et al [21]; b) ZnO@TiO2 nanotube heterostructure reported by Y. Lei et al [22]; c) ZnO/TiO$_2$, nanorod/ nanotube hybrid nanomaterial reported by Z. Zhang et al and d) Cross sectional SEM image of ZnO nanoparticles impregnated in between the tube reported by F. X. Xiao.

Nanostructures in the ZnO-TiO$_2$ system reported so far include nanocomposites of ZnO nanorods and TiO$_2$ nanotubes [21-23], ZnO nanocrystals impregnated in TNA [24] and ZnO@TiO$_2$ core-shell heterostructures [25, 26]. S. Benkara et al prepared ZnO/TiO$_2$ nanotube array composite, in which ZnO have rod like structure (Fig.

3.1a) through hydrothermal method [21]. Sol-gel method and hydrothermal reactions were combined by Y. Lei et al to deposit ZnO nanorods on TiO_2 nanotube arrays [22]. In this heterostructure ZnO nanorods were grown in flower like clusters as shown in Figure 3.1b. Z. Zhang et al [23] applied cathodic electrode deposition method to deposit ZnO nanorods on TiO_2 nanotubes (Fig. 3.1c). Impregnations of ZnO nanoparticle in between the TiO_2 nanotubes were also reported by F. X. Xiao (Fig. 3.1d). The author employed pyrolysis method to impregnate ZnO nanoparticles in between the tubes.

In all of the above mentioned studies the deposited ZnO nanoparticles have almost same morphology. Surface modification of TNA by ZnO nanoparticles having different morphologies has not yet been reported. Therefore, fabrication of TNA/ZnO heterostructures has attracted much interest. In such heterostructures the surface morphology and texture are expected to significantly influence their photocatalytic activity. Therefore in this study, we report the fabrication of TNA/ZnO heterostructures in which ZnO nanoparticles having different morphologies have been deposited on TNA by hydrothermal method and correlate their surface morphology and texture with their photocatalytic activity.

3. 2 Experimental details

Ethylene glycol (99%, Merck), Zinc nitrate hexahydrate (96%, Merck), Ammonium fluoride (98%, Sigma Aldrich), Urea (99.1%, Sigma Aldrich) and Titanium metal foil (99.7%, Aldrich) were used as such for the fabrication of the heterostructures.

Titania nanotube arrays (TNA) were synthesised by anodisation of titanium metal foil (3.0 x 1.0 x 0.25 mm) in a two electrode cell with titanium metal foil as working electrode and Pt rod as counter electrode in an ethylene glycol-fluoride electrolyte at 40 V for 24 h followed by washing and calcination at 400^0C for crystallization, using a modified method as reported earlier [27]. Prior to anodisation the titanium foil was sonicated in acetone for 10 $minutes$ then washed with distilled water and dried. The electrolyte for anodisation was prepared by dissolving NH_4F (0.16 M) in an ethylene glycol (96.5 ml) and water (3.5 ml) mixture.

The prepared TNA were immersed in a solution containing $0.15M$ zinc nitrate hexahydrate and 3.02 M solution of urea in a teflon lined hydrothermal vessel which was kept in an oven at $90^0 C$ for different time durations t of 6, 12, 18 and 24 h to obtain TNA/ZnO heterostructures. After hydrothermal treatment the samples were washed thoroughly with distilled water and further calcined at $350^0 C$. Pure TNA was also subjected to hydrothermal treatment under identical conditions for comparison.
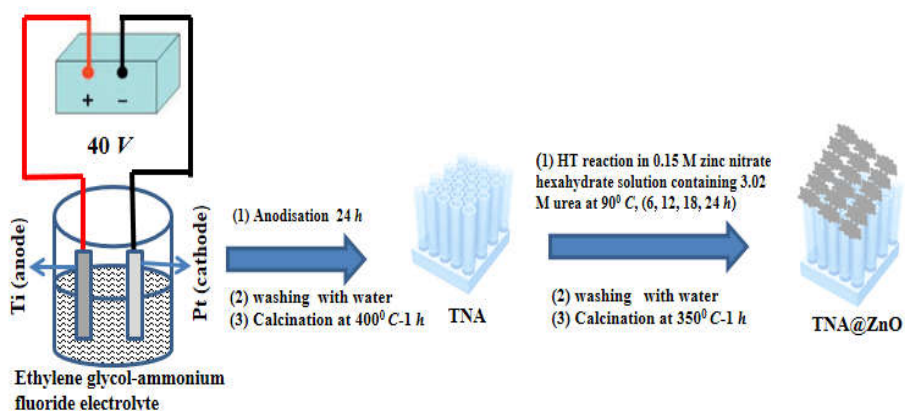
Fig. 3.2: Schematic diagram of fabrication of TNA@ZnO heterostructure.

The Raman spectra of the samples were recorded using a Raman Spectrometer (DXR, Thermo Scientific, USA, 532 *nm* laser excitation). Crystalline phase of the heterostructures were studied using an X-ray diffractometer (XRD, D5005, Bruker, Germany). Surface morphology and elemental analysis of the composites were determined by a scanning electron microscope (SEM) interfaced with an EDAX system (SU6600, Hitachi, Japan). UV-Visible absorption spectra were recorded on a UV-Vis spectrometer (Lambda 35, Perkin Elmer, USA). The heterostructures were carefully dislodged from the Ti metal foil and surface area were analysed by BET surface area analyser (Quadrasorb Evo, Model - 3QDS-MP-30, Quantachrome instruments, USA).

The photocatalytic activity of the prepared heterostructures was determined from the degradation of methylene blue (MB) dye in aqueous solution. In a typical experiment TNA/ZnO film having an

137

area of 1.0 cm^2 was placed in a cuvette containing MB dye solution of concentration 8.5 mg/L. The above cuvette was kept in the dark for 1 hour to acquire adsorption-desorption equilibrium of dye over the film. The dye solution containing the film was subsequently illuminated by UV light source containing 6 numbers of 15 W UV lamps (Philips UV light, G15 T8, Holland). The degradation was monitored at different time intervals, by determining the concentration of the MB dye at regular intervals using a UV visible spectrometer. The reference MB dye solution having the same concentration without the catalyst did not show any degradation under identical illumination conditions.

3.3 Results and Discussion

Formation of TNA/ZnO heterostructures is confirmed by their XRD pattern and Raman spectra (Fig. 3.3). Titania nanotubes are found to crystallise in the anatase phase as observed in the XRD pattern (Fig. 3.3A, a). In TNA/ZnO heterostructures (Fig. 3.3A, b-e) in addition to anatase phase of TiO_2, peaks corresponding to ZnO hexagonal wurtzite phase are also observed.

Raman spectra of the synthesized TNA and TNA/ZnO heterostructures are shown in Figure 3.3B. The different vibrational modes corresponding to anatase phase of TiO_2 are observed at 144, 394, 513 and 636 cm^{-1} in pure titania nanotube sample. Peaks corresponding to anatase as well as the E_2 vibrational mode of ZnO at 434 cm^{-1} [28] confirm the formation of TiO_2/ZnO heterostructure in TNA subjected to different hydrothermal treatments (Fig. 3.3B, b-e). The intensity of

Raman peak corresponding to ZnO is maximum for the sample which was hydrothermally treated for 12 *h*. (Fig. 3.3B, c)
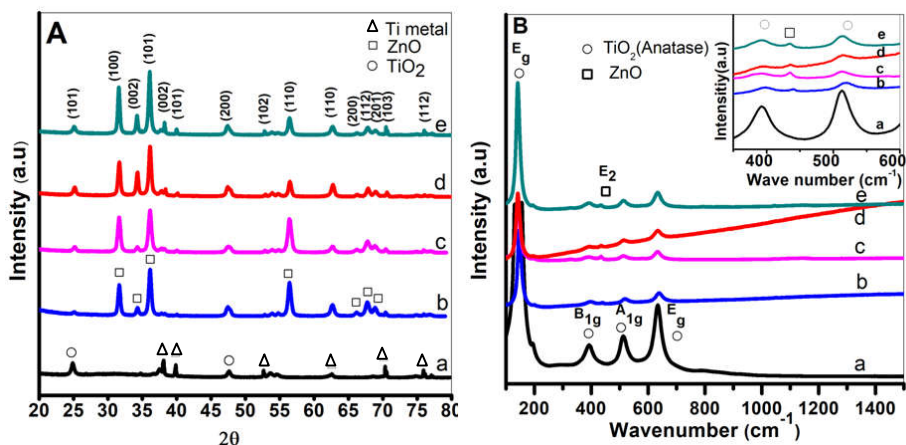
Fig. 3.3: A) XRD patterns and B) Raman spectra of the TNA/ZnO heterostructures a) Pure TNA b) after 6 *h*; c) 12 *h*; d) 18 *h* and e) 24 *h* of hydrothermal treatment time. (Inset from 350 to 600 *cm^1*).

The UV-Vis absorption spectra (Fig. 3.4) of the TNA/ZnO samples subjected to different durations of hydrothermal reactions exhibit a slight red shift when compared with that of the pure TNA [29,30]. This is attributed to the interfacial coupling effect between ZnO and TiO_2 [31]. It is observed that among the heterostructures the red shift is maximum for the one obtained after 12 *h* hydrothermal treatment time (Fig. 3.4c). The red shift is decreased for the other heterostructures. From this observation we can conclude that maximum ZnO is deposited on the TNA which is hydrothermally treated for 12 *h*.
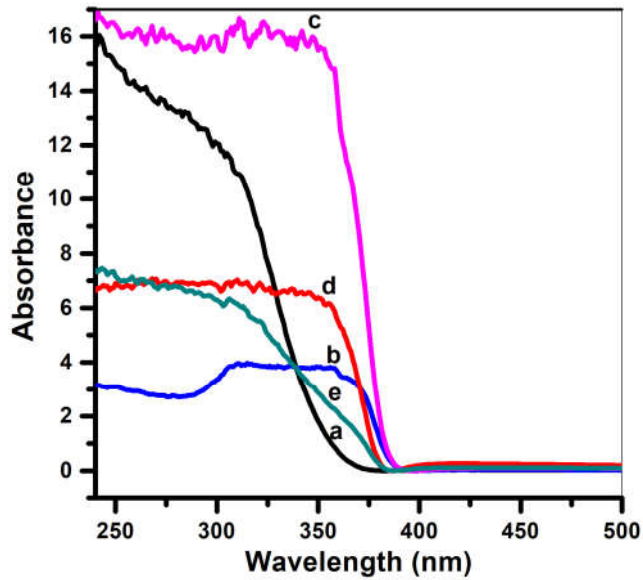
Fig. 3.4: Absorption spectra of TNA and TNA/ZnO heterostructures a) pure TNA, b) after 6 *h*; c) 12 *h*; d) 18 *h*; and e) after 24 *h* of hydrothermal treatment time.
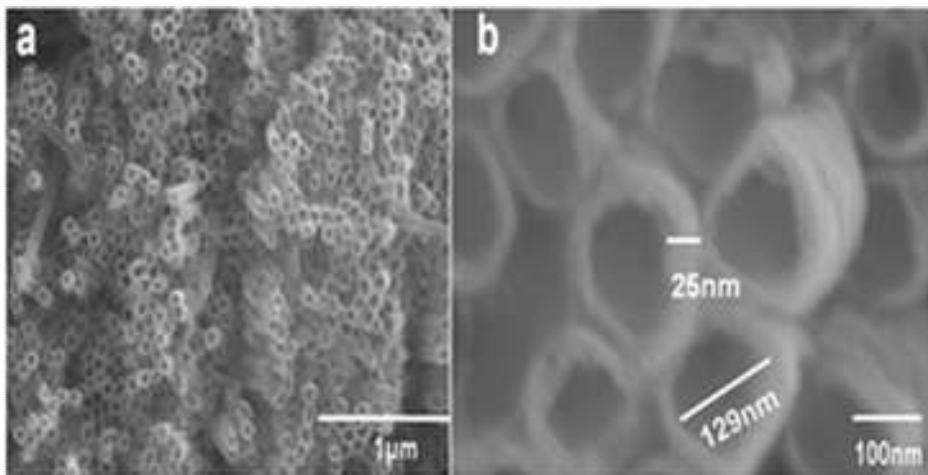
Fig. 3.5: SEM images of the surface of a) Titania nanotube arrays and b) magnified image of the same.

Figure 3.5a shows a typical SEM image of the surface of TNA, revealing well ordered and aligned titania nanotubes. Titania nanotubes have an average diameter of 129 nm, and wall thickness 25 nm as shown in Figure 3.5b. The surface morphology of the titania nanotube arrays after hydrothermal treatment for different time durations are shown in Figure 3.6. The morphological differences are clearly observed, from the SEM of the TNA/ZnO heterostructures. At a hydrothermal treatment time t of 6 h, it is observed that beautiful flower like zinc oxide particles are completely deposited on TNA (Fig. 3.6a). The morphology is similar to that reported earlier [32, 33]. When the hydrothermal treatment time t is increased to 12 h the morphology is flake like as shown in Figure. 3.6b. The EDAX results of the surface confirm the deposition of the zinc oxide particles (Table 3.1). For t greater than 12 h it is observed that the surface morphology is completely collapsed as shown in Figures 3.6c & d. This can be explained as follows. The morphology is highly dependent on the pH of the medium [32]. As the hydrothermal reaction time increases, the pH of the solution increases from 6.0 to 12.5. At $t = 12$ h the increase in pH to 9.5 leads to the delamination of the petals of the flower to yield flake-like structure (Fig. 3.6b). At pH > 9.5, the formed hydrous zinc oxide, being amphoteric in nature, dissolves in the medium to form ammonium zincate [34]. This causes depletion of ZnO from the surface leading to exposure of islands of the TNA to the surface (Figs. 3.6c & d). The EDAX results confirm the presence of TNA on the surface of heterostructure obtained after 24 h of hydrothermal treatment (Table 3.1)

Table 3.1. Composition analysis by EDAX at points B and D marked in Figs 3.6b & d.

Element	At B (Fig 4b)	At D (Fig 4d)
Zn	82.57	47.20
O	17.43	12.88
Ti	0	39.92
Total	100	100
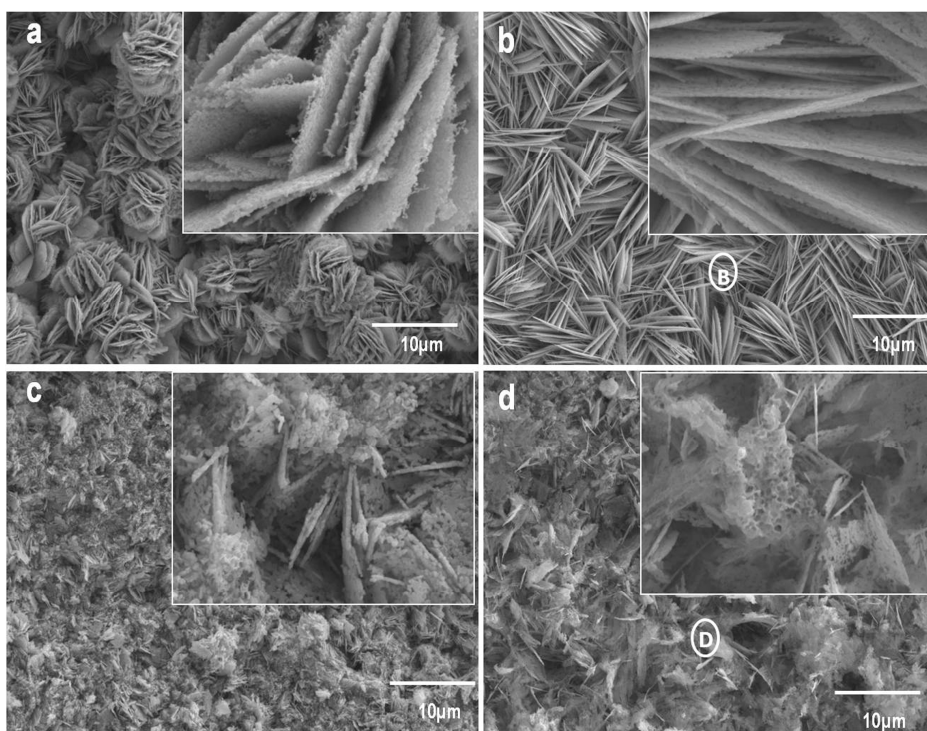
Fig. 3.6: SEM image of the TNA/ZnO heterostructures after a) 6 *h*; b) 12 *h*; c) 18 *h*; and d) 24 *h* hydrothermal treatment time (Inset shows the magnified image of the same).
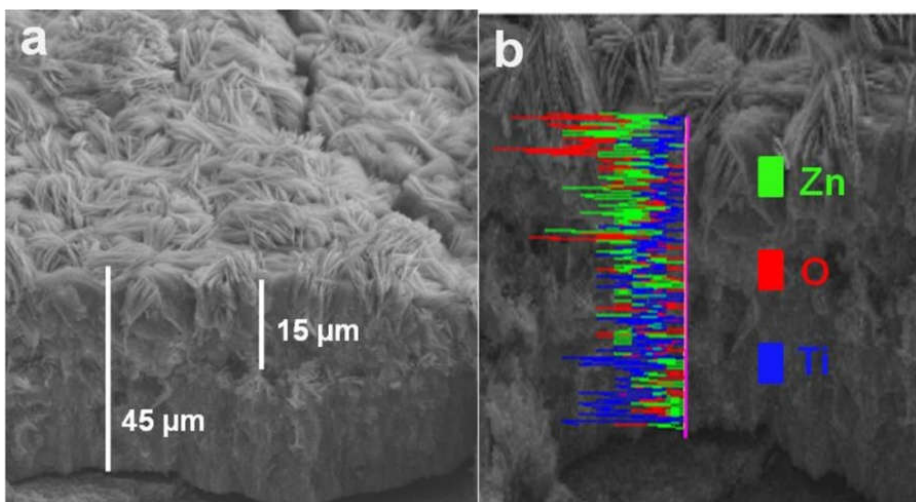
Fig. 3.7: a) Cross sectional image and b) line EDAX of the heterojunction of a typical TNA/ZnO heterostructure (Fluorescent green colour represents Zn in the line EDAX).

It is also observed from the cross sectional elemental analysis of a typical heterostructure (Fig 3.7b), that the ZnO layer deposited on TNA have thickness of $15 \mu m$, below which only TiO_2 are observed (Figs. 3.7a & b). Figures 3.8a & b show the SEM images of TNA subjected to hydrothermal treatment for 18 and 24 h without zinc salt and in the presence of only urea. It is clearly observed that hydrothermal treatments for such long durations under high pH conditions lead to degradation of surface texture as well as the ordered alignment of nanotubes in the array.
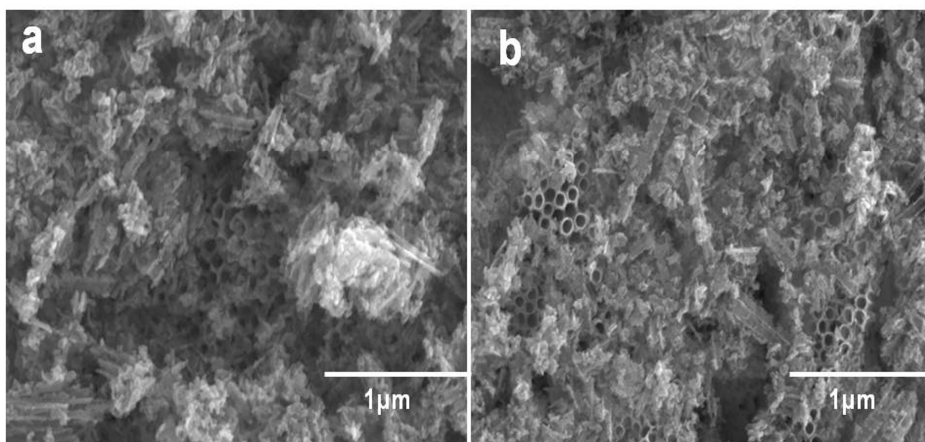
Fig. 3.8: SEM images of the surface of titania nanotube hydrothermally treated for a) 18 and b) 24 *h* respectively without zinc nitrate hexahydrate.

A typical UV-Vis spectra of MB degradation in presence of TNA/ZnO heterostructures is provided in Figure 3.9A, where it is observed that the concentration of the dye decreases in presence of photocatalyst under UV light illumination as a function of time. The decrease in concentration of MB (c/c_0) with respect to time under UV light illumination in presence of the TNA/ZnO heterostructures are shown in Figure 3.9B, where c is the concentration at the time 't' and c_0 is the initial concentration. The pseudo first order rate constant, k, of these samples calculated from the slope of plots of $-\ln(c/c_0)$ vs. time (t), are given in Table 3.2. It is seen that the TNA/ZnO, where $t = 12\ h$ exhibit the maximum photocatalytic activity.
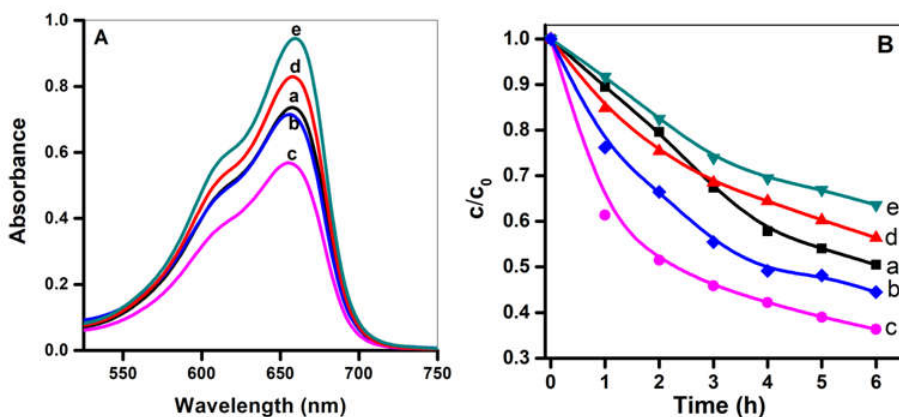
Fig. 3.9: A) UV-Vis spectra of MB dye after 6 *h* UV irradiation and B) Photocatalytic degradation curves of a) TNA and TNA/ZnO heterostructures after b) 6 *h*; c) 12 *h*; d) 18 *h*; and e) 24 *h* of hydrothermal treatment time.

The photocatalytic activities exhibited by TNA/ZnO are comparable with those reported for other TNA-ZnO heterostructures as given in Table 3.3.

Table 3.2. Rate constant *'k'* for MB degradation by TNA/ZnO heterostructures

Sl. No	TNA/ZnO-*t*	Rate constant, k (h^{-1})
1	$t = 0$ (Pure TNA)	0.122
2	$t = 6$ h	0.156
3	$t = 12$ h	0.202
4	$t = 18$ h	0.105
5	$t = 24$ h	0.083

145

Table 3.3. Comparison of photocatalytic activity with Titania – ZnO heterostructures

Nature of the catalyst	Concentration of dye / Area or amount of catalyst used for photo catalytic reaction	Intensity of Light Source.	Rate (K_{app}, $time^{-1}$)/ % degradation	Reference
ZnO nanorods embedded in TiO_2 nanotube arrays	Film of area 1 cm,^{2} 5 x 10^{-5} M of methyl orange solution with Na_2S as supporting electrolyte.	11 W UV lamp	39.6% ; 90 min.	Z. Zhang et al [23]
ZnO impregnated in between the TiO_2 nanotube arrays	Film of area 3cm^2 Rhodamine B (3ml) solution of concentration 5 mg/ L	300W Xe Arc lamp	~70.0%; 150 min.	F.X. Xiao [24]
TiO_2@ZnO n-p-n heterojunctions nanopowder.	10 mg of TiO_2@ZnO n-p-n heterojunctions nanopowder 20 mg/L (100ml) of methyl orange solution.	300 W UV lamps	0.27 min^{-1}.	L. Lin et al [30]
TiO_2/ZnO composite film	2.5 x 10^{-5} M methyl orange solution	20 W UV lamp	0.53 h^{-1}	J.Tian et al [35]
Thick film of TiO_2 / ZnO on Fluorine doped tinoxide surface.	Methylene blue solution (3ml) of concentration 1 x 10^{-5} M.	100 W high-pressure mercury lamp	1.37 min^{-1}.	D. Chen et al [36]
ZnO/TNA film heterostructures.	Film of area 1cm^2; methylene blue solution (4ml) of concentration 8.5 mg/L	6 numbers of 15 W UV lamps	58.0%; 180 min. (k= 0.202 h^{-1})	Present study

The enhanced photocatalytic activity of the TNA/ZnO heterostructures obtained after 6 *h* and 12 *h* of hydrothermal treatment time is attributed to more effective charge separation at the heterojunctions when compared with that of the pure TNA as shown Figure 3.10. The heterogeneous nanostructure of TNA@ZnO prevents the electron-hole recombination, and hence increase the life time of active species like electrons and holes. Thus increases the photocatalytic activity of heterostructures obtained at 6 and 12 *h* of hydrothermal treatment time.
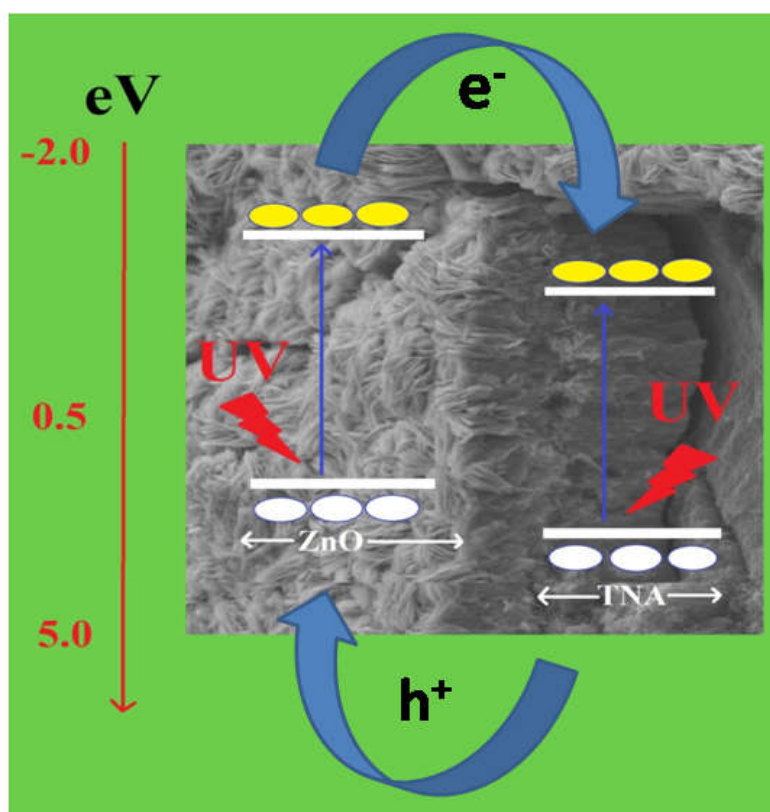
Fig. 3.10: Schematic representation of TNA@ZnO heterostructure.

However the surface morphology of the semiconductor also have an important role in its photocatalytic activity [37-39]. Di. Li et al studied

the photocatlytic activity of ZnO having different morphology and concluded that the crystal phases or ratios of the exposed crystal phases can change acording to the morphology of the material. Morphology can also influence the surface area of the material. Both the surface area and exposed crystal phase can directly alter the photocatlytic activity of the material [37]. The morphological influence on the surface area and hence the photocatlytic activity was also studied by C. W. Tang. The author prepared rod-like, granular-like and rice like ZnO nanostructures and studied the photocatlytic activity in UV light. Among these, ZnO nanoparticles having granular structure exhibited higher phototocatlytic activity than other nanostructures due to its incresed surface area and the altered band-gap. Our study again proves the fact that surface morphology has a crucial role in determining the photocatlytic activity. From the SEM image (Fig. 3.6b inset) it is seen that the effective surface area is increased due to the delamination of the petals of the flowers. This mechanism is in confirmation with the results obtained from BET analysis, showing an increase in surface area from 34 m^2g^{-1} to 39 m^2g^{-1}. This increase in surface area along with a more textured surface lead to their higher photocatalytic activity when compared with that where the morphology is flower like. In the case of hydrothermal reactions for durations beyond 12 h, the decrease in the photocatalytic activity is attributed to the degradation of the surface structure as well as the alignment of the TNAs as described earlier (Figs. 3.8a & b).

3.4 Conclusions

Well-ordered TiO_2 nanotube array were fabricated by anodisation of titanium foil. TNA films exhibited anatase crystalline phase. ZnO nanoparticles were deposited on TNA by hydrothermal treatment to form TNA/ZnO heterostructures. The influence of hydrothermal treatment time on the growth of ZnO on TNA and surface morphology were studied. It is found that the photocatalytic properties of the TNA/ZnO heterostructures are higher than that of unmodified TNA and are highly dependent on their surface morphology and texture. Highest photocatalytic activity was obtained for the TNA/ZnO heterostructure where the surface layers were composed of delaminated petals from ZnO nanoflowers.

References

[1]   S. Ameen, M. S. Akhtar, H. K. Seo, H. S. Shin, in: A. Tiwari and S. Valyukh (Eds.), Advanced Energy Materials, Wiley publications, New-Jersey, America, 2014, pp. 105-157.

[2]   D.M. Fouad, M. B. Mohamed, Comparative Study of the Photocatalytic Activity of   Semiconductor Nanostructures and Their Hybrid Metal Nanocomposites on the Photodegradation of Malathion, J. Nanomater. 2012 (2011) Article ID 524123.

[3]   K. Vinodgopal, I. Bedja, P.V. Kamat, Nanostructured Semiconductor Films for Photocatalysis. Photoelectrochemical Behavior of SnO_2/TiO_2 Composite Systems and Its Role in Photocatalytic Degradation of a Textile Azo Dye, Chem. Mater. 8 (1996) 2180-2187.

[4]   S. S. Shinde, C. H. Bhosale, K. Y. Rajpure, Solar light assisted photocatalysis of water using a zinc oxide semiconductor, J. Semicond. 34 (2013) 1-4.

[5]   C. A. K. Gouvea, F. Wypych, S. G. Moraes, N. Duran, N. Nagata, P. P. Zamora, Semiconductor-assisted photocatalytic degradation of reactive dyes in aqueous solution, Chemosphere, 40 (2000) 433-440.

[6]   C. Hariharan, Photocatalytic degradation of organic contaminants in water by ZnO nanoparticles: Revisited, Appl. Catal. A. 304 (2006) 55-61.

[7]   D. Gong, C. A. Grimes, O. K. Varghese, W. C. Hu, R. S. Singh, Z. Chen, E. C. Dickey, Titanium oxide nanotube arrays prepared by anodic oxidation J. Mater. Res. 16 (2001) 3331-3334.

[8]   O. K. Varghese, D. Gong, M. Paulose, K. G. Ong, C. A. Grimes, Hydrogen sensing using titania nanotubes, Sens. Actuators B, 93 (2003) 338-344.

[9]   C. A. Grimes, Synthesis and application of highly ordered arrays of TiO_2 nanotubes, J. Mater. Chem. 17 (2007) 1451-1457.

[10] K. Zhu, N. R. Neale, A. Miedaner, A. J. Frank, Enhanced Charge-Collection Efficiencies and Light Scattering in Dye-Sensitized Solar Cells Using Oriented TiO_2 Nanotubes Arrays, Nano Lett. 7 (2007) 69-74.

[11] L. Dong, G. X. Cao, Y. Ma., X. L. Jia, G. T. Ye, S. K. Guan, Enhanced photocatalytic degradation properties of nitrogen-doped titania nanotube arrays, Trans. Nonferrous Met. Soc.China, 19 (2009) 1583-1587.

[12] J. H. Park, S. Kim, A. J. Bard, Novel Carbon-Doped TiO_2 Nanotube Arrays with High Aspect Ratios for Efficient Solar Water Splitting, Nano Lett. 6 (2006) 24-28.

[13] N. Lu, X. Quan, J. Y. Li, S. Chen, H. T. Yu, G. H. Chen, Fabrication of Boron-Doped TiO_2 Nanotube Array Electrode and Investigation of Its Photoelectrochemical Capability, J. Phys. Chem. 111 (2007) 11836-11842.

[14] L. Sun, J. Li, C. L. Wang, S. F. Li, H. B. Chen, C. J. Lin, An electrochemical strategy of doping Fe^{3+} into TiO_2 nanotube array films for enhancement in photocatalytic activity, Sol. Energy Mater. Sol.Cells. 93 (2009) 1875-1880.

[15] D. Lu, M. Zhang, Z. Zhang, Q. Li, X. Wang, J. Yang, Self-organized vanadium and nitrogen co-doped titania nanotube arrays with enhanced photocatalytic reduction of CO_2 into CH_4, Nanoscale Res. Lett. 9 (2014) 272.

[16] J. Yu, J. Xiong, B. Cheng, S. Liu, Fabrication and characterization of Ag–TiO_2 multiphase nanocomposite thin films with enhanced photocatalytic activity, Appl. Catal. B, 60 (2005) 211-221.

[17] Q. Kang, S. Liu, L. Yang, Q. Cai, C. A. Grimes, Fabrication of PbS Nanoparticle-Sensitized TiO_2 Nanotube Arrays and Their Photoelectrochemical Properties, Appl. Mater. Interfaces. 3 (2011) 746-749.

[18] X. F. Gao, W. T. Sun, Z. D Hu, G. Ai, Y. L. Zhang, S. Feng, F. Li, L. M. Peng, An Efficient Method To Form Heterojunction CdS/TiO_2 Photoelectrodes Using Highly Ordered TiO_2

Nanotube Array Films, J. Phys. Chem. C.113 (2009) 20481-20485.

[19]   A. I. Kontos, V. Likodimos, T. Stergiopoulos, D.S. Tsoukleris, P. Falaras, I. Rabias, G. Papavassiliou, D. Kim, J. Kunze, P. Schmuki, Self-Organized Anodic TiO_2 Nanotube Arrays Functionalized by Iron Oxide Nanoparticles, Chem. Mater. 21 (2009) 662-672.

[20]   Y. Shen, F. Li, D. Liu, S. Li, L. Fan, Fabrication of TiO_2 Nanotube Films Modified with Ag_2S and Photoelectrocatalytic Decolorization of Methyl Orange Under Solar Light, Sci. Adv. Mater. 4 (2012) 1214-1219.

[21]   S. Benkara, S. Zerkout, Preparation and characterization of ZnO nanorods grown into aligned TiO_2 nanotube array, J. Mater. Environ. Sci. 3 (2010) 173-188.

[22]   Y. Lei, G. Zhao, M. Liu, Z. Zhang, X. Tong, T. Cao, Fabrication, Characterization, and Photoelectrocatalytic Application of ZnO Nanorods Grafted on Vertically Aligned TiO_2 Nanotubes, J. Phys. Chem. C. 113 (2009) 19067- 19076.

[23]   Z. Zhang, Y. Yuan, L. Liang, Y. Cheng, G. Shi, L. Jin, Preparation and photoelectrocatalytic activity of ZnO nanorods embedded in highly ordered TiO_2 nanotube arrays electrode for azo dye degradation, J. Hazard. Mater. 158 (2008) 517-522.

[24]   F. X. Xiao, Construction of Highly Ordered ZnO–TiO_2 Nanotube Arrays (ZnO/TNTs) Heterostructure for Photocatalytic Application, Appl. Mater. Interfaces. 4 (2012) 7055-7063.

[25]   R. Li, Z. Xie, H. Lu, D.W. Zang, A.Yu, Fabrication of ZnO@TiO_2 Core-Shell Nanotube Arrays as Three-Dimensional Anode Material for Lithium Ion Batteries, Int. J. Electrochem. Sci. 8 (2013) 11118-11124.

[26]   X. Qu, F. Du, Organized Arrays of TiO_2/ZnO Nanotube Coaxial Core–Shell Heterojunctions for Photocatalytic Applications, Sci. Adv. Mater. 7 (2015) 337-344.

[27]   N. K. Allam, C. A. Grimes, Room Temperature One-Step Polyol Synthesis of Anatase TiO_2 Nanotube Arrays: Photoelectrochemical Properties, Langmuir 25 (2009) 7234-7240.

[28]   J. Z. Marinho, F. C. Romeiro, S. C. S. Lemos, F. V. Motta, C. S. Riccardi, M. S. Li, E. Longo, R. C. Lima, Urea-Based Synthesis of Zinc Oxide Nanostructures at Low Temperature, J. Nanomater. 2012 (2012), Article ID 427172.

[29]   X. Wang, Z. Wu, Y. Wang, W. Wang, X. Wang, Y. Bu, J. Zhao, Adsorption–photodegradation of humic acid in water by using ZnO coupled TiO_2/bamboo charcoal under visible light irradiation , J. Hazard. Mater. 262 (2013) 16-24.

[30]   L. Lin, Y. Yang, L. Men, X. Wang, D. He, Y. Chai, B. Zhao, S. Ghoshroy, Q. Tang, A highly efficient TiO_2@ZnO n–p–n heterojunction nanorod photocatalyst, Nanoscale. 5 (2013) 588-593.

[31]   Y. Zhao, C. Li, X. Liu, F. Gu, H. L. Du, L. Shi, Zn-doped TiO_2 nanoparticles with high photocatalytic activity synthesized by hydrogen–oxygen diffusion flame, Appl. Catal. B. 79 (2008) 208-215.

[32]   R. Wahab, Y. S. Kim, H. S. Shin, Synthesis, Characterization and Effect of pH Variation on Zinc Oxide Nanostructures, Mater. Trans. JIM. 50 (8) (2009) 2092-2097.

[33]   M. S. Mohajerani, A. Lak, A. Simchi, Effect of morphology on the solar photocatalytic behavior of ZnO nanostructures, J. Alloys Compd. 485 (2009) 616-620.

[34]   A. Kumar De, A Text book of inorganic chemistry, 9th Ed. New Age International publishers, India, 2003.

[35]   J. Tian, L. Chen, Y. Yin, X. Wang, J. Dai, Z. Zhu, X. Liu, P. Wu, Photocatalyst of TiO_2/ZnO nano composite film: Preparation, characterization, and photodegradation activity of methyl orange Surf. Coat. Tech. 204 (2009) 205-214.

[36] D. Chen, H. Zhang, S. Hu, J. Li, Preparation and Enhanced Photoelectrochemical Performance of Coupled Bicomponent ZnO−TiO$_2$ Nanocomposites, J. Phys. Chem. C. 112 (2008) 117-122.

[37] Di. Li, H. Haneda, Morphologies of zinc oxide particles and their effects on photocatalysis Chemosphere. 51 (2003) 129-137.

[38] C. W. Tang, Study of photocatalytic degradation of methyl orange on different morphologies of ZnO catalysts, Mod. Res. Catal. 2 (2013) 19-24.

[39] L. Liu, H. Liu,Y. P. Zhao, Y. Wang ,Y. Duan, G. Gao, M. Ge, W. Chen, Environ. Sci. Technol. 42 (2008) 2342-2348.

CHAPTER 4
SnO$_2$-loaded BaTiO$_3$ nanotube arrays: Fabrication and visible-light photocatalytic applications

CONTENTS

4.1 Introduction

Ferroelectric oxides with the ABO_3 type perovskite structure like Barium titanate ($BaTiO_3$), due to their higher chemical stability and polar nature are emerging as potential candidates for enhanced photocatalytic and solar cell applications [1, 2]. Y. Cui et al studied in detail the advantage of ferroelectric material for photocatalytic application [3]. Ferroelectric materials have the property of spontaneous polarization. Displacement of center of negative and positive charges in the unit cell results in spontaneous polarization and the polarization creates macroscopic charges on the surface of ferroelectric material. This charge is compensated by defects and free charge carriers in the material or this charge can be externally compensated by the adsorbed charged molecule from the surroundings. If the spontaneous polarization is directing from the bulk to the surface, it will create a positive charge (C^+) on the surface and if it is from surface to bulk, it creates a negative charge(C^-) in the surface. The internal depolarization field will lead to accumulation of electrons near the C^+ surface resulting in downward band bending. In the (C^-) region, due to accumulation of holes, upward band bending takes place. Thus the band bending due to ferroelectricity lead to the separation of charge carriers, which helps to prevent the recombination of electrons and holes. Ferroelectricity also helps to bind the dye molecule on material surfaces tightly [3-5]. Y. Cui et al also prepared Ag doped $BaTiO_3$ and compared the photocatalytic activity with other samples and observed an increased photocatalytic rate for Ag doped $BaTiO_3$ than that of ferroelectric and non ferroelectric $BaTiO_3$ (having cubic structure owing to particle size < 20 *nm*). In Ag doped $BaTiO_3$, both the ferroelectricity and

heterogeneous structure prevents the electron-hole recombination, which promote the photocatalytic activity of the material (Fig. 4.1).
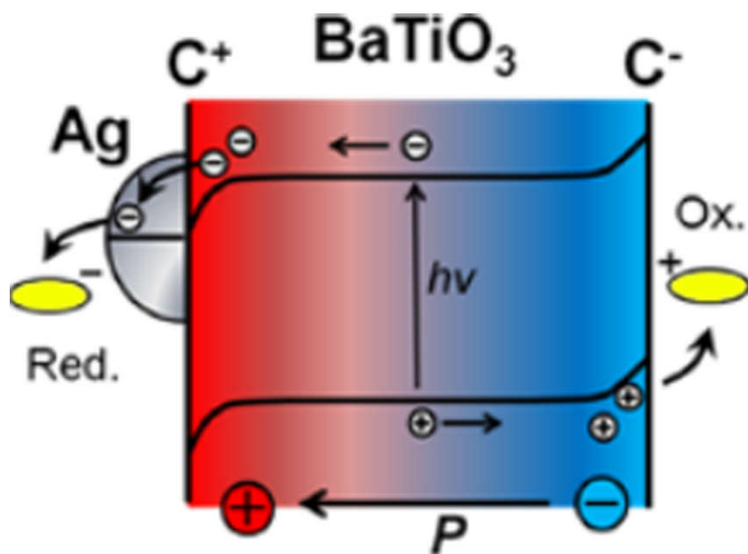
Fig. 4.1: Schematic representation of Ag@BaTiO3 heterostructure.

[Source: Y. Cui et al, Effect of Ferroelectricity on Solar-Light-Driven Photocatalytic Activity of BaTiO₃-Influence on the Carrier Separation and Stern Layer Formation, Chem. Mater. 25 (2013) 4215−4223]

These studies help us to understand the importance of ferroelectric materials as a photocatalyst. However the wide band-gap of ferroelectrics restricts their applications. It is therefore necessary to engineer their band-gap to extend their photo absorption wave lengths to visible region. Band-gap engineering strategies in ferroelectric oxides like $BaTiO_3$ include substitution of Ti^{4+} at the B-site with elements like Ni^{2+}, Pt^{2+} etc [6, 7] as well as fabrication of heterogeneous nanostructures consisting of two components for enhanced visible light absorption [8, 9]. For such applications, it is desirable to fabricate well-ordered nanotube arrays aligned

perpendicular to the substrate surface as this configuration allows for facile surface modification with suitable nanoparticles for fabricating novel heterostructures [10-15]. Although there are reports on the fabrication of well-ordered $BaTiO_3$ nanotube arrays (BTNTAs) [16-19], application of their heterogeneous nanostructures in photocatalysis have not yet been studied in detail. Tin oxide is one of the most important intrinsic n-type semiconductors with a wide band-gap of 3.5 eV. Since tin exists in both +2 and +4 valence states, decorating BTNTAs with nanoparticles of oxide of tin can lead to enhanced photocatalytic activity due to their favorable redox chemistry. This has not yet been reported. Therefore, in this study we report the fabrication of SnO_2-loaded $BaTiO_3$ nanotube arrays, in which SnO_2 nanoparticles having different morphologies have been deposited on BTNTAs by hydrothermal method and correlate their defect chemistry and surface morphology with the visible-light photocatalytic activity. Reaction temperature, pH and use of surfactants are some of the important parameters that control the morphology of many oxides during their synthesis [20-23]. M. Ramezani et al studied the effect of surfactants like PVA (poly vinyl alcohol), CTAB (cetyl trimethyl ammonium bromide), SDS (sodium dodecyl sulphate), PVP (poly vinyl pyrrolidone) and chelating agent like salicylic acid on the morphology of $Na_{1/2}Bi_{1/2}Cu_3Ti_4O_{12}$. The authors reported that surfactant and chelating agent used for the preparation of nanoparticle has a vital role in deciding the morphology of nanomaterial [20]. The influence of natural capping agents like glucose, fructose, galactose, lactose and starch on the morphology of europium titanate ($Eu_2Ti_2O_7$) was investigated by A. S. Nasab et al and found that the natural capping agents can also change the morphology of the material [22]. M. S. Niasari et al prepared zinc titanate ($ZnTiO_3$) through sol-gel method

and co-related the morphology of $ZnTiO_3$ with the calcination temperature and pH of the precursor solution. The authors observed that the Particle size increases as the temperature increases, whereas the particle size decreases as the pH of the medium increases and they concluded that the calcination temperature and the pH of the medium have strong influence on particle size and morphology of the material [23]. In this study we have fabricated morphologically different nanostructures of SnO_2@BTNTAs by changing the pH of the medium during synthesis.

4.2 Experimental

Titania nanotubes were synthesized by anodisation of titanium sheet in a two electrode cell with titanium sheet as working electrode and Pt as counter electrode in an ethylene glycol-fluoride electrolyte at 40 V for 24 h followed by washing with distilled water and drying at room temperature. The prepared Titania nanotubes were then immersed in a solution of 0.05 M barium hydroxide monohydrate in teflon- lined hydrothermal vessel and kept in an oven at 180^0 C for 2 h to obtain BTNTAs. After hydrothermal treatment the samples were washed thoroughly with distilled water and dried at room temperature. Thus obtained BTNTAs were then kept in an 80 ml solution of 0.15 M tin (II) chloride dihydrate containing 0.6 M of urea in a 100 ml teflon-lined hydrothermal vessel. The pH of the solution was adjusted to 8, 10, and 12 by the addition of different volumes of 6 M NaOH. Then the hydrothermal vessel was kept in an oven at 180^0 C for 18 h. After hydrothermal treatment the samples were washed thoroughly with distilled water and dried at room temperature to obtain SnO_2@BTNTAs. The schematic preparation of SnO_2@BTNTAs is shown in Figure 4.2.
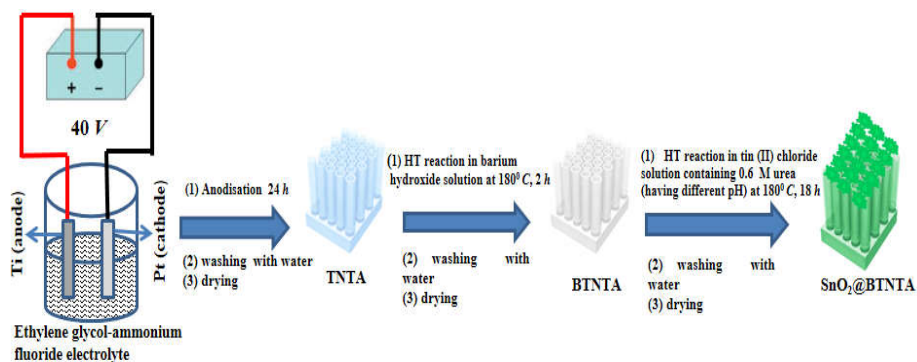
Fig. 4.2: Schematic representation of procedure of SnO₂@BTNTAs preparation.

The Raman spectra of the heterostructures were recorded using a Raman spectrometer [DXR, Thermo Scientific, USA]. Crystalline phase were determined using an X-ray diffractometer [D5005, Bruker, Germany]. Surface morphology of the heterostructures was determined by a scanning electron microscope [Nova Nano SEM 450, FEI, USA]. Absorption and diffused reflectance spectra were obtained using a UV-Visible spectrophotometer [V-550, Jasco, Japan]. X-ray Photoelectron Spectroscopy was carried out on an X-ray Photoelectron Spectrometer [Axis-Ultra, Kratos Analytical, UK]. The photocatalytic activity of the prepared samples was determined from the degradation of methylene blue (MB) dye in aqueous solution. In a typical experiment,SnO₂@BTNTAs film having an area of 1.0 cm^2 was placed in a cuvette containing MB dye solution of concentration 8.5 mg/L. The above cuvette was kept in the dark for 1 h to acquire adsorption-desorption equilibrium of dye over the film. The dye solution containing the film was subsequently illuminated by a visible light source of a 300 W Tungsten lamp (Immersion type photo reactor HEBER, India). The degradation was monitored at different time intervals, by determining the concentration of the MB dye at regular

intervals using a UV-Vis spectrometer. The reference MB dye solution having the same concentration without the catalyst did not show any degradation under identical illumination conditions.

4.3   Results and discussion

It is seen from the XRD pattern (Fig. 4.3A, a) that barium titanate nanotubes crystallise in cubic structure. In SnO_2@BTNTAs, in addition to cubic $BaTiO_3$, peaks corresponding to SnO_2 tetragonal rutile structure are also observed. The intensities of (110) and (101) peaks corresponding to SnO_2 are maximum for the sample obtained at pH= 12 during hydrothermal synthesis (Fig. 4.3A, d).
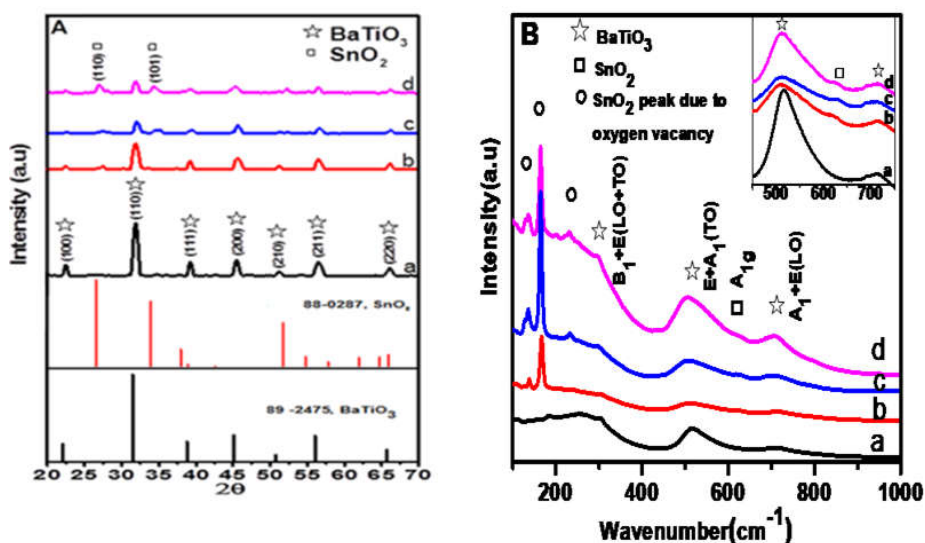
Fig. 4.3: A) XRD patterns and B) Raman Spectra of (a) Pure BTNTAs and SnO₂@BTNTAs obtained at pH values (b) 8; (c) 10; and (d) 12 (inset shows magnified image of the region from 450cm⁻¹ to 750cm⁻¹).

Raman spectra of BTNTAs and SnO_2@BTNTAs are shown in Figure 4.3B. The different vibrational modes of BTNTAs are observed at 261, 306, 517, 718 *cm⁻¹* in pure barium titanate nanotube array. Peaks

corresponding to BaTiO$_3$ as well as the vibrational modes of SnO$_2$ at 628 cm^{-1} suggest the formation of SnO$_2$@BTNTAs (Fig. 4.3B, b-d). The peaks observed at 160, 170 and 230 cm^{-1} represents oxygen vacancies [24-26].
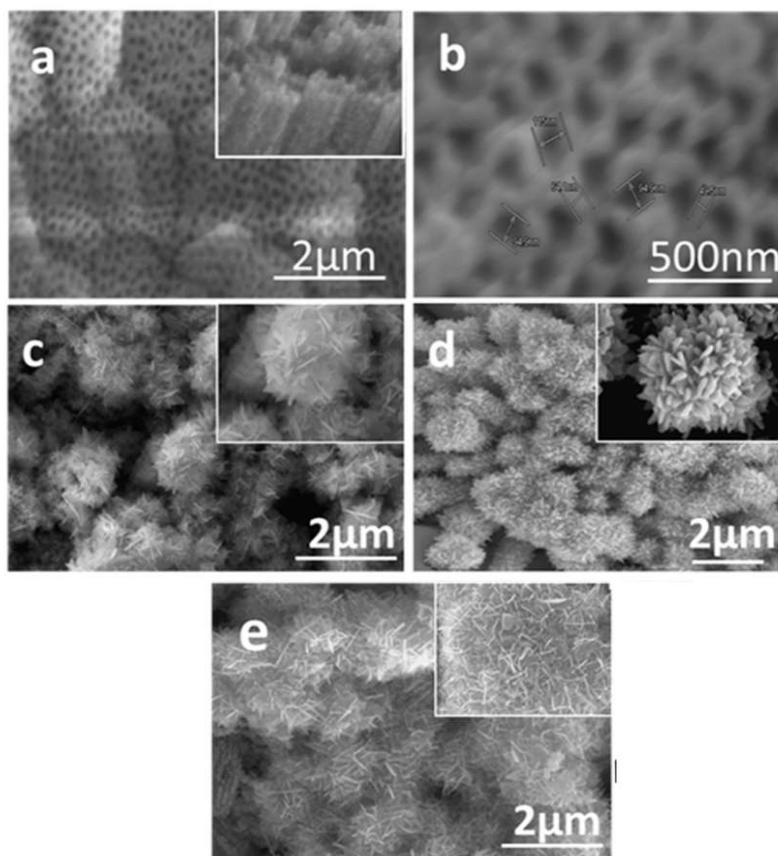
Fig. 4.4: SEM images of the surface of (a) barium titanate nanotube arrays (inset shows cross-sectional view) (b) magnified image of the same and SnO$_2$ @BTNTAs samples obtained at pH values (c) 8; (d) 10; (e) 12 (*insets show the magnified images of the same*).

Figure 4.4a shows a typical SEM image of the surface of BTNTAs, revealing well-ordered and aligned barium titanate nanotubes. Barium titanate nanotubes in the array have an average diameter of 95 *nm* and

wall thickness of 60 *nm* as shown in Figure 4.4b. The surface morphology of the SnO$_2$@BTNTAs obtained at different pH is shown in Figures 4.4(c-e). The morphological differences at the surface are clearly observed for the SnO$_2$ loaded BTNTAs samples. At a pH of 8 and 10 during hydrothermal synthesis, beautiful flower-like particles of SnO$_2$ are deposited on the surface of BTNTAs (Figs. 4.4c and d). For pH = 12, the morphology of the tin oxide particles changed to flake-like as shown in Figure 4.4e. As the pH of the solution increases it is also observed that more and more SnO$_2$ particles are deposited on the surface of BTNTAs.
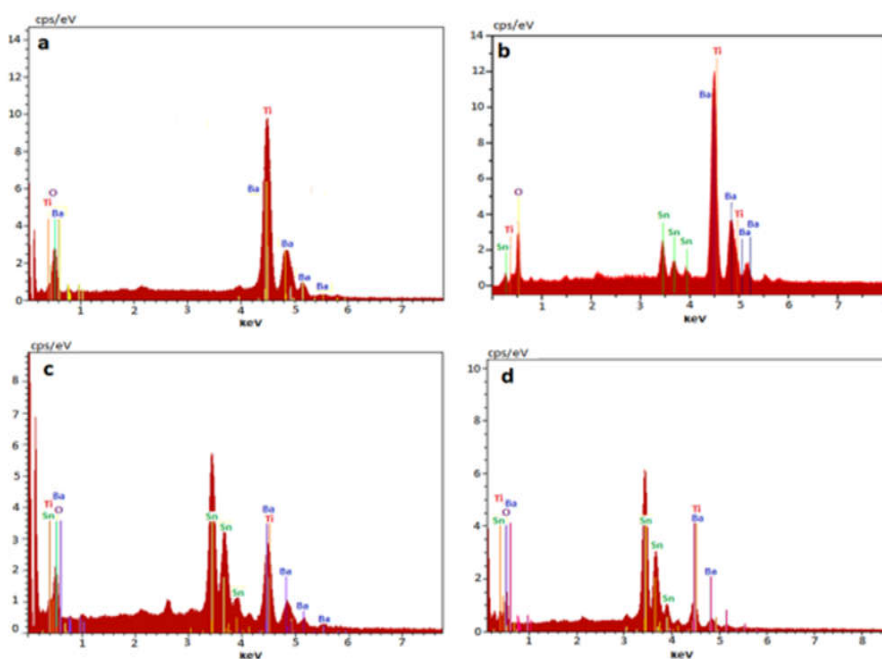
Fig. 4.5: EDX patterns of a) BTNTAs and SnO$_2$@BTNTAs obtained atpH values b) 8; c) 10; and d) 12.

Chemical composition and purity of the heterostructures were analysed by EDX. The EDX spectra obtained for BTNTAs and other

heterostructures are provided in Figure 4.5. It is observed that for pure BTNTA only Ba, Ti and O are present whereas for the heterogeneous structures in addition to Ba, Ti, and O, Sn is also present and the amount of Sn increases as the pH of the medium increases. No other elements are observed in all the samples.

The absorption spectra of pure BTNTAs and SnO_2@BTNTAs are shown in Figure 4.6. It can be clearly observed that in the case of SnO_2 loaded BTNTAs the absorption extends to the visible range when compared with that of pure BTNTAs. The SnO_2@BTNTAs obtained at a pH= 12, which has an intense green color, exhibits the highest red shift (Fig. 4.6d). For pure BTNTAs the band-gap energy is 3.2 eV whereas in the case of SnO_2@BTNTAs the band-gap energy decreases to 2.47 eV as shown in the Kubelka- Munk plot (inset of Fig. 4.6).
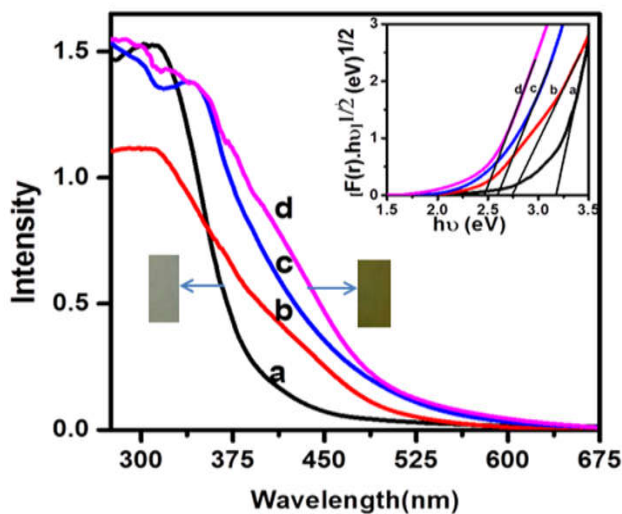
Fig. 4.6: Absorption spectra of (a) Pure BTNTAs and SnO₂@BTNTAs samples obtained at pH values (b) 8; (c) 10; (d) 12 and inset shows Kubelka-Munk plot of BTNTAs and SnO₂@BTNTAs samples.

This decrease in the band-gap energy can be explained as follows. Under the reaction conditions employed the oxidation of Sn^{2+} to Sn^{4+} with a concomitant reduction of Ti^{4+} to Ti^{3+} take place due to the favourable redox reactions as represented below in equations (4.1) and (4.2).

$$TiO^{2+} + 2H^+ + e^- \rightleftharpoons Ti^{3+} + H_2O: \text{E}^0 = 0.19 \text{ V} \quad \text{----} \quad (4.1)$$

$$SnO_2 + 4H^+ + 4e^- \rightleftharpoons SnO + 2H_2O: \text{E}^0 = -0.09\text{V} \quad \text{----} \quad (4.2)$$
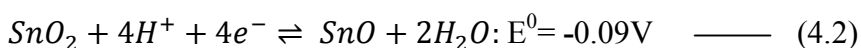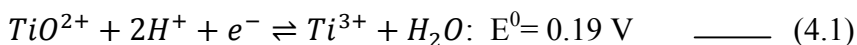
The reduction of Ti^{4+} to Ti^{3+} also leads to the creation of oxygen vacancies $(V_{\ddot{O}})$ as represented below in equation (4.3);

$$2Ti_{Ti}^x + 2e^- \rightarrow 2Ti_{Ti}^{'} + V_{\ddot{O}} \quad \text{----} \quad (4.3)$$

where $Ti_{Ti}^{'}$ represents a Ti^{3+} ion at the B-site with a negative charge and $V_{o}^{\cdot\cdot}$ represents doubly positively charged oxygen vacancy with respect to the neutral lattice in the perovskite structure according to Kröger-Vink notation. Direct evidence for the presence of Ti^{3+} and $V_{\ddot{O}}$ was obtained from the XPS measurements. In BTNTAs the Ti2p$_{3/2}$ and Ti2p$_{1/2}$ binding energies are 457.3 and 463.0 eV respectively (Fig. 4.7A, a) [27, 28]. The observed split of 5.7 eV between the two J states confirms the +4 valence state of Titanium. In the case of SnO$_2$@BTNTAs, the Ti2p$_{3/2}$ binding energy is negatively shifted to 456.4 eV (Fig. 4.7A, b), clearly indicating the presence of Ti^{3+} ions [29, 30]. The O1s peak at 530.6 eV due to the binding energy (BE) of oxygen in Ti^{4+}-O-Ti^{4+} (Fig. 4.7B, a) in BTNTAs, is negatively shifted to 529.2 eV in the SnO$_2$@BTNTAs (Fig. 4.7B, b) clearly indicating the change in the oxygen environment [31, 32]. The O1s peak observed at

528.5 *eV* in BTNTAs represents the Ba-O-Ti^{4+} lattice oxygen [33]. The peak observed at 531.8 *eV* is attributed to surface adsorbed hydroxyl ions [34].
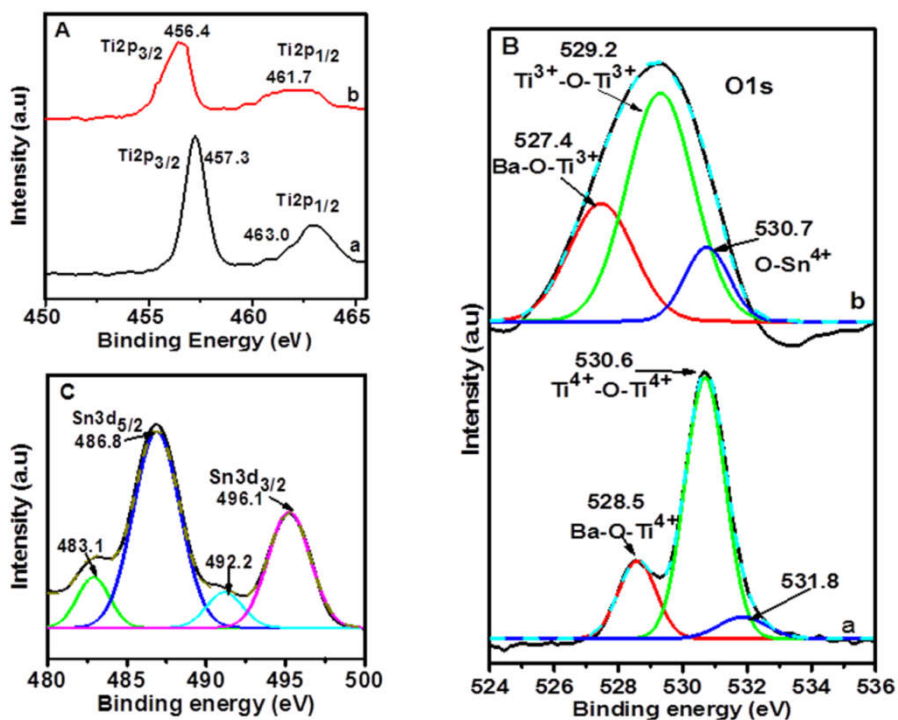
Fig. 4.7: XPS spectra of (A) Ti2p of (a) BTNTAs and (b) SnO$_2$@BTNTAs obtained at pH=12, (B) O1s of (a) BTNTAs and (b) SnO$_2$@BTNTAs obtained at pH=12, (C) Sn3d of SnO$_2$@BTNTAs obtained at pH=12.

The O1s peak of SnO$_2$@BTNTAs (Fig. 4.7B,b) is wide and asymmetric. On deconvolution, the components corresponding to Ba-O-Ti^{3+} (527.4 *eV*); Ti^{3+}-O-Ti^{3+} (529.2 *eV*); and Sn^{4+}-O (530.7 *eV*) are obtained. The peak observed at 527.4 *eV* in the SnO$_2$@BTNTAs corresponds to Ba-O-Ti^{3+} lattice oxygen. The negative shift of this peak from that observed in unloaded BTNTAs also shows the change

in the oxygen environment. For the SnO$_2$@BTNTAs, the O1s binding energy of 530.7eV corresponds to Sn^{4+}-O lattice oxygen [31, 32]. The Sn3d$_{5/2}$,Sn3d$_{3/2}$ peaks (Fig. 4.7C) corresponding to Sn^{4+}are intense and observed at 486.8 and 496.1 eV respectively whereas the corresponding peaks due to Sn^{2+}are weak and are observed at 483.1 and 492.2 eV [28,29]. The weak intensity of these peaks clearly provide evidence for the oxidation of Sn^{2+} to Sn^{4+}and the presence of SnO$_2$ on the surface of the BTNTAs [35, 36]

Oxygen vacancies form donor levels below the conduction band whereas Ti^{3+} form acceptor levels near the valence band leading to reduction in the band-gap as schematically shown in Figure 4.8. The presence of these defect levels within the band-gap in SnO$_2$@BTNTAs is responsible for the reduction in the band-gap [37-39].
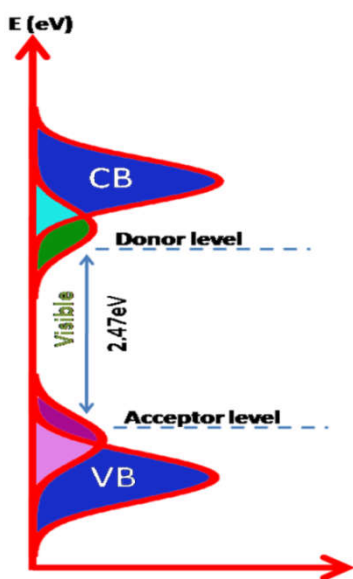
Fig.4.8: Energy band diagram of SnO$_2$@BTNTAs sample.

Typical absorption spectra of MB degradation in presence of BTNTAs and SnO$_2$@BTNTAs samples are shown in Figure 4.9A, where it is observed that concentration of dye decreases in presence of the photocatalyst under visible light illumination as a function of time. The decrease in concentration of MB (C/C_0) with respect to time under visible light illumination in presence of SnO$_2$@BTNTAs samples are plotted in Figure 4.9B, where C is the concentration at time 't' and C_0 is the initial concentration. The pseudo first order rate constant k, calculated from the slope of plots of $-\ln(C/C_0)$ vs time (t), are given in Table 4.1. It is seen that the SnO$_2$@BTNTAs obtained at pH=12 exhibit the maximum photocatalytic activity with a rate constant, $k = 0.558\ h^{-1}$.
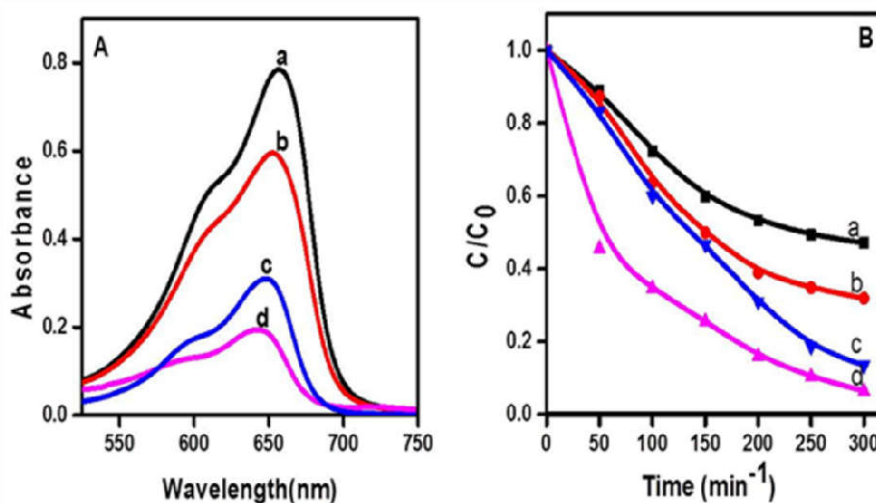
Fig. 4.9: (A) UV-Vis spectra of MB dye after 5 *h* Visible light irradiation and (B) Photocatalytic degradation curves of (a) BTNTAs and SnO$_2$@BTNTAs obtained at pH values (b) 8; (c) 10; (d) 12.

Table 4.1, Kinetics of the photo degradation of MB by SnO$_2$@BTNTAs

Sl. No	Sample	Rate constant k (h^{-1})
1	Pure BTNTAs	0.168
2	SnO$_2$@BTNTAs, pH 8	0.252
3	SnO$_2$@BTNTAs, pH 10	0.378
4	SnO$_2$@BTNTAs, pH 12	0.558

The enhanced visible light photocatalytic activity of SnO$_2$@BTNTAs synthesized at different pH conditions when compared with pure BTNTAs is attributed to decreased energy band-gap as discussed above. The decrease in the band-gap energy facilitates rapid photo excitation of electrons promoting the photocatalysis rate. In the SnO$_2$ loaded BTNTAs structures, the oxygen vacancies, $V_o^{..}$ can act as electron trapping centers enhancing their photocatalytic activity. The surface morphology of the catalyst also has an important role in determining its photocatalytic activity [11]. In the case of the heterostructure synthesized at pH=8, surface of the BTNTAs are only partially deposited with SnO$_2$ exposing islands of BTNTAs on the surface (Fig. 4.4c) while in the SnO$_2$@BTNTAs synthesized at pH=10, surface of BTNTAs are deposited with flower- like SnO$_2$ (Fig. 4.4d). When the pH of the solution changes to 12, surface morphology is flake-like as a result of the delamination of the petals of the flower (Fig. 4.4e) leading to an increase in the effective surface area.

4.4 Conclusions

Well-ordered Barium titanate nanotubes were successfully surface modified with tin oxide nanoparticles having different morphologies to form novel SnO_2@BTNTAs heterostructures. SnO_2@BTNTAs were found to exhibit enhanced photocatalytic activity in the visible light region. The enhanced photocatalytic activity is attributed to the reduction in band-gap as a result of introduction of energy levels due to Ti^{3+} and $V_{\ddot{O}}$ within the energy band gap. Highest visible photocatalytic activity was observed for the SnO_2@BTNTAs obtained at pH=12, in which maximum amount of SnO_2 was deposited on the surface of BTNTAs. Morphological differences in SnO_2 at the surface of heterostructure were also found to play a key role in modifying their photocatalytic activity.

References

[1]   W. Wang, M. O. Tade, Z. Shao, Research progress of perovskite materials in photocatalysis and photovoltaics-related energy conversion and environmental treatment. Chem. Soc Rev. 44 (2015) 5371-5408.

[2]   P. Kanhere, Z. Chen, A Review on Visible Light Active Perovskite-Based Photocatalysts. Molecules, 19 (2014)19995-20022.

[3]   Y. Cui, J. Briscoe, S. Dunn, Effect of Ferroelectricity on Solar-Light-Driven Photocatalytic Activity of $BaTiO_3$-Influence on the Carrier Separation and Stern Layer Formation, Chem. Mater. 25 (2013) 4215−4223.

[4]   Y. Inoue, K. Sato, K. Sato, H. Miyama, Photoassisted water decomposition by ferroelectric lead zirconate titanate ceramics with anomalous photovoltaic effects, J. Phys. Chem. 90 (1986) 2809-2810.

[5]   V. M. Fridkin, Bulk photovoltaic effect in noncentrosymmetric crystals, Crystallogr. Rep. 46 (2001), 654 -658.

[6]   J. W. Bennett, I. Grinberg, A. M. Rappe, New Highly Polar Semiconductor Ferroelectrics through d8 Cation-O Vacancy Substitution into $PbTiO_3$: A Theoretical Study J. Am. Chem. Soc. 130 (2008)17409-17412.

[7]   T. Qi, I. Grinberg, A. M. Rappe, Band-gap engineering via local environment in complex oxides, Phys. Rev. B 83 (2011) 224108 (1-6).

[8]   H. Wang, L. Zhang, Z. Chen, J. Hu, S. Li, Z. Wang, J. Liu, X. Wang, Semiconductor heterojunction photocatalysts: design, construction, and photocatalytic performances, Chem. Soc. Rev. 43 (2014) 5234-5244.

[9]   R. X. Wang, Q. Zhu, W. S. Wang, C. M. Fan, A. W. Xu, $BaTiO_3$–graphene nanocomposites: synthesis and visible light photocatalytic activity New. J. Chem. 39 (2015) 4407-4413.

[10] D. Gong, C. A. Grimes, O. K. Varghese, W. Hu, R. S. Singh, Z. Chen, E. C. Dickey, Titanium oxide nanotube arrays prepared by anodic oxidation, J. Mater. Res. 16 (2001) 3331-3334.

[11] N. Lu, X. Quan, J. Y. Li, S. Chen, H. T. Yu, G. H. Chen, Fabrication of Boron-Doped TiO_2 Nanotube Array Electrode and Investigation of Its Photoelectrochemical Capability J. Phys. Chem. C 111 (2007) 11836-11842.

[12] Q. Kang, S. Liu, L. Yang, Q. Cai, C. A. Grimes, Fabrication of PbS Nanoparticle-Sensitized TiO_2 Nanotube Arrays and Their Photoelectrochemical Properties ACS Appl. Mater. Interfaces. 3 (2011) 746-749.

[13] X. F. Gao, W. T. Sun, Z. D. Hu, G. Ai, Y. L. Zhang, S. Feng, F. Li, L. M. Peng, An Efficient Method To Form Heterojunction CdS/TiO_2 Photoelectrodes Using Highly Ordered TiO_2 Nanotube Array Films, J. Phys. Chem. C. 113 (2009) 20481-20485.

[14] M. Nageri, V. Kalarivalappil, B. K. Vijayan, V. Kumar, Titania nanotube arrays surface-modified with ZnO for enhanced photocatalytic applications, Mater. Res. Bull. 77 (2016)   35-40.

[15] P. Roy, S. Berger, P. Schmuki, TiO_2 Nanotubes: Synthesis and Applications, Angew. Chem. Int. Ed. 50 (2011) 2904-2939.

[16] Y. Mao, S. Banerjee, S. S. Wong, Hydrothermal synthesis of perovskite nanotubes, Chem. Commun. (2003) 408-409.

[17] J. Zhao, X. Wang, R. Chen, L. Li, Synthesis of thin films of barium titanate and barium strontium titanate nanotubes on titanium substrates, Mater. Lett. 59 (2005) 2329-2332.

[18] J. Liu, Y. Sun, Z. Li, Ag loaded flower-like $BaTiO_3$ nanotube arrays: Fabrication and enhanced photocatalytic property, Cryst. Eng. Comm. 14 (2012) 1473-1478.

[19]   R. Li, Q. Li, L. Zong, X. Wang, J. Yang, $BaTiO_3/TiO_2$ heterostructure nanotube arrays for improved photoelectrochemical and photocatalytic , Electrochim. Acta. 91 (2013) 30-35

[20]   M. Ramezani, A. Sobhani-Nasab, S.M. Hosseinpour Mashkani, Synthesis, characterization, and morphological control of $Na_{1/2}Bi_{1/2}Cu_3Ti_4O_{12}$ through modify sol–gel method, J. Mater. Sci. Mater. El. 26 (2015) 4848-4853.

[21]   A. Javidan, M. Ramezani, A. Sobhani-Nasab, S. M. Hosseinpour- Mashkani, Synthesis, characterization, and magnetic property of monoferrite $BaFe_2O_4$ nanoparticles with aid of a novel precursor J. Mater. Sci. Mater. El. 26 (2015) 3813-3818.

[22]   A. Sobhani-Nasab, M. Behpour, Synthesis, characterization, and morphological control of $Eu_2Ti_2O_7$ nanoparticles through green method and its photocatalyst application, J. Mater. Sci. Mater. El. 27 (2016) 11946-11951.

[23]   M. Salavati-Niasari, F. Soofivand, A. Sobhani-Nasab, M. Shakouri- Arani, A. Yeganeh Faal, S. Bagheri, Synthesis, characterization, and morphological control of $ZnTiO_3$ nanoparticles through sol-gel processes and its photocatalyst application, Adv. Powder Technol. 27 (2016) 2066-2075.

[24]   L. Z. Liu, T. H. Li, X. L. Wu, J. C. Shen, P. K. Chu, Identification of oxygen vacancy types from Raman spectra of SnO_2 nanocrystals, J. Raman Spectrosc. 43 (2012) 1423-1426.

[25]   L. Ting-Hui, L. Hai-Tao, P. Jiang-Hong, Interplay between External Strain and Oxygen Vacancies on Raman Spectra of SnO_2, Chin. Phys. Lett. 31 (2014) 076201-076204.

[26]   L. Ying-Kai, D. Yi, W. Guang-Hou, Low-Frequency and Abnormal Raman Spectrum in SnO_2 Nanorods, Chin. Phys. Lett. 21 (2004) 156-159.

[27]   M. Murrata, K. Wakino, S. Ikeda, X-ray Photoelectron Spectroscopic Study of Perovskite Titanates and Related Compounds: An Example of the Effect of Polarization on

Chemical Shifts, J. Electron. Spectrosc. Rel. Phenomena, 6 (1975) 459-464.

[28] S. B. Rudraswamy, N. Bhatt, Optimization of RF Sputtered Ag-Doped BaTiO$_3$-CuO Mixed Oxide Thin Film as Carbon Dioxide Sensor for Environmental Pollution Monitoring Application, IEEE Sens. J. 16 (2016) 5145-5151.

[29] M. J. Jackman, A. G. Thomas, C. Muryn, Photoelectron Spectroscopy Study of Stoichiometric and Reduced Anatase TiO$_2$ (101) Surfaces: The Effect of Subsurface Defects on Water Adsorption at Near-Ambient Pressures, J. Phys. Chem. C 119 (2015) 13682-13690.

[30] A. M. Desbuquoit, J. Riga, J. J. Verbist, Electronic structure of titanium(III) and titanium(IV) halides studied by solid-phase x-ray photoelectron spectroscopy, Inorg. Chem. 26 (1987) 1212-1215.

[31] R. Ren, Z. Wen, S. Cui, Y. Hou, X. Guo, Controllable Synthesis and Tunable Photocatalytic Properties of Ti^{3+}-doped TiO$_2$, J. Chen, Sci. Rep. 5 (2015) 10714(1-11).

[32] V. Etacheri, M. K. Seery, S. J. Hinder, S. C. Pillai, Oxygen Rich Titania: A Dopant Free, High Temperature Stable, and Visible-Light Active Anatase Photocatalyst, Adv. Funct. Mater. 21 (2011) 3744-3752.

[33] S. Nayak, B. Sahoo, T. K. Chaki, D. Khastgir, Facile preparation of uniform barium titanate (BaTiO$_3$) multipods with high permittivity: impedance and temperature dependent dielectric behavior, RSC Adv. 4 (2014) 1212-1224.

[34] L. Ran, D. Zhao, X. Gao, L. Yin, Highly crystalline Ti-doped SnO$_2$ hollow structured photocatalyst with enhanced photocatalytic activity for degradation of organic dyes, Cryst. Eng. Comm. 17 (2015) 4225-4237.

[35] L. Y. Liang, Z. M. Liu, H. T. Cao, X. Q. Pan, Microstructural, Optical, and Electrical Properties of SnO Thin Films Prepared on Quartz via a Two-Step Method, ACS Appl. Mater. Interfaces 2 (2010) 1060-1065.

[36]   Y. C. Her, J. Y. Wu, Y. R. Lin, S. Y. Tsai, Low temperature growth and blue luminescence of SnO_2 nanoblades, Appl. Phys. Lett. 89 (2006) 043115(1-3).

[37]   M. M. Khan, S. A. Ansari, D. Pradhan, M. O. Ansari, D. H. Han, J. Lee, M. H. Cho, Band gap engineered TiO_2 nanoparticles for visible light induced photoelectrochemical and photocatalytic studies, J. Mater. Chem. A, 2 (2014) 637-644.

[38]   B. Sarkar, K. Chakrabarti, K. Das, S. K. De, Optical and ferroelectric properties of ruthenium-doped $BaTiO_3$ nanocubes, J. Phys. D: Appl. Phys. 45 (2012) 505304 (1-10).

[39]   D. D. Cuong, J. Lee, Electronic structure of oxygen deficient $BaTiO_3$, Integr. Ferroelectr. 84 (2006) 23-30.

CHAPTER 5
Manganese-doped BaTiO₃ nanotube arrays for enhanced visible light photocatalytic applications

CONTENTS

5.1 Introduction

ABO_3 type ferroelectric perovskites are emerging as potential candidates for photocatalytic and solar cell applications [1-6]. Though the wide band-gap of ferroelectric oxides like $BaTiO_3$ has hindered their applications in the visible light region many strategies have been employed to engineer the band gap to enhance its application in this region. They include fabrication of heterogeneous nanostructures with suitable materials or doping with transition metal cations. Recently we have shown that photocatalytic activity of $BaTiO_3$ in the visible light region can be enhanced through the use of heterogeneous nanostructures like $SnO_2@BaTiO_3$ [7]. In ferroelectric $BaTiO_3$, its visible light driven photocatalytic activity can also be enhanced through substitution of A^{2+} and B^{4+} cations in the ABO_3 perovskite structure with aliovalent ions. B-site doping with trivalent transition metal cations is known to introduce defect energy levels in the energy band- gap yielding an E_g in the visible light region. This offers them excellent application potential, especially in visible light driven photocatalysis. The photocatalytic applications of $BaTiO_3$ doped with Rh^+, Fe^{3+} Zn^{2+}, Y^{3+}, and Ag^+ have already been reported [8-14]. The morphology of the material also plays a crucial role in determining its photocatalytic activity [15, 16]. Tubular morphology offers advantages since their diameter, length and pore size can be easily tailored for specific applications [17, 18]. Though the fabrication and photocatalytic applications of $BaTiO_3$ nanotubes have been reported [19-21], the modification of $BaTiO_3$-nanotubes with Mn^{3+} for photocatalytic applications has not yet been reported. Hence in this

175

study we prepared B-site Mn^{3+}-doped $BaTiO_3$ nanotube arrays through a combination of anodisation followed by hydrothermal method. The mechanism responsible for enhanced visible light photocatalytic activity of these B-site Mn^{3+}-doped $BaTiO_3$ have also been investigated and reported.

5.2 Experimental details

Ti-metal foil (99.5%, Alfa Aesar),Ethylene glycol (99%, Merck), Ammonium fluoride (98%, Sigma Aldrich), Barium hydroxide (95%, Alfa Aesar), Manganese (III) acetylacetonate (technical grade, Aldrich) and Iso-propyl alcohol (97.9%, Merck) were used as such for the fabrication of Mn^{3+}- doped BTNTA.

Titania nanotubes were synthesized by anodisation of titanium foil in a two electrode cell with titanium foil as working electrode and Pt as counter electrode in an ethylene glycol-fluoride electrolyte at 40 *V* for 24 *h*. Prior to anodisation the titanium foil was sonicated in acetone for 10 *min*, washed with distilled water and dried. The electrolyte for anodisation was prepared by dissolving NH_4F (0.16 *M*) in an ethylene glycol (96.5 *mL*) and water (3.5 *mL*) mixture. The anodized Ti foil was then thoroughly washed with distilled water to remove residual F^- ions followed by drying at room temperature.

Manganese (III) acetyl acetonate was dissolved in a mixture of 60.0 *mL* of deionized water and 20 *mL* of isopropyl alcohol to get different concentrations (0.005, 0.01 and 0.02 *M*). The titania nanotube arrays prepared as above were kept immersed in these solutions in a 125 *mL* teflon lined hydrothermal vessel (Parr instrument company, U. S. A)

and kept in an oven at $120^0 C$ for 2 h to obtain Mn^{3+}-doped titania nanotube arrays. After hydrothermal treatment the samples were washed thoroughly with distilled water and dried. The undoped and Mn^{3+}-doped titania nanotubes were then immersed in a solution of 0.05 M barium hydroxide monohydrate in a teflon lined hydrothermal vessel and kept in an oven at $180^0 C$ for 2 h to obtain the corresponding nanotube arrays of BMn$_x$TNTA; where x=0, 0.005, 0.01 and 0.02 hereafter referred to as BTNTA, BMn5TNTA, BMn10TNTA and BMn20TNTA respectively. After hydrothermal treatment the samples were washed thoroughly with distilled water and dried at room temperature. Schematic representation of the synthetic procedure adopted for the BMnxTNTA photocatalyst is provided in Figure 5.1.
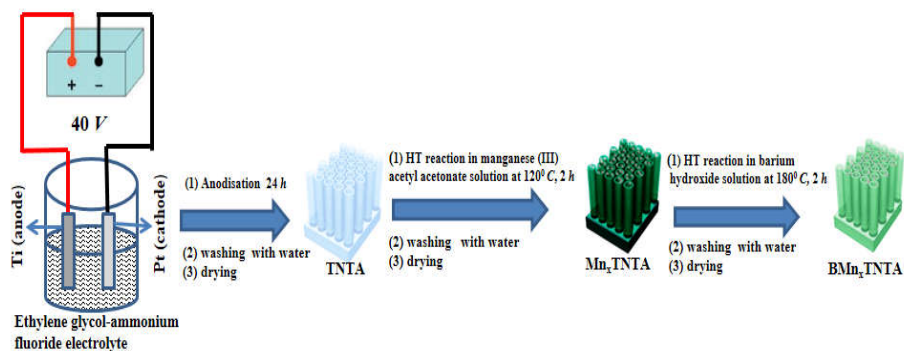
Fig. 5.1: Schematic representation of synthetic steps of BMn$_x$TNTA.

The Raman spectra of the samples were recorded using a Raman spectrometer [DXR, Thermo Scientific, USA, 532 nm laser excitation]. The laser power was fixed at 10 mW for all sample analysis. Crystalline phase of the samples were determined using an X-ray diffractometer [XRD, D5005, Bruker, Germany]. Surface morphology and elemental composition of the nanotube arrays were determined by

a scanning electron microscope interfaced with an EDX system [FEI, Nova Nano SEM 450, US]. Absorption and diffuse reflectance spectra were obtained using a UV-Visible spectrometer [Jasco-V-550-UV/VIS spectrometer, Japan]. X-ray Photoelectron Spectroscopy was carried out on an XPS [Axis-Ultra, Kratos Analytical, UK] at 2.3x 10^{-9} torr using a monochromatic Al-Kα X-ray (1486.6 eV) source. All the binding energies of the elements were calibrated to carbon binding energy of 284. 60 eV which corresponds to the standard value of C-H and C-C bonds. The magnetization measurements were carried out using a Vibrating sample Magnetometer [Model: 7410 series, Lakeshore, USA]. Electron Paramagnetic Resonance spectroscopy of sample was carried out using an EPR spectrometer (Model-JES, JEOL, Japan) at room temperature in the X-band frequency of 9.17 GHz. The peaks in the Photoluminescence and X-ray Photoelectron Spectra were deconvoluted by multiple-peak Gaussian function fitting analysis.

The photocatalytic activity of the different samples was determined by studying the degradation of methylene blue (MB) dye in aqueous solution. In a typical experiment, BMn_xTNTA having an area of 1.0 cm^2 was placed in a cuvette containing the MB dye solution of concentration 8.5 mg/L. The above cuvette was kept in the dark for 1 h to acquire adsorption-desorption equilibrium of dye over the film. The dye solution containing the film was subsequently illuminated by a visible light source of a 300 W Tungsten lamp [Immersion type photo reactor HEBER, India]. The degradation was monitored, at different time intervals, by determining the concentration of the MB dye at regular intervals using a UV-Vis spectrometer.

5. 3 Results and discussion

It is seen from the XRD pattern [Fig. 5.2A, (i)] that barium titanate nanotubes crystallise in the cubic structure (JCPDS 31-0174). As the amount of Mn^{3+} increases the crystal structure changes from cubic to tetragonal and then to hexagonal [22]. For BMn5TNTA, the crystal structure is tetragonal as revealed by the splitting of the peak at $2\theta \sim 45^0$ corresponding to reflections from the (002) and (200) planes (JCPDS 05-0626) [Fig. 5.2A, (ii)]. For further increase in the concentration of Mn^{3+}, peak at $2\theta \sim 24.8^0$ corresponds to (004) plane of the hexagonal phase (JCPDS 34-0129) as shown in Figures 5.2A, (iii-iv). At high Mn^{3+} concentrations x ≥ 0.02, stabilization of the hexagonal structure is attributed to the face sharing of adjacent TiO_6 octahedra [Ti_2O_9] as a result of increase in oxygen vacancy concentration.
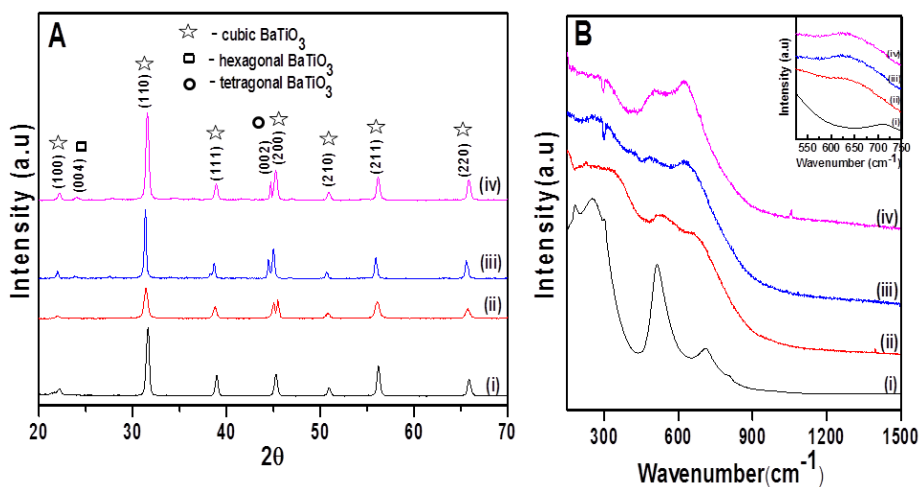

Fig. 5.2: A) XRD patterns and B) Raman Spectra of (i) BTNTA (ii) BMn5TNTA (iii) BMn10TNTA (iv) BMn20TNTA [inset shows Raman spectra from 525 to 750 cm⁻¹].

The presence of different crystalline modification of $BaTiO_3$ has also been confirmed from their Raman spectra (Fig. 5.2B). Cubic $BaTiO_3$ has Oh symmetry and belongs to P*m3m* space group. Optical vibrational modes of cubic $BaTiO_3$ contains three triply degenerate phonon modes of F_{1u} and one triply degenerate mode of F_{2u} (Total modes of vibrations are $3F_{1u}+F_{2u}+F_{1u}$ including acoustic vibrations, in which total number of optical vibrational modes are 12, and they are $3F_{1u}+F_{2u}$). Among these optical vibrational modes none of them is Raman active. Tetragonal $BaTiO_3$ has C_{4V} symmetry (P4*mm* group). In the case of tetragonal $BaTiO_3$, each of F_1u mode of the cubic structure splits into a nondegenarate A_1 mode and a doubly degenerate E mode. F_2u phonon mode also splits into B_1 and E modes, hence the optical vibration modes of tetragonal $BaTiO_3$ are $3A_1+B_1+4E$ (Total vibrational modes of $BaTiO_3$ are $4A_1+B_1+5E$, including acoustic modes). A_1 and E modes again split into transverse (TO) and longitudinal (LO) optical modes. All the optical vibrations are Raman active in case of tetragonal $BaTiO_3$. Hexagonal $BaTiO_3$ has D_{6h} symmetry group and belongs to P6$_3$/*mm*c space group. Optical vibration modes of hexagonal $BaTiO_3$ are $5A_{1g} + 2A_{2g} + 6B_{1g} + B_{2g} + 6E_{1g} + 8E_{2g} + A_{1u} + 6A_{2u}+ 2B_{1u} + 6B_{2u} + 8E_{1u} + 7E_{2u}$, in which the Raman active phonon modes are A_{1g}, E_{1g} and E_{2g}. In hexagonal $BaTiO_3$ the intense Raman peak is generally observed at ≈ 636 cm^{-1} corresponding to the A_{1g} mode of optical vibration [23].

Raman spectra of BTNTA and BMn$_x$TNTA are shown in Figure 5.2B. The different characteristic vibrational modes of $BaTiO_3$ are observed in pure BTNTA and in BMn$_x$TNTA at 261 [A_1 (TO)], 305 [B_1], 517

[A$_1$+E (TO)], and 718 cm^{-1} [A$_1$+ E (LO)] as shown in Figure 5.2B, (i-iv). The B$_1$ phonon mode at 305 cm^{-1}corresponding to the tetragonal crystalline modification is more intense in BMn10TNTA and BMn20TNTA as shown Figure 5.2B, (iii-iv), which also confirms the increased tetragonality of BMn10TNTA and BMn20TNTA [24]. With increasing Mn^{3+} concentration it is observed that the phonon mode at $\approx$ 628 cm^{-1} corresponding to the hexagonal phase is increasing in intensity [25].
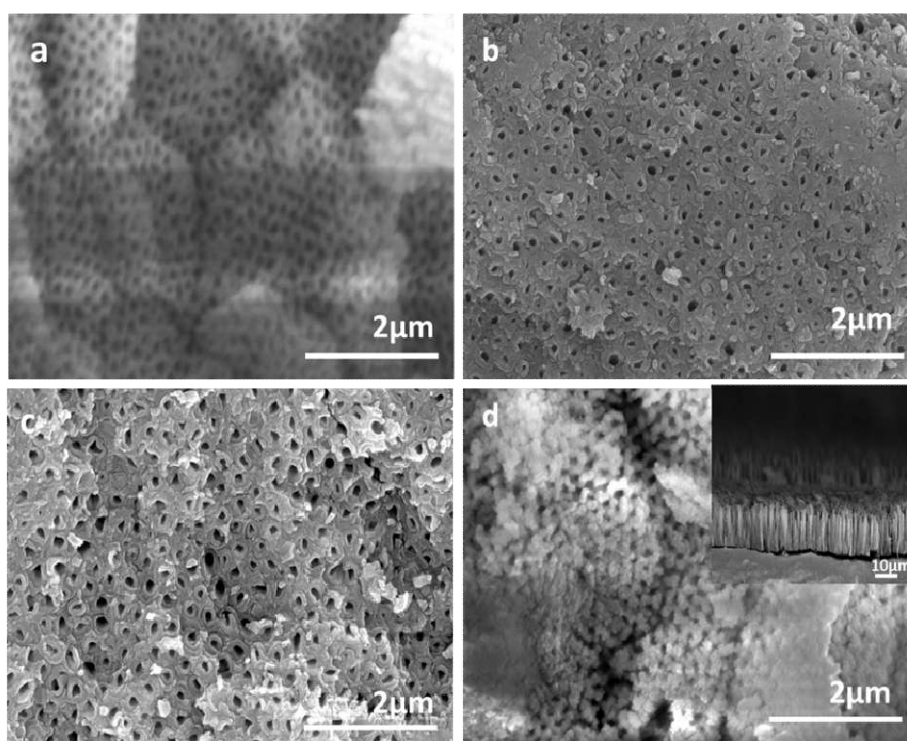
Fig. 5.3: SEM images of the surface of (a) BTNTA (b) BMn5TNTA (c) BMn10TNTA and (d) BMn20TNTA [*inset shows cross-sectional SEM image of the same*].

Figure 5.3a shows a typical SEM image of the surface of BTNTA, revealing well-ordered and aligned barium titanate nanotubes. The

surface morphology of the barium titanate nanotube with different Mn-concentrations are shown in Figures 5.3, b-d revealing morphological similarity. For all Mn-substituted samples the tubular morphology is retained. The vertically aligned nanotube array is further confirmed from the cross-sectional SEM image as shown in the inset of the Figure 5.3d. Chemical composition and purity of samples were analysed by EDX. The EDX spectra obtained for BTNTA and Mn-doped BTNTA are provided in Figure 5.4, a-d. It is observed that for pure BTNTA only Ba, Ti and O are present where as for BMnxTNTA in addition to Ba, Ti, and O, Mn is also present and the amount of Mn increases as the doping concentration of Mn increases. No other elements are observed in the EDX spectra, clearly revealing the purity of the samples.
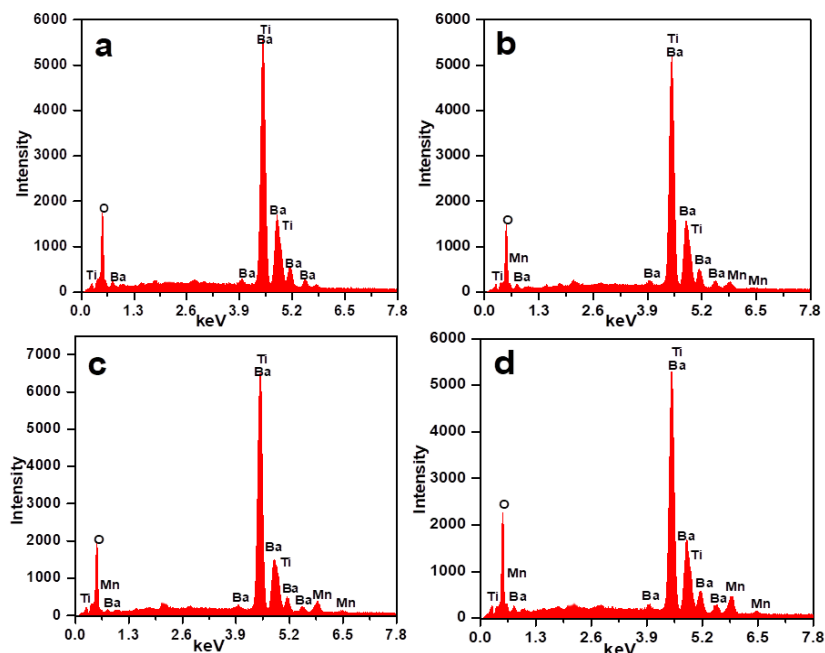
Fig. 5.4: EDX pattern of (a) BTNTA (b) BMn5TNTA (c) BMn10TNTA (d) BMn20TNTA.

The absorption spectra of pure BTNTA and BMn$_x$TNTA are shown in Figure 5.5A. It can be clearly observed that in the case of BMn$_x$TNTA the absorption extends to the visible light region when compared with that of pure BTNTA. It is seen that BMn20TNTA has an intense green color and exhibits the highest red shift as shown in the absorption spectra [Fig. 5. 5A(iv)].
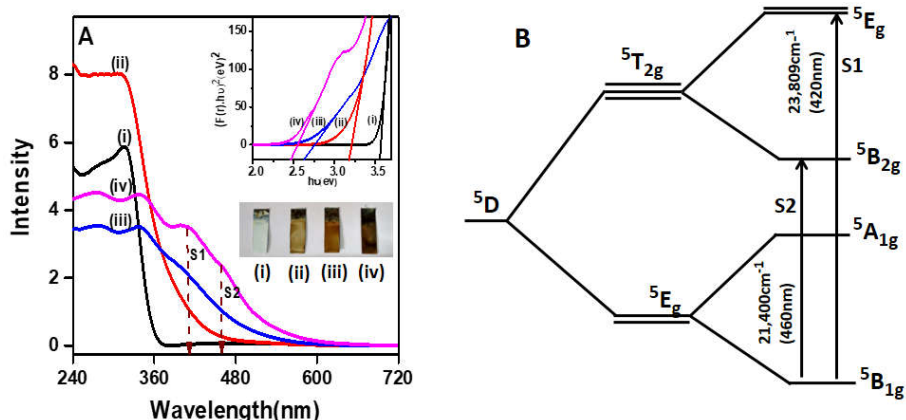
Fig. 5.5: A) Absorption spectra of (i) BTNTA (ii) BMn5TNTA (iii) BMn10TNTA (iv) BMn20TNTA and photographs of the same. Inset shows Kubelka-Monk plot and B) alteration of orbital energies of Mn^{3+} (d^4), due to strong Jahn-Teller distortion.

As the concentration of Mn^{3+} increases from 0 to 0.02 two additional bands are also observed in the visible region denoted as S1 and S2 (Fig. 5.5A). The peak at 460 *nm* (S2) which is broad with its tail extending up to ≈ 520 *nm*, is due to the $^5B_{1g} \rightarrow {}^5B_{2g}$ transition whereas the one at 420 *nm* is attributed to $^5B_{1g} \rightarrow {}^5E_g$ transition as represented in Figure. 5.5B. These peaks arise due to the strong Jahn-Teller distortion exhibited by Mn^{3+}-ion in the MnO$_6$ octahedra [26-28] as shown in Figure 5.6.
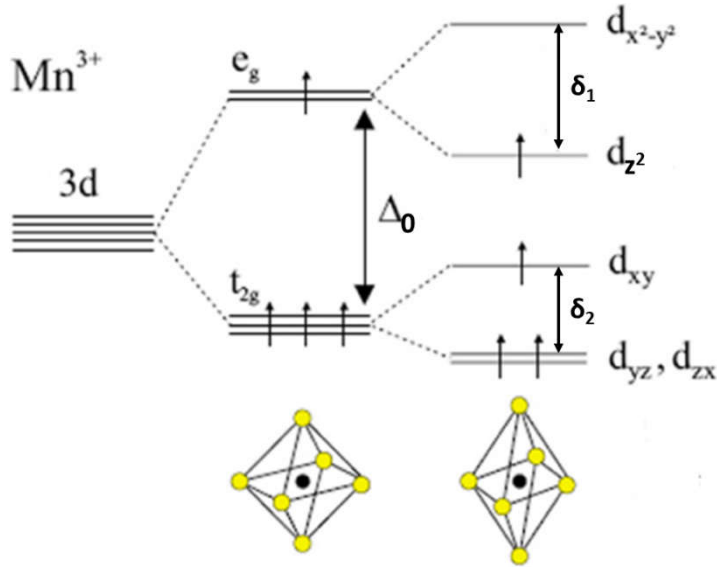
Fig. 5.6: Octahedral splitting and Jahn-Tellar distortion exhibited by Mn^{3+} ion in MnO$_6$-octahedra.

[Source: P. K. Siwach et al, Low Field Magnetotransport in Manganites, J. Phys. Condens. Matter, 20 (2008) 273201]

In BaTiO$_3$, B-site Mn^{3+}doping create oxygen vacancies as represented below in equation (5.1) for the B-site sublattice.

$$Mn_2O_3 \xrightarrow{2TiO_2} 2Mn'_{Ti} + 3O^x_O + 2V^{\cdot}_O \qquad \text{———} \qquad (5.1)$$
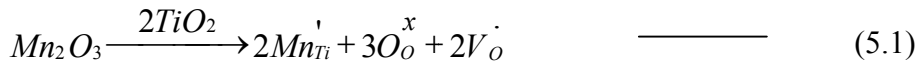
The singly ionised oxygen vacancy in BaTiO$_3$, $V^{\cdot}_O$ creates Ti^{3+} due to charge compensation. As the amount of Mn^{3+} increases more oxygen vacancies are generated in BaTiO$_3$ which in turn creates more number of Ti^{3+} ions. Ti^{3+} are acceptor defects having energy levels near the valence band maximum whereas the oxygen vacancies are donors having energy levels near the conduction band minimum [7, 29, 30]. In addition, Mn^{3+} ions in BaTiO$_3$ introduce energy levels within the band-gap due to the Jahn-Teller-distortion as shown in Figure 5.7B. It

184

is reported that in Mn-doped BaTiO$_3$ systems the t$_{2g}$ orbitals of Mn^{3+} overlap with valence band and e$_g$ orbitals overlap with the conduction band of BaTiO$_3$ [31].

The presence of energy levels due to defects within the band-gap is also confirmed from the photoluminescence spectra of Mn-doped BTNTA [Fig. 5.7A]. The schematic representation of energy levels and emissions are shown in Figure 5.7B. On deconvolution of the broad band, four peaks centered at different wavelengths are obtained. The peak denoted as E$_a$, [Figs. 5.7A and B] centered at 390 *nm* is due to near band edge emission of barium titanate nanotubes. The peak (E$_b$) at 445 *nm* is attributed to the transition from the e$_g$ levels of Ti^{3+}, lying below the conduction band minimum to the valence band and the one at 516 *nm* (E$_d$) is due to the transition from the doubly degenerate (d$_{xz}$, d$_{yz}$) level to the valence band [29]. The blue emission located at $\approx$ 485 *nm* (peak-E$_c$), is due to the emission from the level associated with singly ionised oxygen vacancy($V_O^{\cdot}$) in Mn-doped BTNTA [32]. The relative intensities of E$_b$ and E$_d$ peaks with respect to the other peaks show gradual increase as the Mn-concentration increases which clearly indicate the increase in the density of the energy levels of Ti^{3+} defects.
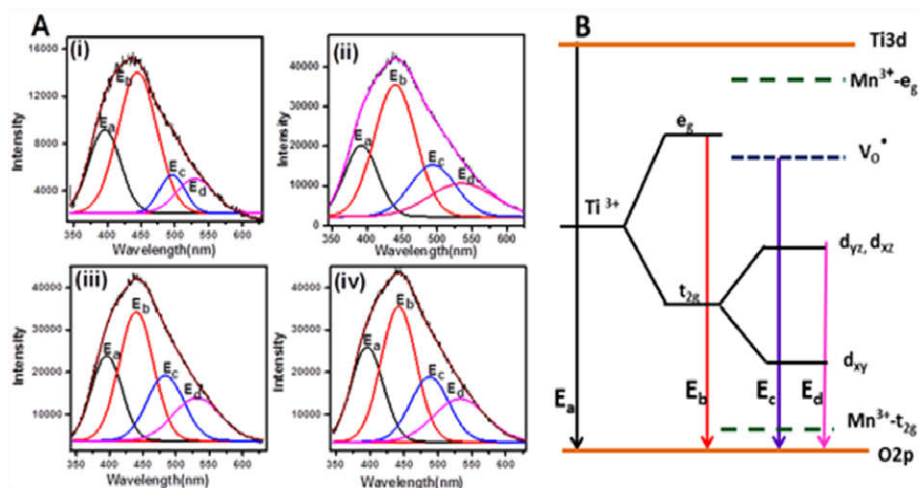
Fig. 5.7: A) Photoluminescence spectra of (i) BTNTA (ii) BMn5TNTA (iii) BMn10TNTA (iv) BMn20TNTA and B) defective band structure of Mn-doped BaTiO₃.

Direct evidence for the presence of Ti^{3+}, Mn^{3+} and $V_{\ddot{O}}$ was obtained from the XPS measurements. In undoped BTNTA the $Ti2p_{3/2}$ and $Ti2p_{1/2}$ binding energies are 457.3 and 463.0 eV respectively [Fig. 5.8A,(i)]. The observed split of 5.7eV between the two J states confirms the +4 valence state of Titanium [33, 34]. In the case of Mn-doped BTNTA having $[Mn^{3+}]$ =0.01, the $Ti2p_{3/2}$ binding energy is negatively shifted to 456.8 eV [Fig. 5.8A,(ii)], clearly indicating the presence of Ti^{3+} ions [35, 36]. The O1s peak at 530.6 eV due to the binding energy of oxygen in Ti^{4+}-O-Ti^{4+} [Fig.5.8B,(i)] in undoped BTNTA, is negatively shifted to 529.3 eV in the Mn-doped BTNTA [Fig. 5.8B,(ii)]. The negative shift of this peak from that observed in unsubstituted BTNTA shows the change in the oxygen environment in the BO_6 octahedra in Mn^{3+}-doped BTNTA [37, 38]. The O1s peak observed at 528.5 and 528.7 eV represents the Ba-O-Ti lattice oxygen in BTNTA and Mn-BTNTA respectively [39]. The peak observed at

531.85 *eV* in BTNTA and at 531.0 *eV* in Mn-doped BTNTA is attributed to surface adsorbed hydroxyl ions. In the case of manganese, Mn^{2+}, Mn^{3+} and Mn^{4+} are expected. All these states contain unpaired d-electrons and are reported to exhibit multiplet 2p structure. The $Mn2p_{3/2}$-$2p_{1/2}$ energy separation in BMn10TNTA is 11.9 *eV*. For the precise determination of oxidation state of Mn, we have deconvoluted [40] the $Mn2p_{3/2}$ peak as shown in Figure 5.8C. The peak [Fig. 5.8C] corresponding to Mn^{2+} is observed at 640.8 *eV* (FWHM-1.76 *eV)* whereas the more intense peak observed at 642.1 *eV* (FWHM-1.95 *eV)* is due to the presence of Mn^{3+} ions and the peak at 644.4 *eV* (FWHM-1.68 *eV*) represents the Mn^{4+} ions [40, 41]. The presence of Mn^{2+} and Mn^{4+} states is due to the facile disproportionation of Mn^{3+}[42].
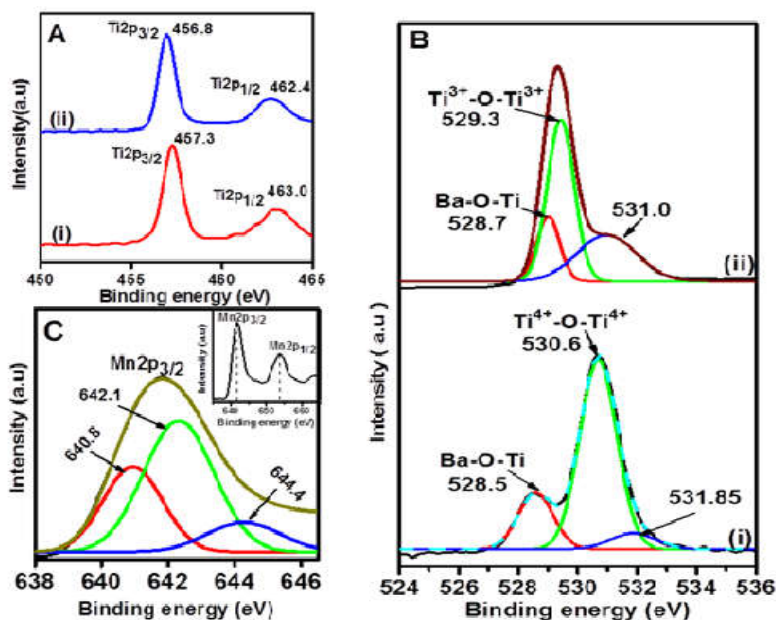
Fig. 5.8: XPS spectra of (A) Ti2p of (i) BTNTA and (ii) BMn10TNTA (B) O1s of (i) BTNTA and (ii) BMn10TNT(C) Mn2p$_{3/2}$-peak of BMn10TNTA [Inset shows the doublet XPS peak of Mn-ion].

The influence of defects is further confirmed from the magnetization measurements of the samples. Magnetization measurements carried out at room temperature for pure and Mn-doped barium titanate samples show paramagnetic ordering for [Mn^{3+}] concentrations in the range $0 \leq x \leq 0.01$ as shown in Figures 5.9(i-iii). On further increase in the concentration of Mn^{3+}, x = 0.02, weak ferromagnetic (FM) ordering is observed [Fig. 5.9(iv)]. This can be explained as follows.

In $BaTiO_3$, B-site Mn^{3+}- doping leads to the creation of charge compensating, singly ionised oxygen vacancies $V_{\ddot{O}}$ (F-centers) as confirmed from EPR spectrum [Fig. 5.9B]. $V_{\ddot{O}}$ form bound magnetic polarons (BMP) coupling the 3d moments of Mn^{2+} ions. At $x \geq 0.02$, the density of BMP attains the percolation limit leading to FM coupling [25, 43-45]. These results confirm the formation of $V_{\ddot{O}}$ defects. Figure 5.10 shows the schematic representation of bound magnetic polarons formed in Mn doped system.
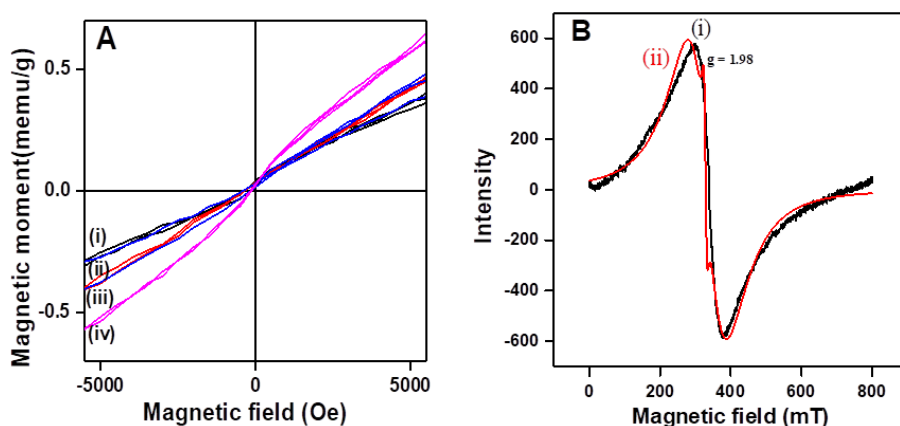
Fig. 5.9: (A) M-H curves of (i) BTNTA; (ii) BMn5TNTA; (iii) BMn10TNTA; (iv) BMn20TNTA and (B) EPR spectrum of BMn20TNTA [(i) observed (ii) simulated].
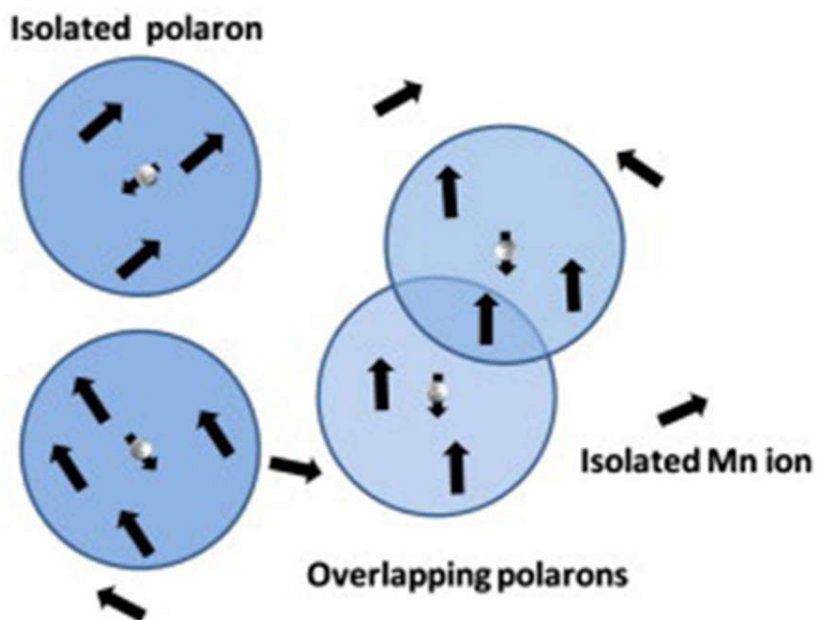
Fig. 5.10: Schematic representation of bound magnetic polaron in an Mn doped system, the blue circles the polarons, the white balls with little arrow denotes the hole spin and the big arrow denotes the Mn^{2+}-ion.

[Source: J. Z. Cai et al, Bound magnetic polaron driven low-temperature ferromagnetism in Cu$_{1-x}$Mn$_x$O compounds, Physica. B Condens. Matter, 424 (2013) 42-46]

The characteristic absorption bands of the MB dye in presence and absence of the photocatalyst are shown Figure 5.11A. It is observed that the concentration of the dye decreases in presence of the photocatalyst under visible light illumination as a function of time. The decrease in concentration of MB (c/c_0) with respect to time under visible light illumination in presence of Mn-BTNTAs samples are plotted in Figure 5.11B, where c is the concentration at time t and c_o is the initial concentration. The reference MB dye solution having the same concentration without the catalyst did not show any degradation under identical illumination conditions (The reference MB dye has a

maximum absorption at $\lambda=663$ *nm*). The photocatalytic degradation follows first order reaction kinetics and the rate constant *k*, calculated from the slope of plots of $-\ln(c/c_0)$ vs time (*t*), are given in Table 5.1. It is seen that BMn20TNTA exhibit the maximum photocatalytic activity with a rate constant, $k = 0.564 \ h^{-1}$.
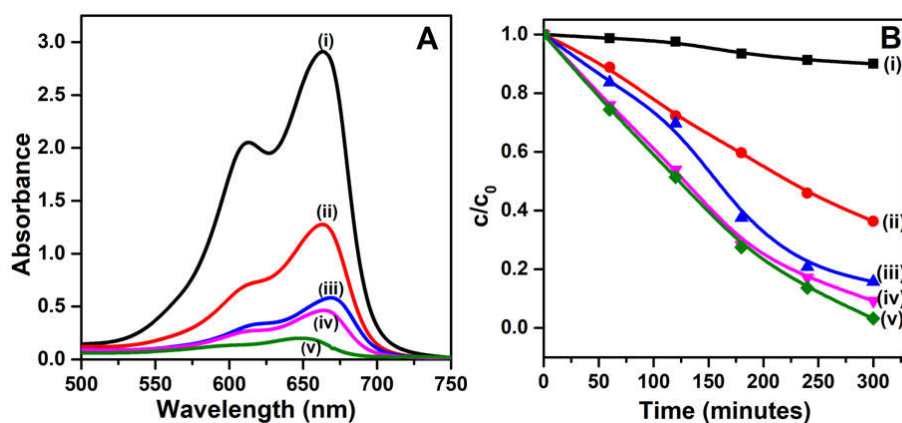
Fig. 5.11: (A) UV-Vis spectra of MB dye after 5 *h* visible light irradiation and (B) $-\ln(c/c_0)$ vs time plots of (i) without catalyst and with (ii) BTNTA; (iii) BMn5TNTA;(iv) BMn10TNTA; and (v) BMn20TNTA.

Table 5.1 Kinetics of photo degradation of MB by Mn- doped BTNTA

Serial. No	Sample Name	Rate constant (h^{-1})
1	BTNTA	0.192
2	BMn5TNTA	0.354
3	BMn10TNTA	0.444
4	BMn20TNTA	0.564

Table 5.2 Comparison of photocatalytic activity of BMn$_x$TNTA with other modified Barium titanate

Nature of catalyst	Concentration of dye and area or amount of catalyst used for photocatalysis	Intensity of light source	Rate constant (K, time^{-1}) % degradation	Reference
Ag-doped BaTiO$_3$ nano tubes film	Methyl orange solution of 20mg/L (75mL) area of catalyst- 6 cm^2	A 350 W, high pressure mercury lamp used as the UV source	4.24h^{-1},98.53%, 60 min	J. Liu et al [12]
Ag/BaTiO$_3$ film	Rhodamine solution of 20 mM is spin coated on Ag/BaTiO3 film of area 4 cm^2	A 20 W UV lamp as UV source and 500 W xenon lamp used as source of both visible and UV-Vis source	43%, 300 min, in UV-vis source and 62%, 300 min in Visible light	S.Zhang et al [13]
Ag/BaTiO$_3$ powder	Rhodamine B solution of 10 mg/L (50mL) Amount of catalyst- 0.15 g	Solar simulator used as the source, radiation intensity is fixed as 100 mW cm^{-2}	0.087 min^{-1}	Y. Cui et al [14]
BaTiO$_3$/TiO$_2$ nanotube film heterostructure	Methylene blue solution of 10 mg/L (30 mL) Area of the catalyst-4 cm^2	A 300 W xenon lamp used as light source	72%, 180 min	R. Li et al [21]
SnO$_2$/BaTiO$_3$ nanotube film heterostructure	Methylene blue solution of 8.5 mg/ L (4 mL) Area of catalyst- 1 cm^2	A 300 W tungsten filament lamp used as visible light source	0.558 h^{-1} (93.58%, 360min)	M.Nageri et al. [7]
Mn-doped BaTiO$_3$ nanotube film	Methylene blue solution of 8.5 mg/ L (4 mL) Area of catalyst-1 cm^2	A 300 W tungsten filament lamp used as visible light source	0.564 h^{-1} (97.04% , 360 min)	Present study

The visible light photocatalytic activities exhibited by BMn$_x$TNTA are comparable or better than with those reported for other modified BaTiO$_3$ in literature as given in Table 5.2. The enhanced visible light photocatalytic activity of Mn-doped BTNTA when compared with that of undoped BTNTAs is attributed to decreased energy band-gap as discussed above. The decrease in the band-gap energy facilitates rapid photo excitation of electrons promoting the photocatalysis rate. In the

Mn-doped BTNTAs the oxygen vacancies can act as electron trapping centers enhancing their photocatalytic activity.

5.4 Conclusions

Well-ordered B-site Mn^{3+} doped barium titanate nanotube arrays (BMn_xTNTA) have been prepared by hydrothermal method. Mn-doped BTNTA were found to exhibit enhanced visible light driven photocatalytic activity. The modulation in the band-gap as a result of introduction of energy levels due to Ti^{3+}, Mn^{3+} and $V_O^{\cdot\cdot}$ defects within the energy band-gap have been correlated with the photocatalytic activity. Defect mediated room temperature ferromagnetism was also investigated in these compositions to unravel the influence of ($V_O^{\cdot\cdot}$) F-centers.

References

[1]   W. Wang, M. O. Tade, Z. Shao, Research progress of perovskite materials in photocatalysis and photovoltaics-related energy conversion and environmental treatment, Chem. Soc. Rev. 44 (2015) 5371-5408.

[2]   P. Kanhere, Z. Chen, A Review on Visible Light Active Perovskite-Based Photocatalysts, Molecules 19 (2014) 19995-20022.

[3]   G. Zhang, G. Liu, L. Wang, J. T. S. Irvine, Inorganic perovskite photocatalysts for solar energy utilization, Chem. Soc. Rev. 45 (2016) 5951-5984.

[4]   R. Konta, T. Ishii, H. Kato, A. Kudo, Photocatalytic Activities of Noble Metal Ion Doped $SrTiO_3$ under Visible Light Irradiation, J. Phys. Chem. B 108 (2004) 8992-8995.

[5]   R. Asai, H. Nemoto, Q. Jia, K. Saito, A. Iwase, A. Kudo, A visible light responsive rhodium and antimony codoped $SrTiO_3$ powdered photocatalyst loaded with an IrO_2 cocatalyst for solar water splitting, Chem. Commun. 50 (2014) 2543–2546.

[6]   K. Iwashina, A. Kudo, Rh-Doped $SrTiO_3$ Photocatalyst Electrode Showing Cathodic Photocurrent for Water Splitting under Visible-Light Irradiation, J. Am. Chem. Soc. 133 (2011) 13272–13275.

[7]   M. Nageri, A. B. Shalet, V. Kumar, SnO_2-loaded $BaTiO_3$ nanotube arrays: fabrication and visible-light photocatalytic application, J. Mater. Sci: Mater.Electron. 28 (2017) 9770-9776.

[8]   K. Maeda, Rhodium-Doped Barium Titanate Perovskite as a Stable p-Type Semiconductor Photocatalyst for Hydrogen Evolution under Visible Light, ACS Appl. Mater. Interfaces 6 (2014) 2167–2173.

[9]   S. Upadhyay, J. Shrivastava, A. Solanki, S. Choudhary, V. Sharma, P. Kumar, N. Singh, V. R. Satsangi, R. Shrivastav, V. Umesh, U. V. Waghmare, S. Dass, Enhanced

Photoelectrochemical Response of BaTiO$_3$ with Fe Doping: Experiments and First-Principles Analysis, J. Phys. Chem. C 115 (2011) 24373–24380.

[10] Z. Ping Zou, L. Zhu Zhang, S. LianLuo, L. Hui Leng, X. Biao Luo, M. Jian Zhang, Y. Luo, G. Cong Guo, Preparation and photocatalytic activities of two new Zn-doped SrTiO$_3$ and BaTiO$_3$ photocatalysts for hydrogen production from water without cocatalysts loading, Int. J. Hydrogen Energy 37 (2012) 17068-17077.

[11] Z. Shen, Y. Wang, W. Chen, H. Lai Wah Chan, L. Bing, Photocatalysis of Yttrium Doped BaTiO$_3$ Nanofibres Synthesized by Electrospinning, J. Nanomater. Volume 2015 (2015) Article ID 327130, 6 pages.

[12] J. Liu, Y. Sun, Z. Li, Ag loaded flower-like BaTiO$_3$ nanotube arrays: Fabrication and enhanced photocatalytic property, Cryst. Eng. Comm. 14 (2012) 1473-1478.

[13] S. Zhang, B. ping Zhang, S. Li, Z. Huang, C. Yang, H. Wang, Enhanced photocatalytic activity in Ag-nanoparticle-dispersed BaTiO$_3$ composite thin films: Role of charge transfer, J. Adv. Ceram. 6 (2017) 1–10.

[14] Y. Cui, J. Briscoe, S. Dunn, Effect of Ferroelectricity on Solar-Light-Driven Photocatalytic Activity of BaTiO$_3$-Influence on the Carrier Separation and Stern Layer Formation, Chem. Mater. 25 (2013) 4215−4223.

[15] N. M. Flores, U. Pal, R. Galeazzi, A. Sandoval, Effects of morphology, surface area, and defect content on the photocatalytic dye degradation performance of ZnO nanostructures, RSC Adv. 4 (2014) 41099-41110.

[16] M. Nageri, V. Kalarivalappil, B. K. Vijayan, V. Kumar, Titania nanotube arrays surface-modified with ZnO for enhanced photocatalytic applications, Mater. Res. Bull. 77 (2016) 35-40.

[17] P. Roy, S. Berger, P. Schmuki, TiO$_2$ Nanotubes: Synthesis and Applications, Angew. Chem. Int. Ed. 50 (2011) 2904 – 2939.

[18]   C. Adan, J. Marugan E. Sanchez, C. Pablos, R. V. Grieken, Understanding the effect of morphology on the photocatalytic activity of TiO_2 nanotube array electrodes, Electrochim. Acta. 191 (2016): 521-529.

[19]   Y. Mao, S. Banerjee, S. S. Wong, Hydrothermal synthesis of perovskite nanotubes, Chem. Commun. 0 (2003) 408-409.

[20]   J. Zhao, X. Wang, R. Chen, L. Li, Synthesis of thin films of barium titanate and barium strontium titanate nanotubes on titanium substrates, Mater. Lett. 59 (2005) 2329-2332.

[21]   R. Li, Q. Li, L. Zong, X. Wang, J. Yang, $BaTiO_3/TiO_2$ heterostructure nanotube arrays for improved photoelectrochemical and photocatalytic activity, Electrochim. Acta. 91 (2013) 30-35.

[22]   R. Yimnirun, J. Tangsritrakul, S. Rujirawat, S. Limpijumnong, Identification of Mn Site in $BaTiO_3$ by Synchrotron X-Ray Absorption Spectroscopy Measurements, Ferroelectrics. 381 (2009) 130–143.

[23]   H. Yamaguchi, H. Uwe, T. Sakudo, E. Sawaguchi, Raman-Scattering Study of the soft Phonon Modes in Hexagonal Barium titanate, J. Phys. Soc. Jpn. 56 (1987) 589-595.

[24]   J. L. Parsons, L. Rimai, Raman Spectrum of $BaTiO_3$, Solid. State. Commun. 5 (1967) 423-427.

[25]   D. P. Dutta, M. Roy, N. Maiti, A. K. Tyagi, Phase evolution in sonochemically synthesized Fe^{3+} doped $BaTiO_3$ nanocrystallites: structural, magnetic and ferroelectric characterization, Phys. Chem. Chem. Phys. 18 (2016) 9758-9769.

[26]   D. W. Barnum, Electronic absorption spectra of acetyl-acetonato complexes-I, complexes with trivalent transition metal ions, J. Inorg. Nucl. Chem. 21 (1961) 221 - 237.

[27]   T. S. Davis, J. P. Fackler, M. J. Weeks, Spectra of manganese (III) complexes. Origin of the low-energy band, Inorg. Chem. 7 (1968) 1994-2002.

[28]   R. S. Drago, Electronic absorption spectroscopy, Physical Methods in Inorganic Chemistry, East-West Press Pvt. Ltd. New Delhi (1965), 135–181.

[29]   B. Sarkar, K. Chakrabarti, K. Das, S. K. De, Optical and ferroelectric properties of ruthenium-doped $BaTiO_3$ nanocubes, J. Phys. D: Appl.Phys. 45 (2012) 505304 (1-10)

[30]   D. D. Cuong, J. Lee, Electronic structure of oxygen deficient $BaTiO_3$, Integr. Ferroelectr. 84 (2006) 23-30.

[31]   R. Inoue, S. Ishikawa, Y. Kitanaka, T. Oguchi, Y. Noguchi, M. Miyayama, Photocurrent Characteristics of Mn-Doped Barium Titanate Ferroelectric Single Crystals, Jpn. J. Appl. Phys. 52 (2013): 09KF03 (1-6).

[32]   M. Borah, D. Mohanta, Composite-Hydroxide-Mediated Formation of Barium Titanate Nanocubes and Their Optical Emission Response, Chin. J. Phys. 53 (2015) 020804 (1-10).

[33]   S. B. Rudraswamy, N. Bhat, Optimization of RF Sputtered Ag-Doped $BaTiO_3$-CuO Mixed Oxide Thin Film as Carbon Dioxide Sensor for Environmental Pollution Monitoring Application, IEEE Sens. J. 16 (2016) 5145-5151.

[34]   M. Murata, K. Wakino, S. Ikeda, X-ray photoelectron spectroscopic study of perovskite titanates and related Compounds: An example of the effect of polarization on chemical shifts, J. Electron. Spectrosc. Rel. Phenomena 6 (1975) 459-464.

[35]   M. J. Jackman, A. G. Thomas, C. Muryn, Photoelectron Spectroscopy Study of Stoichiometric and Reduced Anatase TiO_2 (101) Surfaces: The Effect of Subsurface Defects on Water Adsorption at Near-Ambient Pressures, J. Phys. Chem. C 119 (2015) 13682-13690.

[36]   C. M. Desbuquoit, J. Riga , J. J. Verbist, Electronic structure of titanium(III) and titanium(IV) halides studied by solid-phase x-ray photoelectron spectroscopy, Inorg. Chem. 26 (1987) 1212-1217.

[37] R. Ren, Z. Wen, S. Cui, Y. Hou, X. Guo, J. Chen, Controllable Synthesis and Tunable Photocatalytic Properties of Ti^{3+}-doped TiO_2, Sci. Rep. 5 (2015) 10714(1-11).

[38] V. Etacheri, M. K. Seery, S. J. Hinder, S. C. Pillai, Oxygen Rich Titania: A Dopant Free, High Temperature Stable, and Visible-Light Active Anatase Photocatalyst, Adv. Funct. Mater. 21 (2011) 3744-3752.

[39] S. Nayak, B. Sahoo, T. K. Chaki, D. Khastgir, Facile preparation of uniform barium titanate ($BaTiO_3$) multipods with high permittivity: impedance and temperature dependent dielectric behavior, RSC Adv. 4 (2014) 1212-1224.

[40] Z. Huang, W. Zhou, C. Ouyang, J. Wu, F. Zhang, J. Huang, Y. Gao, J. Chu, High performance of Mn-Co-Ni-O spinel nanofilms sputtered from acetate precursors, Sci. Rep. 5 (2015) 10899(1-8).

[41] M. C. Biesinger, B. P. Payne, A. P. Grosvenor, L. W. M. Lau, A. R. Gerson, R. S. C. Smart, Resolving surface chemical states in XPS analysis of first row transition metals, oxides and hydroxides: Cr, Mn, Fe, Co and Ni, Appl. Surf. Sci. 257 (2011) 2717–2730.

[42] B. Douglas, D. Mcdaniel, J. Alexander, Concepts and Models of Inorganic Chemistry. Wiley India (P) Ltd. (2006) Page No 356-358.

[43] L. Zhang, Y. Zhang, Z. Ye, J. Lu, B. Lu, B. He, The effects of group-I elements co-doping with Mn in ZnO dilute magnetic semiconductor, J. Appl. Phys. 111 (2012) 123524(1-4).

[44] T. Chakraborty, S. Ray, M. Itoh, Defect-induced magnetism: Test of dilute magnetism in Fe-doped hexagonal $BaTiO_3$ single crystals, Phys. Rev. B: Condens. Matter. Mater. Phys. 83 (2011) 144407(1-5).

[45] J. M. D. Coey, M. Venkatesan, C. B. Fitzgerald, Donor impurity band exchange in dilute ferromagnetic oxides, Nat. Mater. 4 (2005) 173-179.

LIST OF PUBLICATIONS/PATENTS

The important findings of the present work have appeared in the following publications.

1) Titania nanotube arrays surface-modified with ZnO for enhanced photocatalytic applications, **Manoj Nageri**, Vijila Kalarivalappil, Baiju K Vijayan, V Kumar, Mater. Res. Bull. 77 (2016) 35-40.

2) SnO_2-loaded $BaTiO_3$ nanotube arrays: fabrication and visible light photocatalytic application, **Manoj Nageri**, A B Shalet, V Kumar, J. Mater.Sci: Mater. Electron. 28 (2017) 9770-9776.

3) Manganese-doped $BaTiO_3$ nanotube arrays for enhanced visible light photocatalytic applications, **Manoj Nageri**, Viswanathan Kumar, Mater. Chem. Phys. 213 (2018) 400-405**.**

4) Stability studies of PbS sensitised TiO_2 nanotube arrays for visible light photocatalytic applications by X-ray photoelectron spectroscopy (XPS), N B Rahna, Vijila Kalarivalappil , **Manoj Nageri** , Suresh C Pillai, Steven J Hinder , V Kumar, Baiju K Vijayan, Mater. Sci.Semicond. Process. 42 (2016) 303-310.

5) Pd Loaded TiO_2 Nanotubes for the Effective Catalytic Reduction of p-Nitro phenol, Vijila Kalarivalappil, C M Divya,W Wunderlich, Suresh C Pillai, Steven J Hinder, **Manoj Nageri**, V Kumar, Baiju K Vijayan, Catal. Lett. 146 (2016) 474-482.

Patent filed.

1. Nano-Zinc oxide process of preparation and application thereof, **Nageri Manoj**, Kizhakekilikoodayil Vijayan Baiju, Viswanathan Kumar, file no-2348/DEL/2015, filing date-July 30, 2015.

Details of Seminar attendated.

1) Participated and presented a poster-in Indo-US, international work shop on Nano structured Electronic Materials: Challenges & Relevance to electronics & energy research-2013, March (IUSWNM-2013) conducted by C-MET Thrissur, Children's hospital Harvard USA, Northeastern University USA, Joint School of nano science & nano engineering USA.

2) Attended in UGC sponsored National Seminar on Advanced Materials (NSAM)-February 2014, organized by- Department of Physics, Vimala College, Thrissur.

3) Participated in the UGC sponsored graduate seminar on Advances in materials chemistry-December-2014 (AMC-2014) organized by the department of chemistry, university of Calicut.

4) Participated and done oral presentation in National Seminar (Frontiers in chemical sciences FCS)- 2018, February conducted by Department of Chemistry, University of Calicut.